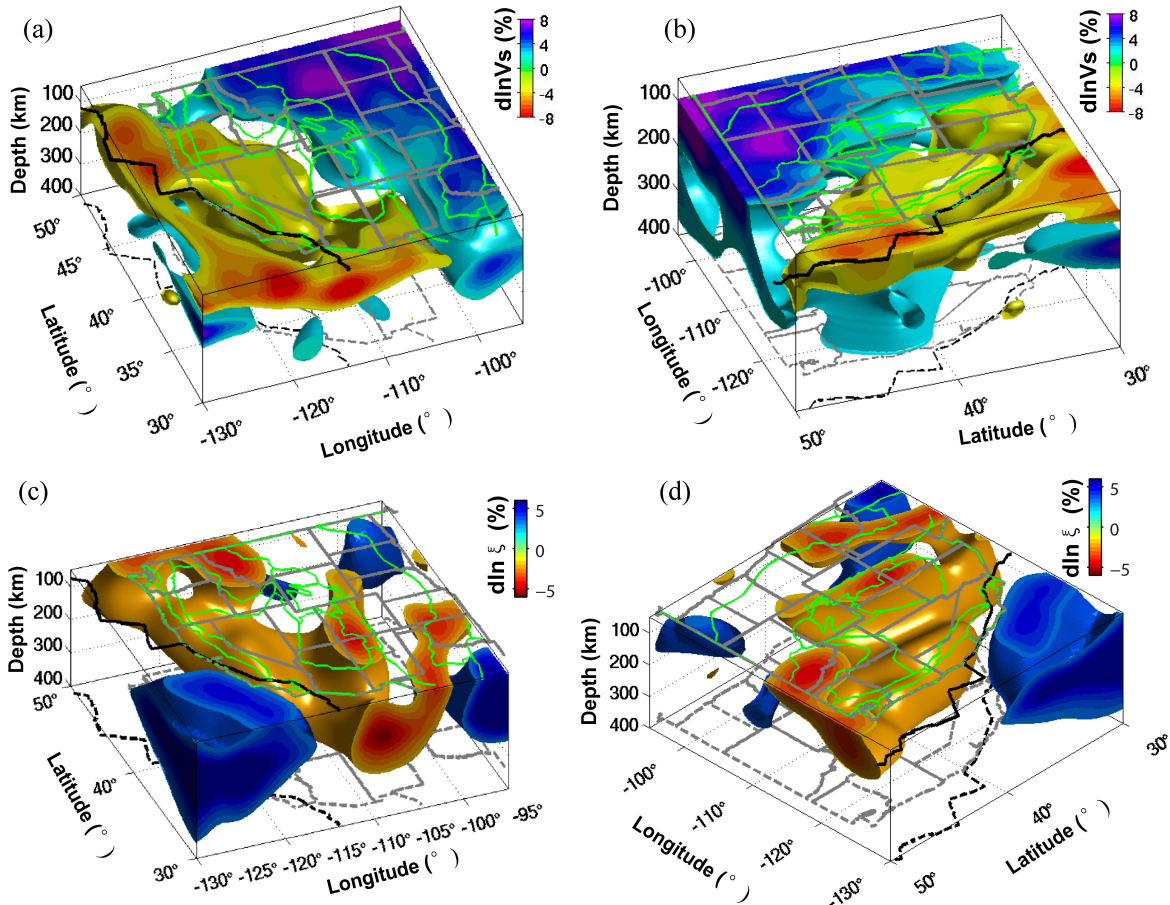


Berkeley Seismological Laboratory



Annual Report
July 2009 - June 2010

Berkeley Seismological Laboratory
Annual Report
July 2009 - June 2010

Cover Picture

3-D rendering of the North American isotropic and radially anisotropic shear wave model *SVEMum_NA2* (Research Section 11) in the western US, viewing from the southwest (a and c), and the northwest (b and d). The velocity variations are with respect to the NA regional average. The isosurfaces in a) and b) are drawn at -1.5% and 3% for the slow and fast velocities, respectively. For radial anisotropy (c and d), the isosurface values are -2% and 4%. Green lines at the top of each plot indicate the western US physiographic regions. Thick black line is the plate boundary between the North American and the Pacific plates.

Contents

| | | |
|----------|---|----------|
| 1 | Director’s Report | 1 |
| 1 | Introduction | 1 |
| 2 | History and Facilities | 1 |
| 3 | BSL staff news | 3 |
| 4 | Acknowledgements | 3 |
| 2 | Research Studies | 5 |
| 1 | Global Effective Elastic Thickness, Mechanical Anisotropy and the Supercontinent Cycle | 6 |
| 2 | New Terrestrial LIDAR and Cosmogenic Radionuclide Constraints on the Little Lake Fault, Eastern California Shear Zone | 8 |
| 3 | Using Geodetic Data to Understand Postseismic Processes following the Sumatra-Andaman Earthquake | 10 |
| 4 | Interseismic Creep on the Concord Fault from PS-InSAR and SBAS | 12 |
| 5 | Probing the Deep Rheology of Tibet Constraints from 2008 M_w 7.9 Wenchuan, China Earthquake . . | 14 |
| 6 | Tidal Triggering of LFEs near Parkfield, CA | 16 |
| 7 | Monitoring Slow Moving Landslides in the Berkeley Hills with TerraSAR-X Data | 18 |
| 8 | Slab-Plume Interaction Beneath the Pacific Northwest | 20 |
| 9 | Imaging Shallow Cascadia Structure with Ambient Noise Tomography | 22 |
| 10 | Anisotropic Layering of the North American Craton | 24 |
| 11 | 3-D Shear Wave Radially and Azimuthally Anisotropic Velocity Model of the North American Upper Mantle | 26 |
| 12 | Depth Dependent Azimuthal Anisotropy in the Western US Upper Mantle | 28 |
| 13 | Seismic Signature of Perovskite and Postperovskite in the D” | 30 |
| 14 | Using the SEM to Simulate Random Wavefields and Improve Noise Tomography | 32 |
| 15 | Toward the Future of Global Waveform Tomography: Scalable Gauss-Newton and Alternative Data-Partitioning Schemes | 34 |
| 16 | Towards Constraining Lateral Variation of Attenuation Structure With Low-Degree Normal Modes Splitting Coefficients | 36 |
| 17 | Efficient Computation of NACT Seismograms: Toward Application in Imagining Upper Mantle Discontinuities | 38 |
| 18 | Modeling of the Byerly’s False S Phase | 40 |
| 19 | ShakeAlert: A Unified EEW System for California | 42 |
| 20 | January 10, 2010 M_w 6.5 Gorda Plate Earthquake: Automated Finite-Source Modeling | 44 |
| 21 | Towards a Real-time Earthquake Source Determination and Tsunami Early Warning in Northern California | 46 |
| 22 | Seismic Constraints on Fault-Zone Frictional Properties at Seismogenic Depth on the San Andreas Fault, Parkfield | 48 |
| 23 | Postseismic Variations in Seismic Moment and Recurrence Interval of Repeating Earthquakes at Parkfield | 50 |
| 24 | Identification of Nonvolcanic Tremors Triggered by Regional Earthquakes in the Parkfield, California Region | 52 |
| 25 | Locating Nonvolcanic Tremors Beneath the San Andreas Fault Using a Station-pair Double-Difference Location Method | 54 |

| | |
|---|------------|
| 3 BSL Operations | 57 |
| 1 Berkeley Digital Seismic Network | 59 |
| 2 California Integrated Seismic Network | 67 |
| 3 Northern Hayward Fault Network | 72 |
| 4 Parkfield Borehole Network (HRSN) | 81 |
| 5 Bay Area Regional Deformation Network | 91 |
| 6 Northern California Earthquake Data Center | 97 |
| 7 Data Acquisition and Quality Control | 107 |
| 8 Northern California Earthquake Monitoring | 112 |
| 9 Outreach and Educational Activities | 118 |
| Glossary | 120 |
| Appendix I Publications, Presentations, Awards, and Panels 2009-2010 | 122 |
| Appendix II Seminar Speakers 2009-2010 | 135 |
| Appendix III Organization Chart 2009-2010 | 137 |

Chapter 1

Director's Report

1 Introduction

As in previous years, I am pleased to introduce the 2009-10 Berkeley Seismological Laboratory Annual Report. This report covers two interrelated activities at BSL: basic research and real time earthquake monitoring operations. Chapter 2 describes the research accomplishments; Chapter 3 details progress in our development of infrastructure and facilities.

The basic research spans many topics in seismology and tectonics. They range from studies of the earth's deep structure and dynamics to various aspects of earthquake physics; from microearthquakes and tremor studies to studies of earthquake mechanisms and rupture spanning different times scales; and from slow tectonic deformation to real time seismology and earthquake early warning. These are described in 25 "two-page" contributions in Chapter 2 of this report. Highlights this year include a collection of studies at different scales of the upper mantle seismic isotropic and anisotropic structure beneath North America, taking advantage of the new broadband seismic dataset provided by the USArray component of the NSF funded national Earthscope program (Chapter 2, Research Sections 8, 9, 10, 12, and 11).

This year has been quite busy on the operational side of the BSL, owing to significant funding received through the USGS, in the framework of ARRA, to upgrade the recording systems at many of our broadband and borehole stations. We have already upgraded two-thirds of our broadband stations with state of the art Quanterra Q330 dataloggers, and we are starting to upgrade those at our borehole stations. These upgrades were much needed, as many of the recording systems were 15-20 years old, well beyond the expected lifetime of computer hardware. We have also received funding to upgrade receivers at our 26 BARD stations and to add GPS receivers at 7 of our existing BDSN stations. The new receivers will allow us to stream high rate (1Hz sampling) GPS data and to start implementing the use of GPS data in our real-time earthquake analysis procedures. Much effort has also gone into redesigning the data processing proce-

dures and the web presentation for the continuous GPS data from the BARD network.

We have continued our involvement in the redesign of the STS-1 very broad band seismometer, under Metrozot's leadership, and with funding from the NSF EAR-Instruments and Facilities Program. The development phase is practically finished, and the new instruments are now being tested and fine-tuned not only at our Byerly Vault but also at Harvard (HRV) and the Albuquerque Seismological Laboratory.

The following sections give a brief historical overview of the BSL, and finally some BSL staff news.

2 History and Facilities

The Berkeley Seismological Laboratory (BSL), formerly the Berkeley Seismographic Stations (BSS), is the oldest Organized Research Unit (ORU) on the UC Berkeley campus. Its mission is unique in that, in addition to research and education in seismology and earthquake-related science, it is responsible for providing timely information on earthquakes (particularly those that occur in Northern and Central California) to the UC Berkeley constituency, to the general public, and to various local and state government and private organizations. The BSL is therefore both a research center and a facility/data resource, which sets it apart from most other ORUs. A major component of our activities is focused on developing and maintaining several regional observational networks, and participating, along with other agencies, in various aspects of the collection, analysis, archival, and distribution of data pertaining to earthquakes, while maintaining a vigorous research program on earthquake processes and Earth structure. In addition, the BSL staff spends considerable time on public relations activities, including tours, talks to public groups, responding to public inquiries about earthquakes, and, more recently, World-Wide-Web presence (<http://seismo.berkeley.edu/>).

UC Berkeley installed the first seismograph in the Western Hemisphere at Mount Hamilton (MHC) in 1887. Since then, it has played a leading role in the operation

of state-of-the-art seismic instruments and in the development of advanced methods for seismic data analysis and interpretation. Notably, the installation, starting in 1927, of Wood-Anderson seismographs at 4 locations in Northern California (BKS, ARC, MIN, and MHC) allowed the accurate determination of local earthquake magnitude (M_L) from which a unique historical catalog of regional earthquakes has been maintained to this day, providing crucial input to earthquake probabilities studies.

Over the years, the BSS continued to keep pace of technological improvements. The first centrally telemetered network using phone lines in an active seismic region was installed by BSS in 1960. The BSS was the first institution in California to operate a 3-component “broadband” system (1963). It played a major role in the early characterization of earthquake sources using “moment tensors” and source-time functions. The BSS also made important contributions to the early definitions of detection/discrimination of underground nuclear tests and, jointly with UCB Engineering, to earthquake hazards work. Starting in 1986, the BSS acquired 4 state-of-the-art broadband instruments (STS-1), while simultaneously developing PC-based digital telemetry, albeit with limited resources. As telecommunication and computer technologies made rapid progress, in parallel with broadband instrument development, paper record reading was completely abandoned in favor of largely automated analysis of digital data.

The current facilities of BSL have been built progressively over the last two decades, efforts initiated by significant “upgrade” funding from UC Berkeley in 1991-1995. The BSL currently operates and acquires data, continuously and in real-time, from over 60 regional observatories. These house a combination of broadband and strong motion seismic instrumentation installed in vaults, borehole seismic instrumentation, the permanent GPS stations of the Bay Area Regional Deformation (BARD) network, and electromagnetic sensors. The seismic data are fed into the BSL real-time processing and analysis system. Since 1996, they are used in conjunction with data from the USGS NCSN network in the joint earthquake notification program for Northern California. This program capitalizes on the complementary capabilities of the networks operated by each institution to provide rapid and reliable information on the location, size and other relevant source parameters of regional earthquakes. In recent years, a major emphasis in BSL instrumentation has been in densifying the state-of-the-art seismic and geodetic networks. At the same time, research efforts have been directed toward the development of robust methods for quasi-real time, automatic determination of earthquake source parameters and predicted strong ground motion, using a sparse network combining broadband and strong motion seismic sensors, as well as permanent geodetic

GPS receivers. Recently, research emphasis has been directed toward the development of “earthquake early warning” capabilities

The Berkeley Digital Seismic Network (BDSN), a regional network of 32 digital broadband and strong motion seismic stations with continuous telemetry to UC Berkeley, is the backbone of the BSL operations. This network contributes basic regional data for real-time estimation of location, size and rupture parameters for earthquakes in Central and Northern California. It is the Berkeley contribution to the California Integrated Seismic Network (CISN). In June 2009, our operational software, the Rapid Earthquake Data Integration (REDI) program, was replaced by the CISN, now AQMS, software (see Chapter 3, Operational Section 8). The data from the BDSN also provide a fundamental database for the investigation of three-dimensional crustal structure and its effects on regional seismic wave propagation. This is ultimately crucial for estimating ground shaking for future earthquakes. Most stations also record auxiliary temperature/pressure channels, valuable in particular for background noise quality control. Complementing this network is a ~ 25 station “high-resolution” network of borehole seismic sensors located along the Hayward Fault (HFN) and under the Bay Area bridges, operated jointly with the USGS/Menlo Park and linked to the Bridge Safety Project of the California Department of Transportation (Caltrans). The latter has facilitated the installation of sensor packages at 15 bedrock boreholes along 5 East Bay bridges in collaboration with Lawrence Livermore National Laboratory (LLNL). A major science goal of this network is to collect high signal-to-noise data for micro-earthquakes along the Hayward Fault to gain insight into the physics that govern fault rupture and its nucleation. The BSL also operates and maintains the 13 element Parkfield borehole seismic array (HRSN). This array provides high quality data on micro-earthquakes, clusters and most recently tremors, and is an important reference for the San Andreas Fault Observatory at Depth (SAFOD). Since April 2002, the BSL collaborates with MBARI on the operation of a permanent broadband ocean bottom station, MOBB.

In addition to the seismic networks, the BSL operates, maintains and processes data from the 26 permanent geodetic stations of the BARD Network. It archives and distributes this data as well. Where possible, BARD sites are collocated with BDSN sites to minimize telemetry costs. In particular, sites are progressively being upgraded to 1 Hz sampling. This will support one focus of BSL research, the development of analysis methods which combine seismic and geodetic data to rapidly estimate source parameters of significant earthquakes.

Finally, two of the BDSN stations (PKD, SAO) also share data acquisition and telemetry with 5-component electromagnetic sensors installed with the goal of investi-

gating the possibility of detection of tectonic signals. In 2002-2003, automated quality control software was implemented to monitor the electromagnetic data.

Archival and distribution of data from these and other regional networks is performed at the Northern California Earthquake Data Center (NCEDC), operated at the BSL in collaboration with USGS/Menlo Park. The data reside on a mass-storage device (current holdings ~ 50 terabytes), and are accessible “on-line” over the Internet (<http://www.ncedc.org>). Among others, data from the USGS Northern California Seismic Network (NCSN), are archived and distributed through the NCEDC. The NCEDC also maintains, archives and distributes the ANSS earthquake catalog.

Core University funding to our ORU has until now provided salary support for one staff scientist and several technical and administrative staff members, representing about 30% of the total infrastructure support. The remaining support comes from extra-mural grants and contracts, primarily from the USGS, NSF, and the State of California, through its Emergency Management Agency (CalEMA, formerly OES). We acknowledge valuable recent contributions from other sources such as Caltrans and PEER, as well as our Earthquake Research Affiliates. The effects of drastic budget cuts in FY09-10 are temporarily being offset by ARRA funding from the USGS.

3 BSL staff news

Changes in BSL staff in 2009-10 are as follows.

In the past year, the following graduate students associated with BSL completed their PhD's: Ved Lekic graduated in December 2009 and joined Brown University in May on an NSF post-doctoral fellowship. Trey Apel completed his doctorate in April 2010, and Gilead Wurman in May 2010. They are now working in industry at AMEC Geomatrix and Seismic Warning Systems, respectively.

There has been one new arrival: Andrea Chiang joined the BSL as a graduate student in the Fall of 2010.

BSL hosted the following visiting scientists in 09-10: Dr. Joshi Karra from the National Geophysical Research Institute, Hyderabad, India, and Yann Capdeville, from IPGP in France.

As a result of a campus-wide reorganization of the research administration of Organized Research Units, our four administrative staff were laid off, effective November 30, 2009. Tina and Yolanda were rehired at RES (Research Enterprise Services), the agency which provided business administration for BSL from December 2009 thru June 2010. After a brief sojourn at RES, Kristen Jensen, our former manager, joined EFA. They are very fortunate to have her! All three have been outstanding members of the BSL team, and we are sorry to see them go despite all our efforts. Fortunately, we

were able to rehire Kate Lewis in March 2010 as Executive Assistant, to coordinate the programmatic aspects of BSL administration during the RES tenure. Kate has also played a major role in helping organize the 6 week long CIDER-2010 summer program in Santa Barbara, CA (<http://www.deep-earth.org/summer10.html>) and the international SEDI 2010 symposium that followed from July 18-23, 2010. Since July 2010, BSL administration has been consolidated with that of the Earth and Planetary Science department, and Kate is now in charge of the coordination of all funds and transactions related to the BSL operations, as well as handling many everyday tasks while we wait for the hire of two additional administrative staff, jointly with EPS.

Finally, Rick McKenzie retired in June 2010. We miss him!

The greater BSL family has continued to grow in the past year, with the arrival of Audrey Lewis in October 2009. She was followed by Freeman McCarty and Arieh Wurman-Fenton in November 2009, Henry Allen in April 2010, and Rebekah Zheng in June 2010.

4 Acknowledgements

I wish to thank our technical and administrative staff, scientists and students for their efforts throughout the year and their contributions to this Annual Report. Individual contributions to activities and report preparation are mentioned in the corresponding sections, except for the Appendix section, which was prepared by Jennifer Taggart.

I also wish to specially thank the individuals who have regularly contributed to the smooth operation of the BSL facilities: Mario Aranha, Rich Clymer, Doug Dreger, John Friday, Jarrett Gardner, Peggy Hellweg, Ingrid Johanson, Bill Karavas, Oleg Khainovski, Rick Lellinger, Pete Lombard, Rick McKenzie, Bob Nadeau, Doug Neuhauser, Charley Paffenbarger, Jennifer Taggart, Taka'aki Taira, Bob Uhrhammer, and Stephane Zuzlewski, and in the administrative office, Kristen Jensen, Kate Lewis, Tina Barber-Riggins, and Yolanda Andrade. I also wish to thank our undergraduate assistants, Chris Rawles, Danny Feucht, Josef Matlak, Eric Winchell, and Amanda Truyol, for their contributions to our research and operations activities.

I am particularly grateful to Jennifer Taggart and Peggy Hellweg for their help in putting together this Annual Report and bringing it to completion.

The Annual Report of the Berkeley Seismological Laboratory is available on the Web at http://seismo.berkeley.edu/annual_report.

Chapter 2

Research Studies

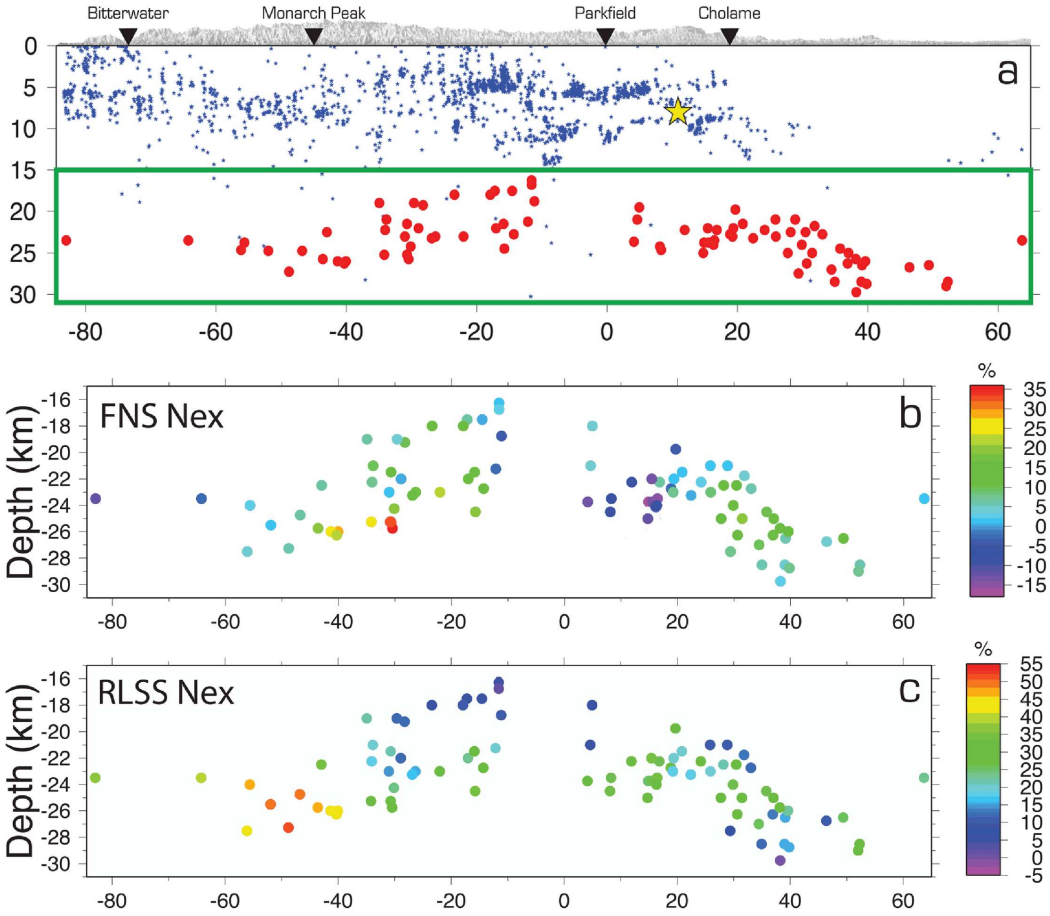


Figure 2.1: (a) Along-fault cross section of the SAF viewed from the south-west. Vertically exaggerated topography is shown in grey. Local towns are marked by inverted triangles. Hypocenters of SAF seismicity, the 2004 Parkfield earthquake, and LFE locations are shown as blue dots, yellow star, and red circles respectively. Panels (b) and (c) are delineated by the green box. (b) LFE locations color coded by their FNS Nex (percent excess = [actual number of LFEs during times of positive FNS - expected number of LFEs during times of positive FNS]/expected number of LFEs during times of positive FNS). (c) LFE locations color coded by the RLSS Nex values. (Figure from Research Section 6)

1 Global Effective Elastic Thickness, Mechanical Anisotropy and the Supercontinent Cycle

Pascal Audet and Roland Bürgmann

1.1 Introduction

The Earth experienced several supercontinent cycles since 2.7 Ga, the last one ending with the breakup of Pangaea into the current plate configuration. The driving mechanism is associated with vertical motion of the convective mantle from both subduction of ocean basins during supercontinent assembly and warm mantle upwelling causing breakup and the creation of new ocean floor (Gurnis, 1988). Although the details of the dynamics are still debated, it is generally agreed that continental margins are repeatedly deformed within weak, diffuse zones, and that stronger cratonic lithosphere remains intact during this process. Most cratonic cores within continents show crustal ages greater than 2.0 Gyr, are depleted in basaltic constituents, and have conductively cooled through time, thus acquiring a thick, high-viscosity thermo-chemical root (Jordan, 1978). Continental margins, in contrast, are much younger (< 0.5 Gyr), have been thermally rejuvenated and structurally reactivated, and are much thinner. Such large differences in structure imply comparably large gradients in rheological properties of the lithosphere. These factors, combined with numerical simulations of coupled mantle convection and continental plates, suggest that deformation during supercontinent cycles is controlled by pre-existing structure acquired from past tectonic events. There is little observational constraint, however, on the spatial variability of rheological properties of the lithosphere because it cannot be observed directly.

1.2 Method

A useful proxy for the the long-term strength of the lithosphere is given by the flexural rigidity, $D = ET_e/12(1 - \nu^2)$, where E is Young’s modulus and ν is Poisson’s ratio, which governs the resistance to flexure (Watts, 2001). The strong dependence of D on T_e implies that the magnitude and spatial variations of T_e can have a significant influence on the degree and style of deformation due to long-term tectonic loads. In particular, it is expected that spatial variations and gradients in T_e can prescribe where strain may localize and consequently determine the locus of deformation as manifested by brittle (e.g. seismicity, faulting) and thermal processes (e.g. volcanism, rifting). T_e is estimated by comparing the spectral coherence between topography and Bouguer gravity anomalies with that predicted for an equivalent elastic plate bending under surface and internal loading. The plate response is modeled either as isotropic

or anisotropic, and the coherence is inverted for a single parameter, T_e , or the three parameters of an orthotropic elastic plate (i.e. having different rigidities in two perpendicular directions), T_{min} , T_{max} , and ϕ_e , the direction of weakest rigidity. Here we use the wavelet transform method to calculate the coherence and estimate T_e and T_e anisotropy (Audet and Mareschal, 2007) and apply the technique to all major continents, with the exception of Greenland and Antarctica where thick ice caps complicate the analysis and data coverage is incomplete. We account for possible bias in T_e estimation by considering the effect of gravitational “noise” and masking regions where the model fails.

1.3 Results

Figure 2.2 shows the azimuthal variations of the weak direction of T_e superposed on the pattern of T_e variations. In general, the T_e pattern correlates with age since the last thermo-tectonic event. T_e is high (> 100 km) in Early to Late Proterozoic and Archean cratonic provinces, with the largest values found in the North American, West African, and East European shields. Some cratons (e.g. South Africa, North China, South India) exhibit lower T_e ($50 < T_e < 100$ km) where lithosphere has been thinned by plume-related magmatism or delamination. Low T_e (< 40 km) is found in young Phanerozoic orogens (e.g. American Cordillera, Alpine belt) and tectonically active provinces (e.g. western North America, Afar Triple Junction and most of central-eastern Asia). T_e is also generally low in the hanging wall of past and present subduction zones and along most continental margins, possibly due to thermal and fluid-related weakening as a consequence of subduction and rifting processes. T_e anisotropy varies over short spatial scales ($\sim 200 - 500$ km) in both magnitude and direction (Figure 2.2), thus ruling out a deep, sub-lithospheric mantle-flow origin. Magnitude of T_e anisotropy is inversely correlated with T_e as young, low- T_e provinces display larger magnitude than older, high- T_e cratons. Directions of weak rigidity are oriented normal to most continental margins and tectonic boundaries. T_e anisotropy reflects directional variations in the flexural compensation of the lithosphere and has been speculated to originate from either dynamical or structural effects.

These results allow us to clarify the role of rheological heterogeneity and mechanical anisotropy in continental evolution and deformation. That T_e varies according to age since the last thermo-tectonic event and is parti-

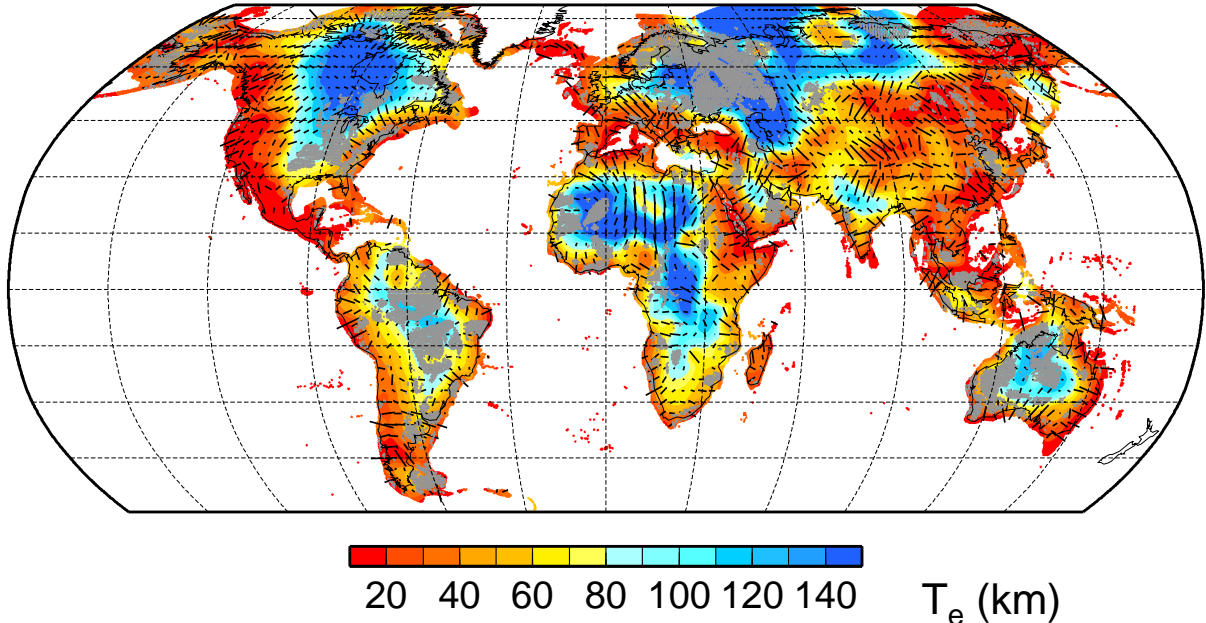


Figure 2.2: Global effective elastic thickness over continents calculated from the coherence between Bouguer gravity and topography using a wavelet transform. T_e anisotropy (sampled on a $3^\circ \times 3^\circ$ grid) is superposed on filtered (using a Gaussian function of width 900 km) and color-contoured T_e over continents and continental shelves (depth shallower than 500 m below sea level). Shaded areas correspond to regions where T_e estimation is biased by gravitational “noise.” The length of black bars is given by the magnitude of T_e anisotropy from the ratio $(T_{max} - T_{min}) / (T_{max} + T_{min})$.

tioned between continental cores and margins is consistent with the episodic thermal rejuvenation of continental margins and resetting of lithosphere strength during thermo-tectonic events. These episodes originate from large-scale vertical convective motion of the mantle during continental assembly and breakup and are accompanied by margin-wide faulting and fault reactivation (either from rifting or thrusting) that further weakens marginal lithosphere and induces significant mechanical anisotropy. A weak and faulted lithosphere may enhance deformation by concentrating strain at pre-existing structures. Over time, these factors isolate continental interiors from deformation due to plate boundary forces during continental assembly, thus creating positive feedback and allowing only a small fraction of continental lithosphere to be recycled. Only in rare cases do plumes or delamination events de-stabilize cratonic cores. This model is consistent with numerical models of continental evolution that simulate the stability of cratonic crust and longevity of deeper roots as a consequence of higher yield strength with respect to oceanic lithosphere, and the buffering effect of weak mobile belts and margins that absorb stresses during repeated supercontinent cycles. This, in turn, implies that the inherited weakness of marginal lithosphere is relatively long-lived, despite its tendency to get recycled into the mantle during orogeny, possibly due to con-

tinuous accretion of terranes and plateaus that further enhances mechanical weakness and anisotropy.

1.4 Acknowledgements

This work was funded by the Miller Institute for Basic Research in Science (UC Berkeley).

1.5 References

- Audet, P., and J.-C. Mareschal, Wavelet analysis of the coherence between gravity and topography: Application to the elastic thickness anisotropy in the Canadian Shield, *Geophys. J. Int.*, 168, 287-298, 2007.
- Gurnis, M. Large-scale mantle convection and the aggregation and dispersal of supercontinents, *Nature*, 332, 695-699, 1988.
- Jordan, T. H., Composition and development of the continental tectosphere, *Nature*, 274, 544-548, 1978.
- Watts, A. B., *Isostasy and Flexure of the lithosphere*, Cambridge University Press, Cambridge, UK, 2001.

2 New Terrestrial LIDAR and Cosmogenic Radionuclide Constraints on the Little Lake Fault, Eastern California Shear Zone

Colin Amos, Roland Bürgmann, G. Burch Fisher (UCSB), Dylan Rood (LLNL), Angela Jayko (USGS)

2.1 Introduction

An ever-expanding inventory of fault slip-rates spanning various time intervals reveals contrasting spatial and temporal patterns of strain for active faults within the eastern California shear zone (ECSZ). Comparison of these data, derived from geologic, geomorphic, and paleoseismic records, with geodetic estimates of fault loading affords unparalleled opportunity to investigate the dynamics of earthquake processes and the evolution of an intracontinental plate boundary fault system. This work focuses on the Little Lake fault, which occurs along the western margin of the ECSZ between the Sierra Nevada and the Coso Range in east-central California. The fault accommodates 10-20% of the total dextral motion within the ECSZ at this latitude and a smaller fraction of the relative motion between the Pacific and North American plates. Relatively high rates of decadal fault loading described for the Little Lake fault zone from GPS measurements and InSAR data (7 ± 3 mm/yr; *Peltzer et al.*, 2001) suggest potential discrepancies with longer, late Quaternary records of geologic strain. To address this inconsistency, we targeted a series of previously unrecognized fluvial terraces related to overtopping and outflow from pluvial Owens Lake that cross the fault and record dextral offset since Late-Pleistocene time.

2.2 Methods

Geologic constraints on displaced Quaternary geomorphic features along the Little Lake fault zone come from geologic and geomorphic mapping and high-resolution digital topography collected using a Riegl LMS-Z420i terrestrial laser scanner (TLS).

Constraints on the age of offset terrace surfaces and risers come from cosmogenic ^{10}Be samples (currently being processed) from intact, meter-scale outwash boulders preserved on terrace treads bounding each riser. Slip rates were computed using the methods and code outlined by *Zechar and Frankel* (2009) from probability distributions of displacement and correlated surface age.

2.3 Findings

Initial results from TLS measurements of Late-Pleistocene geomorphic surfaces on the Little Lake fault zone suggest between 33 and 38 m of reconstructed right-lateral displacement over this time period. Preliminary correlation of terrace surfaces with exposure dating of fluvially scoured basalt upstream at Fossil Falls (~ 16 ka;

Cerling, 1990) suggests a right-lateral displacement-rate on the order of ~ 2 mm/yr at 95% confidence.

Although more than double the previously reported rate estimate (≥ 1 mm/yr; *Roquemore*, 1988) based on older, poorly constrained basalt flows, this result tentatively suggests that decadal rates of loading ($\leq \sim 5$ mm/yr) on the Little Lake fault zone are not sustained geologically over the $\sim 10,000$ year timescale. Future work will explore the implications of this rate variation for the ECSZ and fault networks in general.

2.4 Acknowledgements

This work is supported by NSF award EAR 0847990 to Amos.

2.5 References

- Cerling, T.E., Dating geomorphologic surfaces using cosmogenic He-3: *Quaternary Research*, 33(2), 148-156, 1990.
- Peltzer, G., Crampe, F., Hensley, S., and Rosen, P., Transient strain accumulation and fault interaction in the Eastern California shear zone: *Geology* 29(11), 975-978, 2001.
- Roquemore, G.R., Revised estimates of the slip rate on the Little Lake fault, California: *Geological Society of America Abstracts with Programs*, 20(3), 225, 1988.
- Zechar, J.D., and Frankel, K.L., 2009, Incorporating and reporting uncertainties in fault slip rates: *Journal of Geophysical Research-Solid Earth*, 114, DOI 10.1029/2009JB006325.

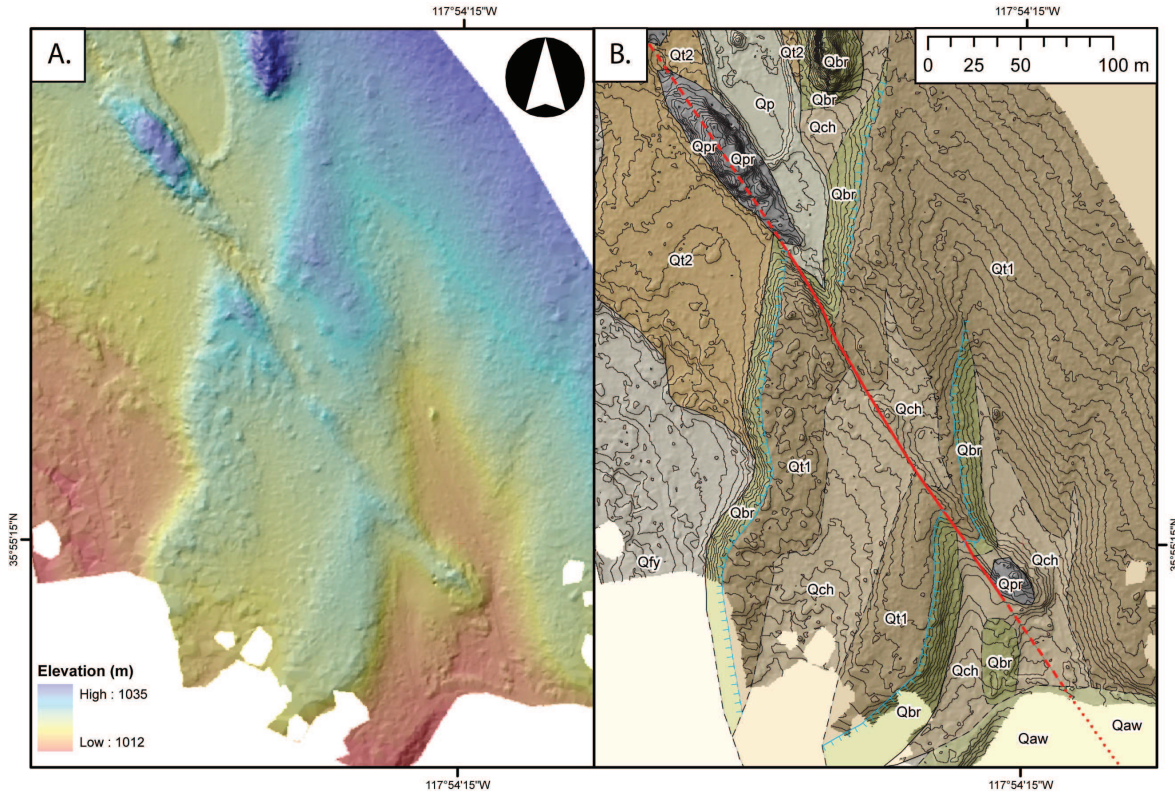


Figure 2.3: A) 50-cm DEM of lower Little Lake wash overlain on a hillshade image, both computed from high-resolution terrestrial laser scanning (TLS) surveys. B) Geologic mapping and 50-cm elevation contours of the same area as (A), highlighting right-lateral displacement of the Qt1/Qt2 terrace riser by the Little Lake fault.

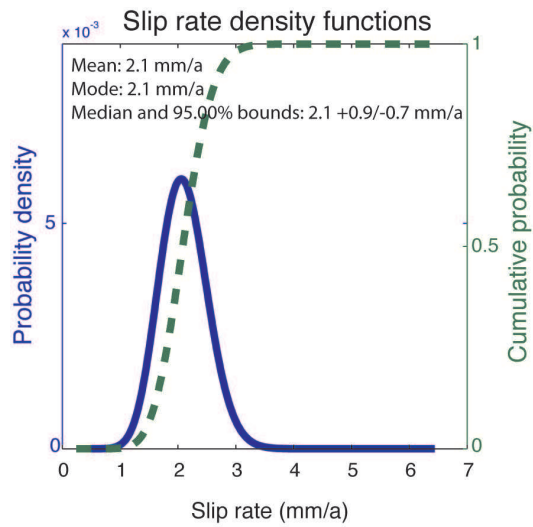


Figure 2.4: Probability density functions of fault slip rates computed from offset terrace risers and cosmogenic age constraints at Fossil Falls (Cerling, 1990).

3 Using Geodetic Data to Understand Postseismic Processes following the Sumatra-Andaman Earthquake

Kelly Grijalva, Roland Bürgmann, and Paramesh Banerjee (Earth Observatory of Singapore)

3.1 Introduction

Investigations of postseismic deformation are often plagued by ambiguities between fundamental deformation mechanisms that can be expected to contribute to the deformation, including viscous flow, localized afterslip and poroelastic rebound. Previous studies have explained the near-field postseismic deformation following the Sumatra-Andaman earthquake with afterslip or poroelastic rebound, and the far-field postseismic deformation with viscoelastic relaxation from both the 2004 M_w 9.2 and 2005 M_w 8.7 events. We aim to fit both the near and far-field data, spanning years 2005-2007, with a combination of postseismic mechanisms. We utilize campaign GPS data from *Gahalaut et al.* (2008) and continuous GPS data from the regional networks: NICT, SuGAR, and THAI.

3.2 Poroelastic Rebound

The strain field resulting from a coseismic dislocation produces changes in pore fluid pressure in the brittle upper crust. The subsequent decay of the excess pore-fluid-pressure gradients will lead to fluid flow and poroelastic deformation. We approximate the fully relaxed poroelastic response by subtracting the undrained solution for coseismic deformation from the drained solution for coseismic deformation. Based on earlier studies (e.g. *Masterlark*, 2003), the crust is assumed to be fluid-saturated down to 15 km depth. However, *Ogawa and Heki* (2007) propose that the downgoing slab releases fluids into the mantle wedge in sufficiently high quantities, with sufficiently large pore pressure diffusivities, to contribute to the poroelastic rebound during the early postseismic period. We therefore test a range of earth models, with undrained Poisson's ratio values 0.05 above the drained value for the top 15 km to 60 km of the lithosphere (Figure 2.5a).

3.3 Afterslip

We test afterslip models that range in depth from 10 km to 75 km, spanning the coseismic rupture planes and the downdip portion of the megathrust (Figure 2.5b). In general, the horizontal deformation is oriented towards the trench and magnitude of the deformation in the far-field increases with increased afterslip plane depth. When the afterslip plane is placed trenchward of the GPS site, there is vertical subsidence. Conversely, when the GPS site is located trenchward of the afterslip plane, there

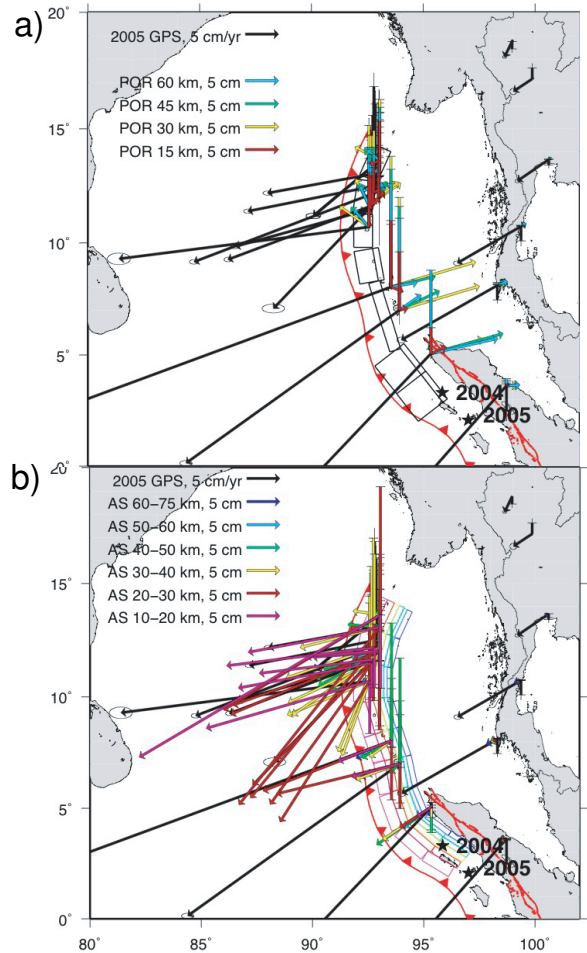


Figure 2.5: a) Modeled surface deformation due to a) poroelastic rebound and b) afterslip on the Sunda megathrust. The modeled displacements are compared with geodetic measurements over the year 2005.

is vertical uplift. Afterslip can be optimized to fit the near-field vertical and horizontal data with 1-2 m of slip. However, in order to fit the far-field sites in Thailand, it is necessary to have approximately 10 m of afterslip at 60-75 km depth.

3.4 Viscoelastic Relaxation

Deep-seated transient postseismic relaxation can produce time dependent deformation exceeding that from the earthquake itself in the intermediate-to-far field

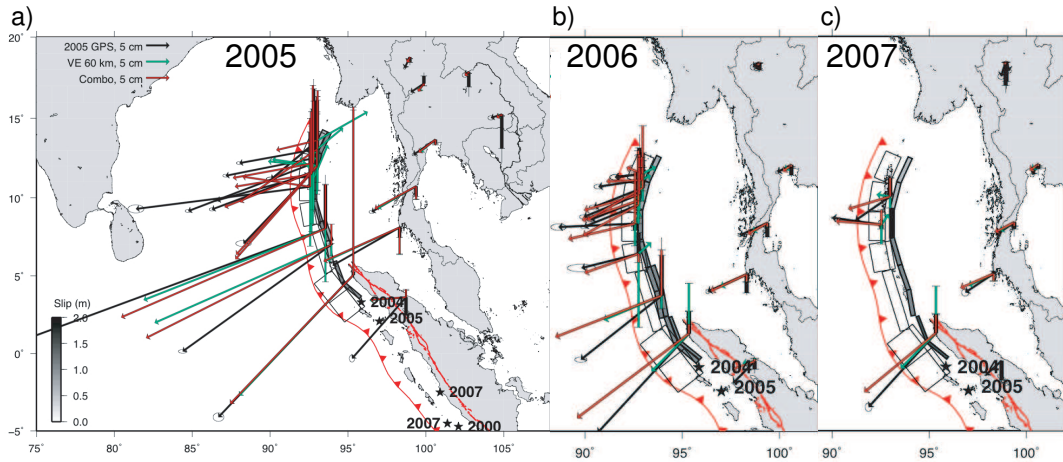


Figure 2.6: Comparison of a) 2005, b) 2006, and c) 2007 geodetic data with the preferred viscoelastic relaxation model and a combination model. The coseismic rupture planes for the Sumatra-Andaman earthquake are outlined in black (Banerjee *et al.*, 2007).

range. We test a range of earth models with the lithosphere-asthenosphere boundary (LAB) increasing from 50 km to 80 km in depth. Increasing the LAB decreases the magnitude of the surface deformation. The viscoelastic models can be optimized to fit the far-field data, but they poorly fit the near-field data. Our preferred LAB is 60 km because it is similar to previously published results (Pollitz *et al.*, 2006) and the subsidence in the Nicobar Islands helps to offset the modeled uplift from poroelastic rebound and afterslip. We find that our viscoelastic model fits the rate of decay at the Thai sites best with a transient asthenospheric viscosity of 2.5×10^{17} Pa s and a steady-state viscosity of 5×10^{18} Pa s.

3.5 Discussion

We discovered that the vertical component is more important than the horizontal component for diagnosing the near-field postseismic processes. For the Sumatra-Andaman earthquake, poroelastic rebound always has uplift in the near-field, afterslip can have either uplift or subsidence depending on the slip location, and viscoelastic relaxation always has both uplift and subsidence. Our preferred postseismic model for 2005 includes a combination of the 15 km-poroelastic rebound model, the 60 km-viscoelastic relaxation model, and between 0.5-1.5 m of afterslip (Figure 2.6a). For 2006 and 2007, we did not include poroelastic rebound in our preferred combination model. The 2006 combination model includes between 0.7-1.0 m of afterslip (Figure 2.6b) and the sparser 2007 data suggest that the afterslip location is continuing further downdip along the megathrust with cumulative slip magnitude of between 0.5-2.0 m (Figure 2.6c). The afterslip magnitude does not appear to have decayed significantly during our observation period from 2005-2007.

Overall, we find that the near-field and far-field data can not be fit by just one postseismic process and the vertical component is especially necessary for properly diagnosing the near-field postseismic deformation.

3.6 Acknowledgments

This work is supported by the National Science Foundation grant EAR 0738299. The GPS data is provided by the Tectonics Observatory, LIPI and SOPAC. The modeling programs are provided by Fred Pollitz.

3.7 References

- Banerjee *et al.*, Coseismic slip distributions of the 26 December 2004 Sumatra-Andaman and 28 March 2005 Nias earthquakes from GPS static offsets, *Bull. Seism. Soc. Am.*, *97*, S86-S102, 2007.
- Gahalaut *et al.*, GPS measurements of postseismic deformation in the Andaman-Nicobar region following the giant 2004 Sumatra-Andaman earthquake, *J. Geophys. Res.*, *113*, 10.1029/2007JB005511, 2008.
- Masterlark, T., Finite element model predictions of static deformation from dislocation sources in a subduction zone: Sensitivities to homogenous isotropic, Poisson-solid, and half-space assumptions, *J. Geophys. Res.*, *108*, doi:10.1029/2002JB002296, 2003.
- Ogawa, R. and K. Heli, Slow postseismic recovery of geoid depression formed by the 2004 Sumatra-Andaman Earthquake by mantle water diffusion, *Geophys. Res. Lett.*, *34*, doi:10.1029/2007/GL029340, 2007.
- Pollitz *et al.*, Post-seismic relaxation following the great 2004 Sumatra-Andaman earthquake on a compressible self-gravitating Earth, *J. Int.*, *167*, 397-420, 2006.

4 Interseismic Creep on the Concord Fault from PS-InSAR and SBAS

Ingrid Johanson, Roland Bürgmann, Alessandro Ferretti (TRE, Milan) and Fabrizio Novali (TRE, Milan)

4.1 Introduction

The Concord fault (CF) is part of the San Andreas fault (SAF) system in California’s San Francisco Bay Area. Its long-term slip rate of 7 ± 2 mm/yr (geodetically determined) represents about one-fifth of the total SAF system rate. The Concord fault also creeps at a rate of 2.5-3.5 mm/yr, determined from measurements at two alignment arrays (McFarland *et al.*, 2009). The alignment arrays also showed time-variable slip, with creep events occurring every 3-5 years. Measuring creep and its variability on the CF is important, not just for understanding the fault’s earthquake potential, but also because it may give us insight into how slip is transferred onto the Concord fault. The similarity in creep rate between the Northern Calaveras Fault (NCF) and CF, noted by Galehouse and Lienkamper (2003) is one line of evidence for linking the two.

We use PS-InSAR (Permanent Scatterer Interferometric Synthetic Aperture Radar) and the SBAS (Small Baseline Subset) technique to construct time series of ground motion around the CF and measure the creep rate along several profiles (Figure 2.7). The analysis is possible because of the extensive set of ERS data available through the WInSAR and GeoEarthScope archives. The PS-InSAR method identifies and integrates individual points that act like point scatterers and have stable phase measurements in a set of interferograms with a common master scene (starting date) (Ferretti *et al.*, 2001). The SBAS technique uses a set of interferograms with various master and slave scenes and provides time series of deformation at any consistently coherent pixel (Berardino, 2002).

4.2 Measuring creep from InSAR time series

We use 2 PS-InSAR datasets from descending tracks 70 and 342 from the European Space Agency’s ERS1 & 2 satellites, using 46 and 30 acquisitions, respectively, and spanning from 1992 through 2001. The data were processed using the PS-InSAR method of Ferretti *et al.* (2001) to produce time series of range change (change in distance between the ground and satellite) for each point as shown in Figure 2.7B & C. We also use a set of 22 ERS scenes from ascending track 478, arranged into a time series using the SBAS technique (Figure 2.7D).

To measure creep on the Concord fault, we look at motion along several profiles crossing the Concord fault. We use swath averaging to construct a profile at each time step of the InSAR time series (e.g. Figure 2.8).

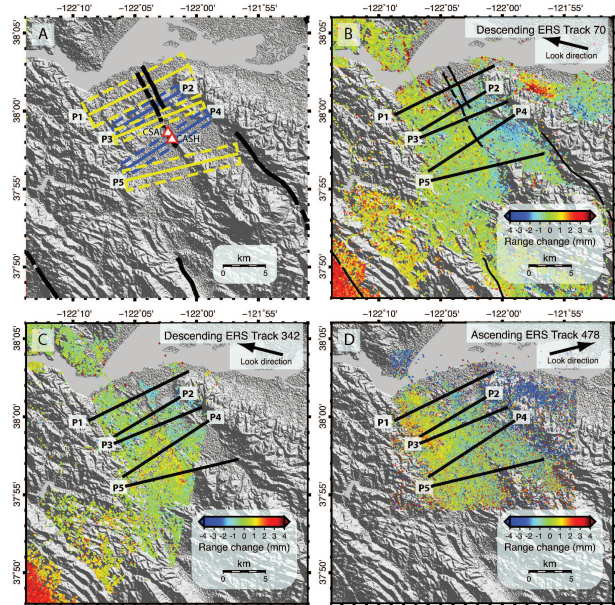


Figure 2.7: Overview map showing mean velocity of each PS-InSAR and SBAS dataset (B,C,D). Dashed boxes in subfigure A are the areas included in the swath averages, which are then projected onto the solid black centerlines. White triangles are alignment arrays CSAL and CASH.

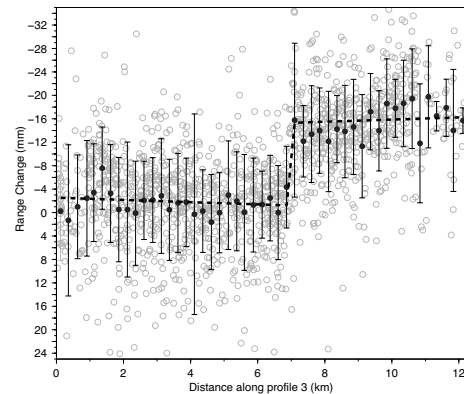


Figure 2.8: An example of a swath average profile for descending Track 70. Grey circles are the actual PS-InSAR points within the swath. Black circles are the calculated swath averages, with one sigma error bars. The dashed black line and offset is fit to the data by minimizing the least-squares residuals.

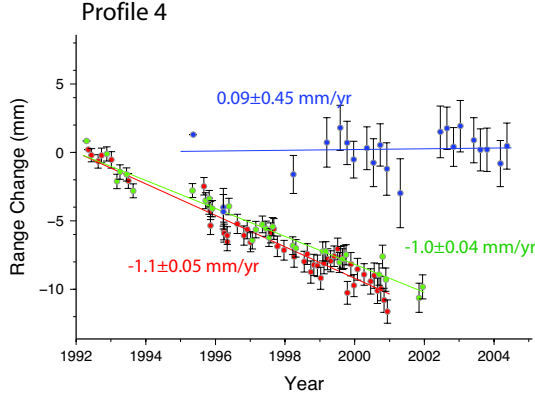


Figure 2.9: Range change across the trace of the Concord fault through time for all three datasets for one profile. Track 70 is shown in red, track 342 in green and track 478 is shown in blue. The secular creep rate as determined from a weighted linear inversion is printed next to each series.

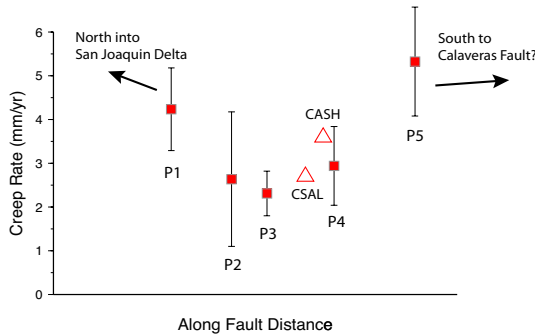


Figure 2.10: Calculated creep rates at each profile are shown according to their location along strike (red squares). Creep rates from alignment array measurements are shown as triangles.

Within each swath, shown as dashed lines in Figure 2.7A, points within 0.25 km bins perpendicular to the fault are averaged together and projected onto the centerline. For example, all points between 0.5 and 0.75 km west of the fault are averaged together to provide one point on the profile, and their standard deviation provides an estimate of the profile point's uncertainty.

A swath average profile is constructed for all acquisition dates in the three datasets and on each of the five profiles, for a total of 490 profiles. A linear inversion is performed on each profile to obtain the offset at the fault trace, produced by the shallowly creeping fault (dashed line in Figure 2.8). Each offset value represents the amount of creep on the Concord fault since the beginning of the time series.

4.3 Long-term creep rates

By fitting a line to the offsets, we can obtain a measurement of the secular range change rate at each profile (Figure 2.9). Using multiple viewing geometries (descending and ascending tracks) allows us to uniquely separate the range change into horizontal and vertical components. We assume horizontal motions are due to fault creep (Figure 2.10) and vertical motions represent hydrologic processes. All horizontal motion is taken to be parallel to the local strike of the Concord fault at each profile, as would be the case for pure strike-slip. The inversion of fault creep rate (V_{SS}) is set up as shown below.

$$RC = V_{SS} [\sin^2 \theta \cos \alpha + \cos \theta \sin \theta \sin \alpha] + V_V [\cos \theta]$$

$$RC = V_{SS} G_{SS} + V_V G_V$$

$$\begin{bmatrix} V_{SS} \\ V_V \end{bmatrix} = \begin{bmatrix} G_{SS} T_{70} & G_V T_{70} \\ G_{SS} T_{342} & G_V T_{342} \\ G_{SS} T_{478} & G_V T_{478} \end{bmatrix}^{-1} \begin{bmatrix} RC_{T70} \\ RC_{T342} \\ RC_{T478} \end{bmatrix} \quad (2.1)$$

The results for secular creep-rate (V_{SS}) for each profile are shown in Figure 2.10. The results are very consistent with the long-term creep rates obtained from the alignment array surveys. It would appear that creep rates increase toward the ends of the Concord fault trace; however all the creep rate measurements from InSAR profiles are within uncertainty of the alignment array derived rates (2.5-3.5 mm/yr).

4.4 References

- Berardino, P., G. Fornaro, R. Lanari, and E. Sansosti, A new algorithm for surface deformation monitoring based on small baseline differential SAR interferograms. *IEEE Trans. Geo. Rem. S.*, 40 2375-2383, 2002.
- Ferretti, A., C. Prati, and F. Rocca, Permanent scatterers in SAR interferometry, *IEEE Trans. Geosci. Remote Sens.*, 39, 8-20, 2001.
- Galehouse, J.S. and J. J. Lienkaemper, Inferences drawn from two decades of alignment array measurements of creep on faults in the San Francisco Bay Region. *Bull. Seismol. Soc. Am.*, 93(6), 2415-2433, 2003.
- McFarland, F., J. Lienkaemper, and S. J. Caskey, Data from theodolite measurements of creep rates on San Francisco Bay region faults, California; 1979-2009, *USGS Open file report 09-1119*, 2009.

5 Probing the Deep Rheology of Tibet Constraints from 2008 M_w 7.9 Wenchuan, China Earthquake

Mong-Han Huang and Roland Bürgmann

5.1 Introduction

Debate over the fundamental geological shape of the Tibetan Plateau has been running for many years. There are mainly two end-member models proposed: [1] The deformation in Tibet is diffuse and distributed, associated with ductile flow in the mantle and in the middle or lower crust (e.g., Royden *et al.*, 1997); [2] Tibet results from interactions among rigid blocks with localization of deformation along major faults (e.g., Avouac and Tapponnier, 1993). Both have major implications for the dynamics of plateau borders with different mechanisms for building up and supporting the mountain ranges. On 12 May 2008, a M_w 7.9 Earthquake occurred at Wenchuan in Sichuan Province, China, generating about 280 km of surface rupture (Shen *et al.*, 2009). More than 80,000 people were killed and over 4.8 million people became homeless due to this disastrous earthquake. The major faults involved in this event include the Pengguan fault in the east along the mountain front, the Beichuan fault about 10-15 km further to the west, and the Wenchuan-Maowen fault that lies about 30 km northwest of the Beichuan fault. They are all part of the Longmen Shan fault zone, which is located in the zone of crustal shortening between the Tibetan Plateau and the Sichuan Basin. The postseismic deformation is at least an order of magnitude less than the coseismic slip. The most significant postseismic deformation recorded at a continuous GPS station about 25 km away from the maximum rupture on the Beichuan fault shows 0.7 m coseismic offset but merely 0-6 mm of postseismic displacement in the 5 months following the event.

Postseismic deformation is considered to be a motion which is a response to the redistribution of stresses induced by an earthquake. In other words, the motion is evidence of the relaxation stress somewhere in the upper part of the lithosphere (Ryder *et al.*, 2007). There are various hypotheses suggesting the relaxation procedure, such as: afterslip on a discrete plane, creep in a viscous or viscoelastic shear zone, viscoelastic relaxation in the lower crust/upper mantle, and poroelastic rebound, etc. In this study, we will apply viscoelastic modeling using the VISCO1D code (Pollitz, 1992), and compare different rheological configurations with their responses to the postseismic surface deformation. The aim for doing numerical modeling is to find out a relevant rheological forward model that could explain the geodetic observations. In this way, we can understand the key parameters, especially the viscosity, which control the deformation process following an earthquake.

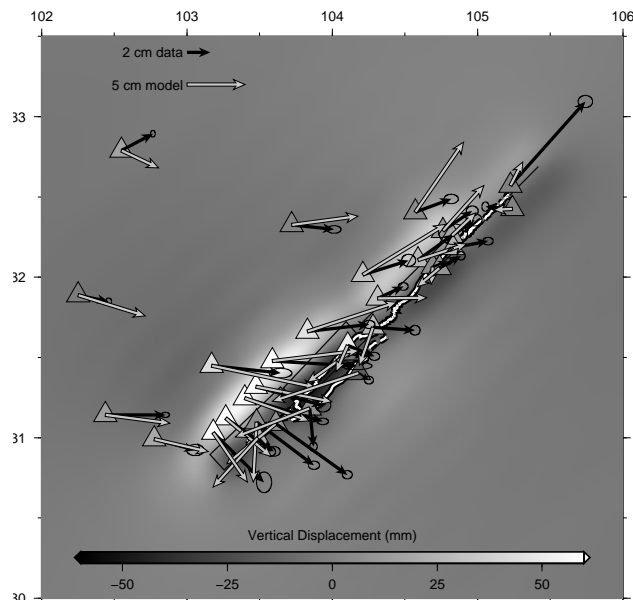


Figure 2.11: The GPS measurements and the forward modeling result of the Wenchuan postseismic deformation. The black arrows show the best fitting one year deformation from the GPS time series. The rectangles are the preferred earthquake fault model segments modified from Shen *et al.*, 2009, and the white lines are the surface rupture. The white arrows are the forward modeling using the Maxwell rheology according to Ryder *et al.*, 2008. The background colors are the vertical forward modeling, and the colors in the triangles are the one year GPS vertical measurements.

5.2 Primary Result and Discussion

Shen *et al.*, 2009 apply GPS and InSAR (Interferometric Synthetic Aperture Radar) inversion to find the best fault geometry and slip distribution. Here we simplify the Wenchuan coseismic fault geometry provided by Shen *et al.*, 2009 into 5 fault segments with different fault properties. According to coseismic studies (e.g., Shen *et al.*, 2009), all segments (Pengguan fault, Beichuan fault, and Wenchuan-Maowen fault) of the Longmenshen fault strike about 229° and dip to the NW. However, the dipping angle ranges from $\sim 43^\circ$ in the SW to nearly vertical in the NE. Moreover, the sense of motion varies from thrusting in the SW to right lateral strike-slip in the

NE. Most of the GPS stations were installed just after the Wenchuan main shock. We estimate the one year postseismic slips in terms of linear least square fit to the GPS time series. In this study, we consider viscoelastic rebound to be the main driving force of the postseismic deformation. The viscoelastic model calculation is based on the software VISCO1D (Pollitz, 1992). This program can build up the earth model with either elastic or viscoelastic properties specified by users for Maxwell or Burgers rheological models. We consider the rheological model suggested by *Ryder et al.*, 2007 and *Godard et al.*, 2009 as the starting conditions. [1] *Ryder et al.*, 2007 study the post 1997 M_w 7.6 Manyi (Tibet) earthquake surface deformation in terms of SAR interferometry. They assume a 15 km elastic lid over a viscoelastic half-space, and the shear modulus is held constant at 5×10^{10} Pa. Their best fitting viscosity of the half-space (Maxwell rheology) is 7×10^{18} Pa s. [2] *Godard et al.*, 2009 explore the viscoelastic properties of the borders of Tibetan Plateau (the Sichuan and Tarim basins, for example) in terms of thermomechanical modeling of continental lithosphere coupled with fluvial denudation. They propose a viscoelastic model that has a 15 km elastic lid over the lower crust (viscosity: 10^{20} Pa s) and the upper mantle with viscosity decreasing in depth. We simplify their proposed viscosity model to include 4 layers: elastic lid, lower crust (viscosity: 10^{21} Pa s), upper-most mantle (viscosity: 10^{22} Pa s), and upper mantle (viscosity: 10^{18} Pa s).

Afterslip and poroelastic rebound are additional important mechanisms that contribute to postseismic deformation. Poroelastic rebound generally shows relatively localized postseismic slips near the fault rupture zone and is related to Poisson's ratio and shear modulus, etc. (*Freed et al.*, 2006). Afterslip represents accelerated aseismic slip on and adjacent to the main shock rupture. In this study, we also test for contributions from these two processes to the postseismic deformation. The afterslip distribution inverted from the postseismic GPS data can explain the near-field postseismic displacement in terms of afterslip on the deeper part of the Beichuan fault. However, this model is not able to fit the far-field transients, which might be dominated by the viscoelastic deformation. A first-order model of poroelastic rebound in terms of changing the Poisson's ratio in coseismic forward dislocation models from 0.29 (undrained) to 0.25 (drained) leads to surface deformation with only up to 6 mm horizontal and 1 mm vertical deformation at near-field GPS stations. The modeled poroelastic rebound can only contribute about 1/5 of the observed postseismic deformation and thus cannot be the primary source of the postseismic deformation. Our future work will involve careful exploration of how a combination of viscoelastic flow, poroelastic rebound and afterslip produces the observed transients, so that we will be able to characterize

the relative importance of each mechanism at different scales of postseismic deformation and quantify the rheological parameters of the underlying processes.

5.3 Acknowledgements

We thank Z.K. Shen for providing the GPS time series. This work is supported by NSF grant (EAR 0738298).

5.4 References

- Avouac, J.P. and Tapponnier, P., Kinematic model of active deformation in Central Asia, *Geophys. Res. Lett.*, *20*, 895-898, 1993.
- Bürgmann, R. and Dresen, G., Rheology of the Lower Crust and Upper Mantle: Evidence from Rock Mechanics, Geodesy, and Field Observations, *Annu. Rev. Earth Planet. Sci.*, *36*, 531-67, doi:10.1146/annurev.earth.36.031207.124326., 2008.
- Freed, A., Bürgmann, R., Calais, E., Freymueller, J., and Hreinsdottir, S., Implications of deformation following the 2002 Denali, Alaska, earthquake for postseismic relaxation processes and lithospheric rheology, *J. Geophys. Res.*, *111*, B01401, doi:10.1029/2005JB003894.i, 2006.
- Godard, V., Cattin, R., and Lave, J., Erosional control on the dynamics of low-convergence rate continental plateau margins. *Geophys. J. Int.*, *179*, 763-777, doi: 10.1111/j.1365-246X.2009.04324.x., 2009.
- Pollitz, F., Postseismic relaxation theory on a spherical earth. *Bull. Seism. Soc. Am.*, *82*(1), 422-453, 1992.
- Royden, L.H., Burchfiel, B.C., King, R.W., Wang, E., Chen, Z.L., Shen, F., and Liu, Y.P., Surface deformation and lower crustal flow in eastern Tibet, *Science*, *276*, 788-790, 1997.
- Ryder, I., Parsons B., Wright T.J., and Funning G., Post-seismic motion following the 1997 Manyi (Tibet) earthquake: InSAR observations and modeling, *Geophys. J. Int.*, *169*, 1009-1027, doi: 10.1111/j.1365-1246X.2006.03312.x., 2007.
- Shen, Z.K., J. Sun, P. Zhang, Y. Wan, M. Wang, R. Bürgmann, Y. Zeng, W. Gan, H. Hiao, and Q. Wang, Slip maxima at fault junctions and rupturing of barriers during the 2008 Wenchuan earthquake, *Nat. Geosci.*, *2*, 718-724, doi:10.1038/NCEO636, 2009.

6 Tidal Triggering of LFEs near Parkfield, CA

Amanda M. Thomas, Roland Bürgmann, and David Shelly

6.1 Introduction

Studies of nonvolcanic tremor (NVT) in Japan, Cascadia, and Parkfield, CA have established the significant impact small stress perturbations, such as the solid earth and ocean tides, have on NVT generation (*Thomas et al.*, 2009). Similar results irrespective of tectonic environment suggest that extremely high pore fluid pressures are required to produce NVT. Here we analyze the influence of the solid earth and ocean tides on a catalog of 500,000 low frequency earthquakes (LFE) distributed along a 150km section of the San Andreas Fault centered at Parkfield (*Shelly and Hardebeck*, 2010). LFEs comprising the tremor signal are grouped into families based on waveform similarity and precisely located using waveform cross-correlation. Analogous to repeating earthquakes, LFE families are thought to represent deformation on the same patch of fault. While the locations of repeating earthquakes are assumed to be coincident with the location of asperities in the fault zone, NVT occurs below the seismogenic zone, where fault zones behave ductilely. Here we explore the sensitivity of each of these LFE families to the tidally induced shear (right-lateral shear stress, RLSS), normal (fault-normal stress, FNS), and Coulomb (CS) stresses on the SAF.

6.2 Methods

Tidally induced strains are computed in the LFE source region using SPOTL. Assuming two-dimensional plane strain and linear elasticity, with an elastic modulus of 30 GPa and Poisson ratio of 0.25, strains are then converted to stresses and resolved into fault normal and parallel (shear) directions of the San Andreas fault (N°45W), and the volumetric strain is converted to pressure. Timeseries of the resolved stresses are then used to compute the percent excess [= (actual number of LFEs that occur under a particular loading condition - expected number) / expected number] for each stress constituent. We compute the percent excess, or Nex, for each stressing condition. Additionally, relative tremor rates during times when the tides are encouraging or retarding failure can be used to estimate the effective normal stress (*Dieterich*, 1986). The precisely relocated LFE families allow us to map spatial variation of the aforementioned quantities in the deep San Andreas fault.

6.3 Preliminary Results

Preliminary results indicate that extremely small stresses induced in the lithosphere by the tides are suffi-

cient to trigger/modulate LFE families on the deep SAF. Additionally, precise LFE locations coupled with tidal influence on LFE families can be used to produce maps of along-fault spatial variability in tidal sensitivity, friction, and effective normal stress (Figure 2.12). The tidally induced RLSS has the most robust influence on LFE generation, however many families also show statistically significant correlation or anti-correlation with FNS. All families exhibit near-lithostatic pore pressure.

Future research efforts will focus on using tidal sensitivity of LFEs to place controls on the mechanical properties and behavior of deep fault zones.

6.4 Acknowledgements

This work is funded by the United States Geological Survey and a National Science Foundation Graduate Research Fellowship.

6.5 References

- Dieterich, J.H., Nucleation and triggering of earthquake slip: effect of periodic stresses, *Tectonophysics*, 144, 127-139, 1986.
- Shelly, D.R. and J.L. Hardebeck, Precise tremor source locations and amplitude variations along the lower-crustal central San Andreas Fault, *Geophys. Res. Lett.*, 37, L14301, 2010.
- Thomas, A.M., R.M. Nadeau, and R. Bürgmann, Tremor-tide correlations and near-lithostatic pore pressure on the deep San Andreas fault, *Nature*, 462, 1048-1051, 2009.

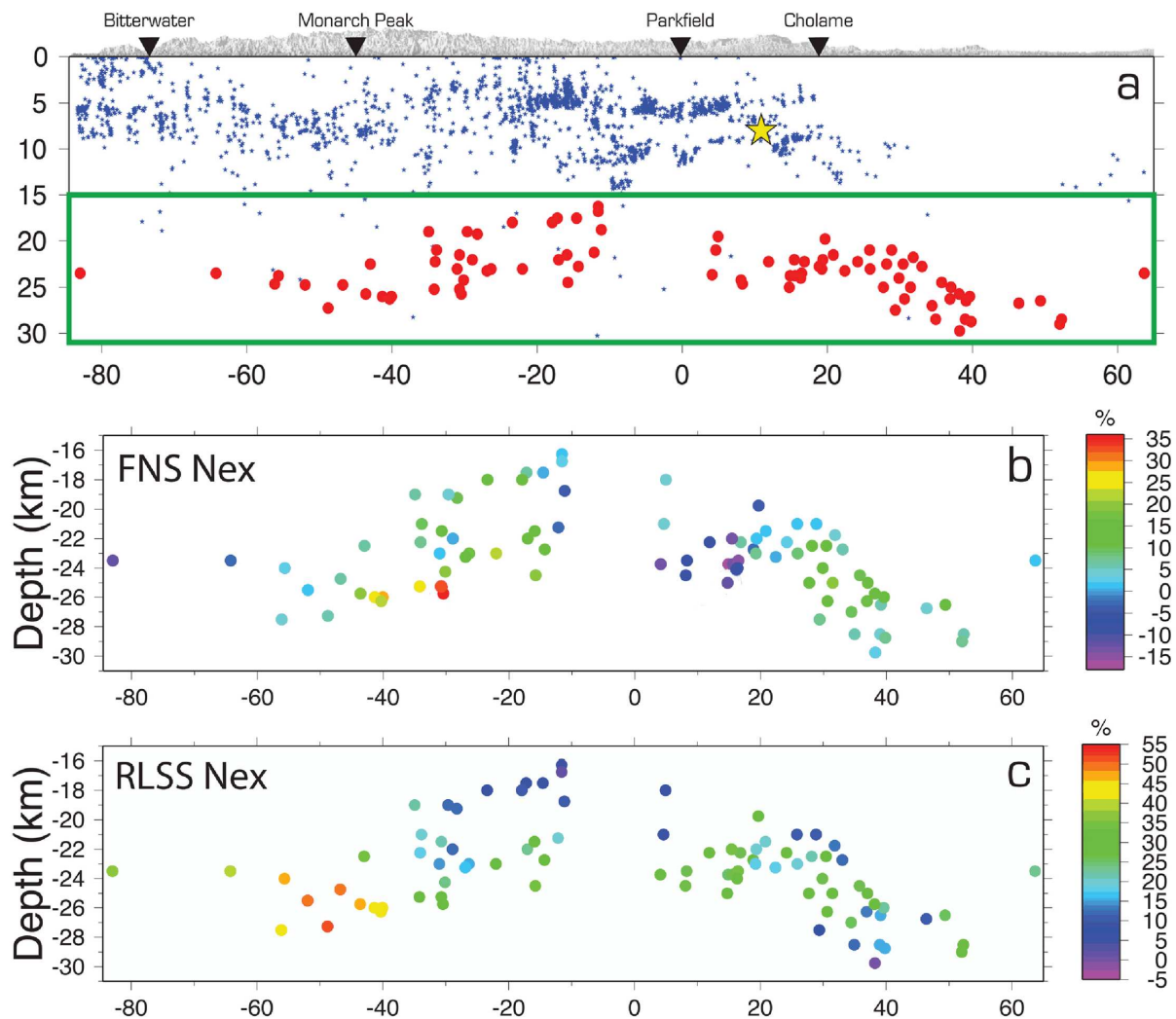


Figure 2.12: (a) Along-fault cross section of the SAF viewed from the south-west. Vertically exaggerated topography is shown in grey. Local towns are marked by inverted triangles. Hypocenters of SAF seismicity, the 2004 Parkfield earthquake, and LFE locations are shown as blue dots, yellow star, and red circles respectively. Panels (b) and (c) are delineated by the green box. (b) LFE locations color coded by their FNS Nex (percent excess = [actual number of LFEs during times of positive FNS - expected number of LFEs during times of positive FNS]/expected number of LFEs during times of positive FNS). (c) LFE locations color coded by the RLSS Nex values. (See color version of this figure at the front of the research chapter.)

7 Monitoring Slow Moving Landslides in the Berkeley Hills with TerraSAR-X Data

Ling Lei and Roland Bürgmann

7.1 Introduction

Resolving the kinematics of landslides is a prerequisite for improving our understanding of the mechanics of these potentially hazardous features. We need to better understand how landslides destabilize during large rainstorms and seismic events. In the Berkeley Hills there are four large, slow moving, deep-seated landslides. All the landslides extend through residential areas and move on the order of cm/year, each covering an area of roughly $0.25\text{-}1.00\text{km}^2$. These slides are located in a rapidly uplifting zone adjacent to the Hayward fault (Figure 2.13). A lot of damage to homes, breakage of underground utility pipes, and confusion over property lines was caused by landslides over the years, although deformation on these landslides is typically small and slow. It is currently not well understood how the landslides respond to seismic activity on the Hayward fault. DInSAR (Differential Interferometric Synthetic Aperture Radar) is a powerful tool for measuring movements of ground by exploiting the phase difference of SAR images taken at different time instances. In this project, we aim to monitor the Berkeley Hills landslides using SAR data from a number of different satellites, especially TerraSAR-X.

7.2 TerraSAR-X Data Set

The TerraSAR-X satellite, launched on June 15, 2007, carries an X-band SAR operating at 9.65 GHz. One of the main goals of the TerraSAR-X mission is to produce high resolution imagery with near optical quality. The antenna on TerraSAR-X can be steered in both elevation and azimuth and can be used to generate Spotlight, Stripmap and ScanSAR images. Spotlight images have a resolution of about 1 meter, while Stripmap data have a ground resolution between 2 meters and 6 meters, and ScanSAR images have a resolution of approximately 16 meters. The satellite operates in an 11 day repeat orbit at an altitude of 514 km. The rather short orbit repeat cycle and the electronically steerable antenna allow fast and frequent imaging of a particular site. The frequent interferometric coverage can help especially with monitoring events on shorter time scales. Fast events can be detected and atmospheric delay errors can be reduced by averaging many interferograms.

Up to now, we have ordered and received 90 TerraSAR-X Spotlight Single Look Complex (SLC) images and a few Stripmap SLC images delivered by DLR. The TerraSAR-X images were acquired over the active landslides, coastal subsidence and shallow Hayward fault

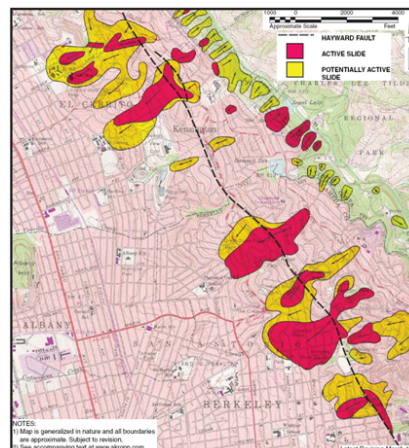


Figure 2.13: Map of active landslides of the Berkeley Hills (<http://www.akropp.com/resources>)

creep near the city of Berkeley. The data acquisition interval is from November, 2008 till now. Four types of Spotlight images and one type of Stripmap images in time sequence were ordered and acquired: spot_012, spot_038, spot_049, spot_075 and strip_003, with HH polarization, different look angles, and different pass directions.

We use ROLPAC to do the Interferometric processing. We used a two-pass differential interferometry approach using SRTM 1-arc-second DEM heights as a reference to calculate the topographic phase. From the analysis of a map of phase coherence values, we find high coherence values in urban areas but low values in the hills and more vegetated areas which caused phase unwrapping problems in the landslides area. Thus, a time series of interferograms was used for the atmospheric correction. We used sequential interferograms to do the stacking, which means that every image appears in two interferograms except the first and last image. We obtained preliminary results from Stripmap interferograms and standard stacking of Spotlight interferograms. The results are generally consistent with southwest motion of the landslides.

7.3 Persistent Scatterer Processing

While standard InSAR measurements that rely on one or a stack of several interferograms can resolve the motion of large landslides, this method is still often hampered by significant noise introduced by atmospheric delays and by loss of coherence in vegetated or high-relief terrain. The persistent scatterer approach can enhance the ability to find suitable scatterers in relatively low-coherence ter-

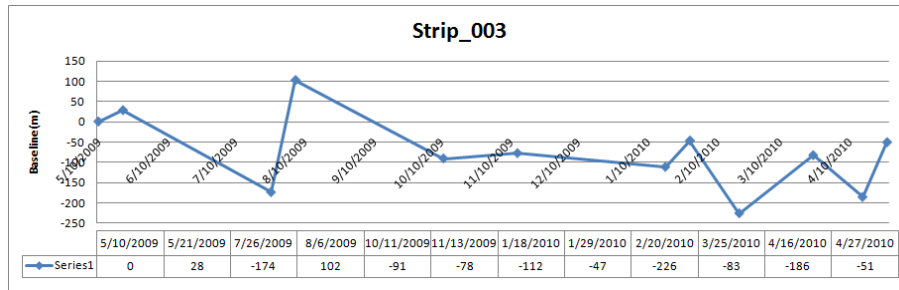


Figure 2.14: Acquisition dates and perpendicular baseline

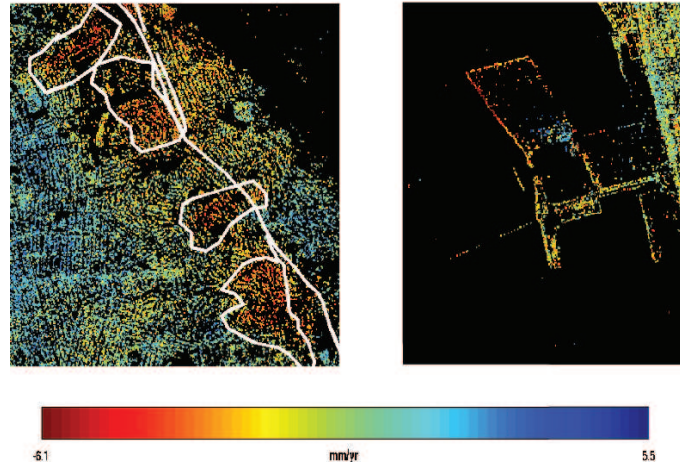


Figure 2.15: Mean LOS velocity of the landslides area and Berkeley Marina

rains. We use Stanford Method for Persistent Scatterers (StaMPS) which was developed at Stanford University by Dr. Andy Hooper (*Hooper et al.*, 2004). Since we do not have many Strimap acquisitions yet, we only used 12 scenes, which span the time interval from May 2009 to April 2010, for our analysis. We constructed eleven interferograms relative to the master scene of May 10, 2010 with Doris (Delft Object-oriented Radar Interferometric Software). All of these images were used to identify persistent and coherent pixels. Figure 2.14 shows the acquisition date and baseline information. The wrapped phase of the PS pixels is selected and the improved phase unwrapping algorithm is adopted.

The negative mean Line-of-sight (LOS) velocity in the landslides area (Figure 2.15) is consistent with landslide motion, moving away from the satellite. Also, the negative LOS velocity reveals subsidence of the Berkeley marina area. For our future work, we hope the four beams of TerraSAR-X Spotlight data from different viewing geometries will significantly improve our ability to fully characterize the kinematics and temporal patterns of the landslides. We are still in the early stages of this investigation and will acquire more data to do the PS processing. Results from TerraSAR data will be carefully compared and integrated with InSAR data from other spacecraft, including the ERS-1/2, Envisat, RADARSAT-1,

and ALOS satellites.

7.4 Acknowledgements

We thank the German Aerospace Centre (DLR) for providing TerraSAR-X data for this project. We thank Paul Lundgren, Eric J. Fielding, and Paul Rosen for providing TerraSAR reading codes and beneficial discussions. We thank Andy Hooper for supporting StaMPS software.

7.5 References

- Hilley, G., R. Bürgmann, A. Ferretti, F. Novali and F. Rocca, Dynamic of slow-moving landslides from permanent scatterer analysis, *Science*, 304, 1952-1955, 2004.
- TerraSAR-X Ground Segment Basic Product Specification Document, TX-GS-DD-3302.
- Bürgmann, R., E. Fielding, and J. Sukhatme, Slip along the Hayward fault, California, estimated from space-based synthetic aperture radar interferometry, *Geology*, 26, 559-562, 1998.
- Eineder, M., N. Adam, and R. Bamler, Spaceborne Spotlight SAR Interferometry With TerraSAR-X, *IEEE Trans. Geosci. Remote Sense.*, 5, 1524-1535, 2009.
- Hooper, A., H. Zebker, P. Segall and B. Kampes, A new method for measuring deformation on volcanoes and other natural terrains using InSAR persistent scatterers, *Geophys.*, 31, 2004.

8 Slab-Plume Interaction Beneath the Pacific Northwest

Mathias Obrebski, Richard Allen, Mei Xue (Tongji University, China), Shu-Huei Hung (National Taiwan University)

8.1 Introduction

The Pacific Northwest of western North America is unusual in that both a subducting slab and a hotspot occur within 1000 km of one another. Globally, these geologic components are commonly separated into distinct provinces. The Juan de Fuca (JdF) plate that continues to subduct today is a remnant corner of the Farallon plate and is terminated to the south by the Mendocino Triple Junction (MTJ). Subduction beneath the Pacific Northwest has been continuous for more than 150 Ma. The westernmost US exhibits several major Neogene to Quaternary volcanic provinces. The Columbia River Basalts (CRB) is the product of a phase of massive volcanic outpouring that occurred 17 Ma. The Yellowstone Snake River Plain (YSRP) hosts a bimodal volcanic trend that exhibits a time progressive sequence of volcanic centers. Two groups of hypotheses have been proposed to explain this surface geology: a stationary deep-seated whole mantle plume, or various lithospheric-driven processes of fracture and volcanism. Nevertheless, seismic imaging efforts to constrain the geometry of any Yellowstone plume anomaly through the mantle have been inconclusive. Here we take advantage of the Yellowstone region being now well covered by the dense USAarray deployment to provide constraints on the source of the hotspot, the process of subduction, and the inevitable interaction between the two in the mantle beneath the Pacific Northwest.

8.2 Data and Method

To image the Earth's interior beneath the Pacific Northwest, we use all of the available Earthscope-USArray data recorded from January 2006 to July 2009. The station coverage extends from the west coast to 100°W and from the Mexican border to the Canadian border. We also processed the data from two Earthscope temporary arrays (FlexArray Along Cascadia Experiment for Segmentation [FACES] and the Mendocino Experiment) deployed along the Cascadia trench and permanent seismic networks in the western US. The velocity structure of the mantle is retrieved through body wave finite frequency tomographic inversion. The dataset of our multi-frequency compressional model DNA09-P is derived from 58,670 traveltimes of direct P from 127 earthquakes measured in four frequency bands. The dataset used for our shear model DNA09-S includes 38,750 travel-time measurements, 34,850 S-wave observations from 142 events and 3,900 SKS observations from 24 events.

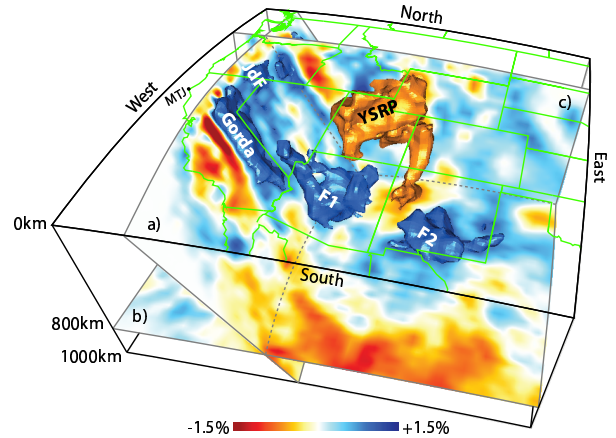


Figure 2.16: Tomographic 3D view of the DNA09 P-wave velocity structure of the mantle beneath the Pacific Northwest. a) is an oblique section through the currently subducting Gorda-Juan de Fuca slab (JdF) that clearly shows the southern edge of the slab beneath the Mendocino Triple Junction (MTJ). b) is a constant depth slice at 800km that illustrates the contrast between dominantly high velocity mantle to the north and slow velocities to the south where the Farallon slab is no longer present. c) is an E-W vertical slice at 46.5°N. 3D blue isosurfaces show strong fast anomalies linked to the Gorda-JdF slab and to possible Farallon fragments (F1-F2). The red isosurface depicts the 3D geometry of a large slow anomaly that extends from beneath the Yellowstone-Snake River Plain (YSRP) hotspot track to the bottom of our model at 1000km depth and that we interpret as a mantle plume.

8.3 Result and Interpretation

We interpret the low velocity anomaly beneath the YSRP as a mantle plume with a lower mantle origin. Our interpretation, based on geometrical observations of our P- and S-wave models, is also supported by the high He3/He4 isotopic ratio typical of the YSRP volcanism (Graham *et al.*, 2004), which is often interpreted as indicative of a lower mantle source. The low velocities are consistent with high temperatures and low density. A hot plume with a large volume of low density material, as observed in our models, accounts for the high heat flow, the broad topographic swell, the geoid high, and the large free air gravity anomaly observed in the YSRP area (Smith *et al.*, 2009 and references therein), and also

the 410km mantle discontinuity that deepens by 10km in this region (Fee and Dueker, 2004). The geometry and structure of the elongated slow anomaly observed in the upper 200km beneath the YSRP are consistent with the predictions of numerical models for the deflection of a plume head by the motion of an overlying lithospheric plate (Steinberger *et al.*, 2004). It is elongated in the SW-NE direction parallel to the motion of the North American plate, the amplitude of the slow anomalies decreases to the southwest with increasing age of the calderas, and the plume conduit today coincides with active volcanism in the Yellowstone Caldera.

The geometry of the Cascadia subduction zone, namely the length and amplitude of the slab anomaly, displays north-south variations (Figure 2.16). In particular, the slab is virtually absent deeper than 300 km beneath Oregon, and is thus too short to act as a mechanical barrier to upper-mantle flow. This gap in the trench may allow the mantle underlying the JdF plate to flow eastward beneath the plate margin as the North American plate moves southwestward above it. This provides a possible explanation for the trench-normal fast direction of anisotropy retrieved from SKS splitting analysis in central and northern Cascadia (Eakin *et al.*, 2010). The orientation of the fast direction in central and northern Cascadia differs from most other subduction zones where the fast direction is trench-parallel (Long and Silver, 2009). The Gorda-Juan de Fuca slab is thought to be in trench rollback, and it has been suggested that the Gorda slab plays a significant role. This is consistent with our model, where the Gorda slab dives deeper into the mantle and exhibits a faster anomaly, potentially indicative of cooler and denser material. Finally, the Cascadia subduction zone is also unusual due to the near-absence of deep seismicity. The fragmentation of the slab may play a role. There is no recorded seismicity deeper than 35km beneath Oregon, where the depth extent of the slab is only 300 km, thereby reducing the slab pull force usually responsible for intermediate depth down-dip-tension earthquakes. There is some sub-crustal seismicity beneath Northern California and beneath northern Washington, where the slab is imaged deeper into the mantle.

The analysis of the geometry of our tomographic models suggests that the arrival and emplacement of the large Yellowstone plume had a substantial impact on the nearby Cascadia subduction zone, promoting the tearing and weakening of the JdF slab. The existence of a whole-mantle plume and an active subduction zone within 1000km of one another as imaged in our models makes the tectonic setting of the Pacific Northwest unique. Also striking is the substantial fragmentation of the slab. The latitude where the slab is absent coincides with that of the Yellowstone plume (Figure 2.16). Around 19 Ma, there was a substantial change in the spreading rate at the Pacific-JdF ridge and also in the

convergence rate of the Cascadia trench (Wilson, 1988). This change could result from a reduction in slab pull. The change also shortly predates the massive magma outpouring of the Columbia River Basalts and the onset of volcanism along the YSRP, which have been interpreted as the manifestation of Yellowstone plume head emplacement (Smith *et al.*, 2009) around 17 Ma. We thus propose that the ascent of the Yellowstone plume, and its necessary encounter with the JdF slab, contributed to a rupture of the slab (Xue and Allen, 2007) (Figure 2.16) and the subsequent reduction of slab pull in the Cascadia trench. The composition of the CRB requires the presence of oceanic crust in the source (Takahahshi *et al.*, 1998), which supports the hypothesis that the Yellowstone plume interacted with the JdF slab and carried fragments of oceanic crust back up to the melting zone. This interpretation also explains several intriguing geophysical properties of the Cascadia trench that contrast with most other subduction zones, such as the absence of deep seismicity and the trench-normal fast direction of mantle anisotropy.

8.4 Acknowledgements

We thank USArray TA for data collection and the IRIS DMC for data distribution. This work was supported by the National Science Foundation and a UC-National Laboratory Research program grant.

8.5 References

- Eakin, C.M., M. Obrebski, R. M. Allen, D. C. Boyarko, M. R. Brudzinski, R. Porritt, Seismic anisotropy beneath Cascadia and the Mendocino triple junction: Interaction of the subducting slab with mantle flow, *Earth Planet. Sci. Lett.*, doi:10.1016/j.epsl.2010.07.015, 2010.
- Fee, D. and K. Dueker, Mantle transition zone topography and structure beneath the Yellowstone hotspot, *Geophys. Res. Lett.*, 31, L18603, doi:10.1029/2004GL020636, 2004.
- Graham, D. W., M. R. Reid, B. T. Jordan, A. L. Grunder, W. P. Leeman, and J. E. Lupton, Mantle source provinces beneath the Northwestern USA delimited by helium isotopes in young basalts, *J. Volcanol. Geotherm. Res.*, doi:10.1016/j.jvolgeores.2008.12.004, 2009.
- Smith, R. B., M. Jordan, B. Steinberger, C. M. Puskas, J. Farrell, G. P. Waite, S. Husen, W. L. Chang, and R. O'Connell, Geodynamics of the Yellowstone hotspot and mantle plume: Seismic and GPS imaging, kinematics, and mantle flow, *J. Volcanol. Geotherm. Res.*, 188, 26-56, 2009
- Steinberger, B., R. Sutherland, and R. J. O'Connell, Prediction of Emperor-Hawaii seamount locations from a revised model of global plate motion and mantle flow, *Nature*, 430, 167-173, 2004
- Takahahshi, E., K. Nakajima, and T. L. Wright, Origin of the Columbia River basalts: Melting model of a heterogeneous mantle plume head, *Earth Planet. Sci. Lett.*, 162, 63-80, 1998

9 Imaging Shallow Cascadia Structure with Ambient Noise Tomography

Robert W. Porritt and Richard M. Allen

9.1 Introduction

Along strike variation has been observed throughout the Cascadia Subduction Zone in multiple studies with a variety of data sets. Body-wave tomography shows a broad zone in the center of the slab beneath Oregon with a weak high velocity signal in an atypically quiescent seismic zone (*Obrebski and Allen, 2009*). Characteristics of primitive basalts found in the arc volcanoes change along strike, defining four distinct magma sources or plumbing systems (*Schmidt et al, 2007*). However, the most striking variation is in the recurrence rate of episodic tremor and slip throughout the region (*Brudzinski and Allen, 2007*). These separate observations may reflect lithospheric variations on a regional scale. This study seeks to connect these previous observations by developing a short period surface wave model of structure in the region using ambient seismic noise as the source.

9.2 Data Processing

Data for this study comes from the Berkeley Digital Seismic Network, the Southern California Earthquake Center, the Canadian National Seismic Network, and USArray with focus on two Flexible Array Experiments. The Flexible Array deployments, FlexArray Along Cascadia Experiment for Segmentation (FACES) and Mendocino Broadband, were deployed in 2007 and have completed their deployments as of summer 2010. This is one of the first studies utilizing the approximately one hundred stations in these broadband experiments.

Detailed processing flow for computing group and phase velocity maps can be found in *Benson et al (2007)*. While the typical measurements from 7-40 seconds were well constrained from signal-to-noise ratio (SNR) and wavelength criterion, in order to obtain reliable longer period measurements (40-92) seconds, the empirical Green's functions and measured dispersion curves were checked manually to ensure that the measurements were reasonable and consistent with realistic Earth models. The inter-station dispersion curves were inverted with a ray theoretical approach onto a 0.1° by 0.1° grid with a smoothing radius of one wavelength for each period from 7-92 seconds. Initial models exhibited strongly biased maps with clear artifacts from the heterogeneous distribution of noise sources. This bias was removed by binning the paths into 15° bins, normalizing the number of paths in each bin, and applying post-inversion smoothing regularization. To estimate the uncertainties in the phase and group velocity maps, a bootstrapping procedure was applied by randomly choosing 70% of the paths

to invert and repeating the process 30 times.

Dispersion curves over the model space and their corresponding uncertainties from the bootstrapping and a static value proportional to period are utilized in a Monte Carlo inversion scheme (*Shapiro and Ritzwoller, 2002*). The inversion used PREM (*Dziewonski and Anderson, 1982*) as a starting model in the mantle and GIL7 (*Dreger and Romanowicz, 1994*) in the crust. Crustal thickness was imposed from the receiver function model of *Levanter et al. (2008)*. Slab depth estimates from *Audet et al (2009)* were also used for better constraints in the subduction zone.

9.3 Results

It is not possible to discuss all the features of the model in this short summary; instead we discuss just two key areas of interest. Figure 2.17 details the crustal structure of the Klamath Mountain range. These mountains primarily overlay the Gorda plate portion of the Gorda-Juan de Fuca system, and the region has the shortest tremor recurrence interval of the Cascadia Subduction Zone at 10 months. The fastest velocities in the crust are around 3.6km/s and occur around 20km deep in the core of the mountains. The variability of the top of the Gorda slab with respect to the crustal variations implies some dynamic system of crust-mantle interaction in this zone.

Figure 2.18 details the three dimensional structure of the Siletzia terrain. This piece of accreted ocean terrain is often seen in high-resolution 2D active source studies (*Trehu et. al, 1994*), and anomalies in geochemical studies are often attributed to it. This study clearly illustrates the structure in a 3D capacity. From this it is clear the Siletzia terrain consists of high velocity material above the plate interface which may be driving the very long recurrence interval of episodic tremor and slip.

Comparing the structure of the two regions can provide insight into the observed variations. The Klamath range is overall slower than the Siletzia. While mapping velocity to rheology is a non-unique process, in general the low shear velocity could be due to a higher silicic or fluid content, or lower shear modulus, both of which imply a lower density and thus less compressive stress on the plate interface. Both of these factors are probable causes for an area to be more likely to have non-volcanic tremors. Future studies, such as receiver function analysis for V_p/V_s ratio and tomographic V_p and V_s studies will further improve our constraints on the region.

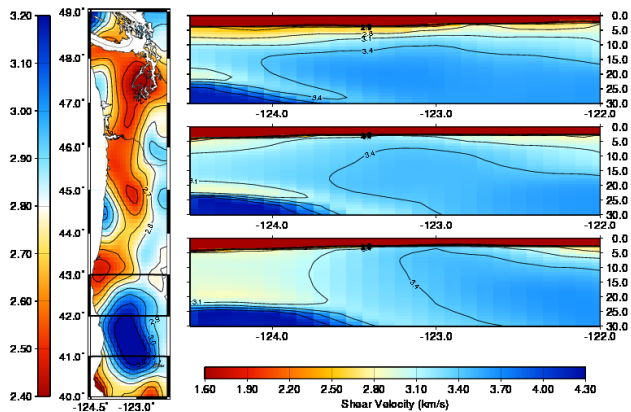


Figure 2.17: Slices to illustrate the structure of the Klamath terrain. Left: Map slice at sea level. Right: Sections of constant latitude showing high velocity mountain core and the top toe of the subducting slab.

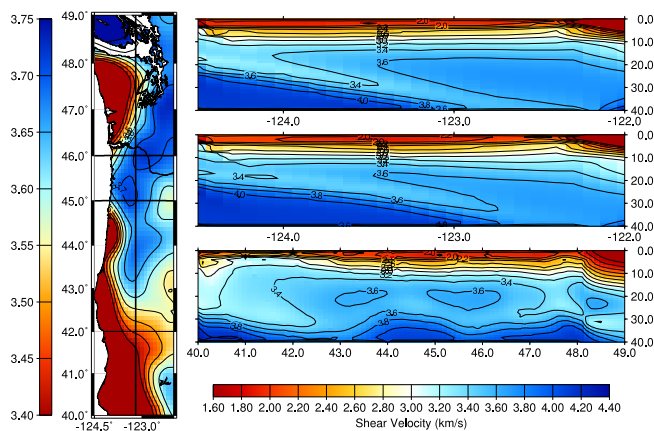


Figure 2.18: Slices illustrating the 3D structure of the Siletzia terrain. Left: Map slice at 15km. Right bottom: Cross section at 123°W longitude. Right top and middle: Cross sections at 46°N and 45°N respectively.

9.4 Acknowledgements

We would like to acknowledge our co-PIs and collaborators on the flexible array experiments. The Mendocino Broadband experiment was made possible through NSF grants EAR0643392 and EAR0745934, with help from Gene Humphreys, Leland O’Driscoll, Alan Levander, and Yongbo Zhao for fieldwork and discussions. The FlexArray Along Cascadia was funded through NSF grant EAR0643007 with co-PI Mike Brudzinski and his students Devin Boyarko and Stefany Sit.

Data from this study came from the Earthscope US-Array/Transportable Array, the Canadian National Seismic Network through the AutoDRM system, the Berkeley Digital Seismic Network, and the Southern California Earthquake Center.

This work has been made possible with the resources available through the PASSCAL instrument center at New Mexico Tech.

9.5 References

Audet, P., Bostock, M. G., Christensen, N. I., and Peacock, S. M., Seismic evidence for overpressured subducted oceanic crust and megathrust fault sealing. *Nature*, 457, 76-78, 2009

Benson, G.D., Ritzwoller, M.H., Barmin, M.P., Levshin, A.L., Lin, F., Moschetti, M. P., Shapiro, N.M., Yang, Y., Processing seismic ambient noise data to obtain reliable broadband surface wave dispersion measurements. *Geophysical Journal International*, 169, 1239-1260, 2007

Bostock, M.G., Hyndman, R.S., Rondenay, S., and Peacock, S. M., An inverted continental Moho and serpentinization of the forearc mantle. *Nature*, 417, 53-539, 2002

Brudzinski, M. and Allen, R. M., Segmentation in Episodic Tremor and Slip All Along Cascadia. *Geology*, 35(10) 907-910, 2007

Dreger, D. S. and Romanowicz, B., Source characteristics of events in the San Francisco Bay region, *U. S. Geol. Surv. Open-File Report 94-176*, 301-309, 1994

Dziewonski and Anderson, Preliminary Reference Earth Model, *Phys. Earth. Planet. Int.*, 25, 297-356, 1981

Levander, A., Niu, F., Miller, M.S., Zhai, Y. and Liu, K., USArray Receiver Function Images of the Lithosphere in the Western U.S.. *EOS Trans. AGU 82(52)*, Fall Meet. Suppl., Abstract S44B-01, 2007

Obrebski, M. J., and Allen, R. M., Plume Vs. Plate: Convection beneath the Pacific Northwest. *Berkeley Seismological Laboratory Annual Report*, 2008-2009

Schmidt, M. E., Grunder, A.L., and Rowe, M., Segmentation of the Cascades Arc as indicated by Sr and Nd isotopic variation among primitive basalts. *Earth and Planetary Science Letters*, 266 166-181, 2007

Shapiro, N. M., and Ritzwoller, M. H., Monte-Carlo inversion for a global shear velocity model of the crust and upper mantle, *Geophysical Journal International*, 151, 88-105, 2002

Trehu, A. M., Asudeh, I., Brocher, T. M., Luetgert, J. H., Mooney, W. D., Nabelek, J. L., and Nakamura, Y., Crustal Architecture of the Cascadia Forearc. *Science*, 266, 237-243, 1994

Xue, M., and Allen, R. M., The Fate of the Juan de Fuca Plate: Implications for a Yellowstone Plume Head. *Earth and Planetary Science Letters*, 264, 266-276, 2007

10 Anisotropic Layering of the North American Craton

Huaiyu Yuan and Barbara Romanowicz

10.1 Summary

Seismic anisotropy in the Earth’s upper mantle is generally attributed to lattice-preferred orientation of anisotropic crystals in minerals such as olivine and pyroxene (e.g. *Nicolas and Christensen, 1987*) resulting from rock deformation in past and present mantle flow. Under continents, seismic anisotropy results from a combination of frozen-in lithospheric anisotropy from past deformation processes, shear coupling between the lithosphere and asthenosphere, and current flow in the asthenosphere (*Park and Levin, 2002*). Characterizing seismic anisotropy and relating it to past and present geodynamic processes thus provides insights into our understanding of the driving mechanisms of plate tectonics and lithospheric evolution.

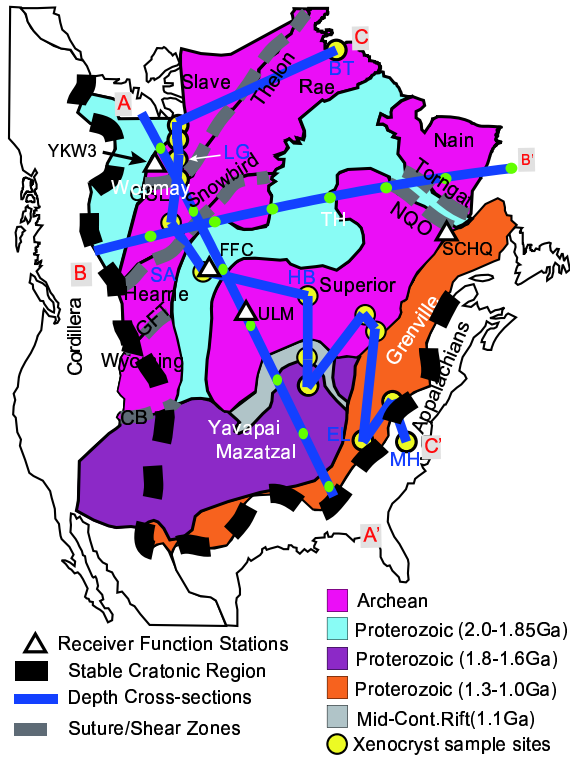


Figure 2.19: Precambrian basement of the North American continent. Precambrian province ages follow *Whitmeyer and Karlstrom (2007)*. Labels are: BHT, the Buffalo Head Terrane; THO, Trans-Hudson Orogen; MH, Medicine Hat province; WY, Wyoming Province; CP, Colorado Plateau. Depth cross-section locations are shown as thick black lines with white circles for better correspondence with Figure 2.

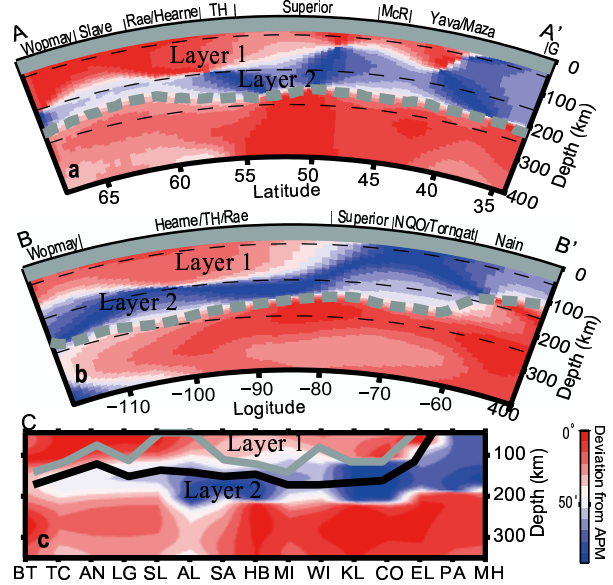


Figure 2.20: Upper mantle layering defined by changes in the direction of azimuthal anisotropy fast axis across three profiles in Figure 2.19: (a) AA’, (b) BB’ and (c) CC’. The fast axis direction is color coded as a deviation from the NA APM. Thick dashed line is our inferred LAB. Layer 1 and 2 are two lithospheric layers defined by the change of anisotropic fast axis directions. (a) Symbols are: TH, Trans-Hudson Orogen; Yava/Mazat/G: Yavapai, Mazatzal and Grenville provinces; and McR: Mid Continent Rift. (b) NQO: New Quebec Orogen. (c) This profile follows the sites where xenocryst samples have been obtained (yellow circles in Figure 2.19; *Griffin et al., [2004]*). Sample sites are labeled at the bottom of (c). The boundary corresponding to Mg#93 is indicated by a grey line, and the black line corresponds to Mg#92.

The North American (NA) continent is in many ways an ideal target for this type of study due to its rich tectonic history (Figure 2.19; e.g. *Hoffman, 1989; Thomas, 2006; Whitmeyer and Karlstrom, 2007*). In this report, we show strong anisotropic layering in the stable North American craton upper mantle, inferred from our updated 3-D upper mantle SVEMum_NA2 model (*Yuan et al., 2010*). This layering of anisotropy in the craton enables us to distinguish three domains of azimuthal anisotropy, two in the lithosphere and one in the asthenosphere (*Yuan and Romanowicz, 2010*). In particular, the boundary between the two lithospheric layers roughly corresponds to the negative velocity jump detected in receiver function studies (*Yuan et al., 2010*).

10.2 Anisotropic Layering

In Figure 2.20, we present upper mantle layering defined by changes in the direction of azimuthal anisotropy fast axis, shown as depth cross sections across three profiles. We found that beneath the craton, the fast axis direction of anisotropy becomes systematically aligned with the absolute plate motion (APM; *Gripp and Gordon, 2002*) below the lithosphere-asthenosphere boundary (LAB), confirming our previous findings (*Marone and Romanowicz, 2007*). The changes with depth of azimuthal anisotropy define more accurately (to within ± 20 km) the location of the LAB than depth profiles of isotropic shear velocity (V_s) or radial anisotropy ($\xi = (V_{sh}/V_{sv})^2$), which, in general, shows gradual decrease in amplitude across the LAB depth, and thus does not allow us to locate the LAB (*Yuan and Romanowicz, 2010; Yuan et al., 2010*).

Moreover, a change in direction of the fast axis of azimuthal anisotropy at mid-lithospheric depths clearly defines two layers (Layer 1 and 2; Figure 2.20) within the cratonic lithosphere, separated by a boundary with large lateral variations in depth. Layer 1 is thick under the central part of the craton and tapers off at its boundaries with Paleozoic provinces (e.g. Figure 2.19). The thickest parts of Layer 1 are found in regions affected by orogenies in the Archean (e.g. the Trans-Hudson orogen). Layer 1 also thins in the Mid-continental rift zone (Figure 2.20a). The lateral variations in the thickness of Layer 1 are in good agreement with geochemical estimates from xenolith studies for the most depleted part of the craton, as defined in terms of Mg # (Figure 2.20c; *Griffin et al., 2004*).

10.3 Tectonic Implications

Comparison with the geochemistry studies (Figure 2.20c) suggests that Layer 2 may represent a younger, less depleted, thermal boundary layer, possibly accreted at a later stage through processes influenced by the presence of a stagnant, chemically distinct lid (Layer 1). This scenario is supported by the excellent agreement between the lateral variations in the depth of the LAB inferred from our azimuthal anisotropy study and the variations predicted from the thickness of Layer 1 (Figure 4 in *Yuan and Romanowicz, 2010*), when applying the geodynamically inferred relationship between the thicknesses of the chemical and thermal lithospheres (e.g. *Cooper et al., 2004*).

We suggest that receiver functions and long range seismic profiles preferentially detect the transition between the ancient Archean lithosphere (Layer 1) and the subsequently accreted thermal boundary layer (Layer 2). The details of this transition and its precise nature are likely to be complex, as indicated by the fine layering documented by long range seismic profile studies (*Thybo, 2006*), and may involve stacks of thin, low-velocity lay-

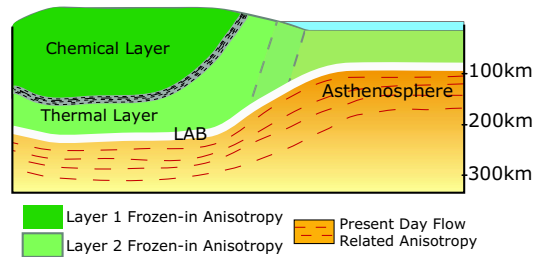


Figure 2.21: Cartoon illustrating the inferred stratification of the lithosphere. Beneath the craton, three layers of anisotropy are present: two in the lithosphere (Layers 1 and 2), and one in the asthenosphere. Layer 1 corresponds to the chemically distinct, depleted Archean lithosphere, and Layer 2 is the thermal root, separated from the asthenosphere by the LAB, which is at relatively constant depth beneath the stable part of the continent, but rapidly shallows between the tectonic part of the continent and the oceans. The boundary between layers 1 and 2 is seismically sharp, but its fine-scale structure is likely to be complex.

ers marking the trace of partial melting and dehydration (*Mierdel et al., 2007*), possibly at the top of oceanic lithosphere that was welded onto the bottom of Layer 1. It could also result from kimberlite accumulation (*Sleep, 2009*) if the strong, chemically distinct, Archean Layer 1 acts as a barrier to their further ascent. Note that this mid-lithospheric anisotropic boundary zone must be a sharp high-to-low velocity horizon since it produces converted phases seen in receiver function studies, but it is barely detectable by isotropic velocity tomography, although we have noted the presence of a local minimum in the depth profile of shear velocity in some parts of our model. On the other hand, the LAB under cratons is likely more gradational, as it is hard to detect with receiver functions, which is consistent with a largely thermal, anisotropic boundary that likely does not involve any significant compositional changes or partial melting.

Here, by using an approach based on seismic azimuthal anisotropy, we have documented the craton-wide presence of a mid-lithospheric boundary, separating a highly depleted chemical layer of laterally varying thickness, from a less depleted deeper layer bounded below by a relatively flat LAB (Figure 2.21). The change of fast-axis direction of azimuthal anisotropy with depth is a powerful tool for the detection of lithospheric layering under continents. Our study indicates that the “tectosphere” is no thicker than 200-240 km and that its chemically depleted part may bottom out around 160-170 km.

10.4 References

References are found in the References section of our paper: Yuan, H. and Romanowicz, B., Lithospheric layering in the North American Craton, *Nature*, 466, 1063-1068, 2010.

11 3-D Shear Wave Radially and Azimuthally Anisotropic Velocity Model of the North American Upper Mantle

Huaiyu Yuan, Barbara Romanowicz, Karen Fischer (Department of Geological Sciences, Brown University, Providence, Rhode Island, USA), and David Abt (ExxonMobil Exploration Company, Houston, Texas, USA)

11.1 Summary

Using a combination of long period seismic waveforms and SKS splitting measurements, we have developed a 3D upper mantle model (SAWum_NA2; *Yuan et al.* 2010) of North America that includes isotropic shear velocity (Figure 2.22), with a lateral resolution of ~ 200 km, as well as radial and azimuthal anisotropy (Figures 2.23, 2.24, respectively), with a lateral resolution of ~ 400 km. Combining these results, we infer several key features of the lithosphere and asthenosphere structure.

A rapid change from thin (~ 70 - 80 km) lithosphere in the western US to thick lithosphere (~ 200 km) in the central, cratonic part of the continent closely follows the Rocky Mountain Front (RMF; thick dashed line in Figure 2.22). Changes with depth of the fast axis direction of azimuthal anisotropy reveal the presence of two layers in the cratonic lithosphere, as shown in our companion paper (*Yuan and Romanowicz, 2010a*), and allow us to define the lithosphere-asthenosphere boundary (LAB) throughout the craton more precisely than from isotropic velocity tomography or the analysis of receiver function data, which, on the other hand, define the LAB consistently in the western US, where the boundary is sharper. The boundary between the two lithospheric layers in the craton varies significantly in depth and may correspond to the mid-lithospheric fast-to-slow discontinuity found in receiver function studies. Lateral variations in azimuthal and radial anisotropy in the cratonic lithosphere correspond to surface geological features marking tectonic events of the past.

Below the lithosphere, azimuthal anisotropy (Figure 2.23) manifests a maximum, stronger in the western US than under the craton, and the fast axis of anisotropy aligns with the absolute plate motion. In the western US, this zone is confined to between 70 and 150 km, decreasing in strength with depth from the top, from the RMF to the San Andreas Fault system and the Juan de Fuca/Gorda ridges. This result suggests that shear associated with lithosphere-asthenosphere coupling dominates mantle deformation down to this depth in the western part of the continent. The depth extent of the zone of increased azimuthal anisotropy below the cratonic lithosphere is not well resolved in our study, although it is peaked around 270 km, a robust result.

Radial anisotropy (Figure 2.24) is such that, predominantly, $\xi > 1$, where $\xi = (V_{sh}/V_{sv})^2$, under the continent and its borders down to ~ 200 km, with stronger ξ in the bordering oceanic regions. Across the continent and be-

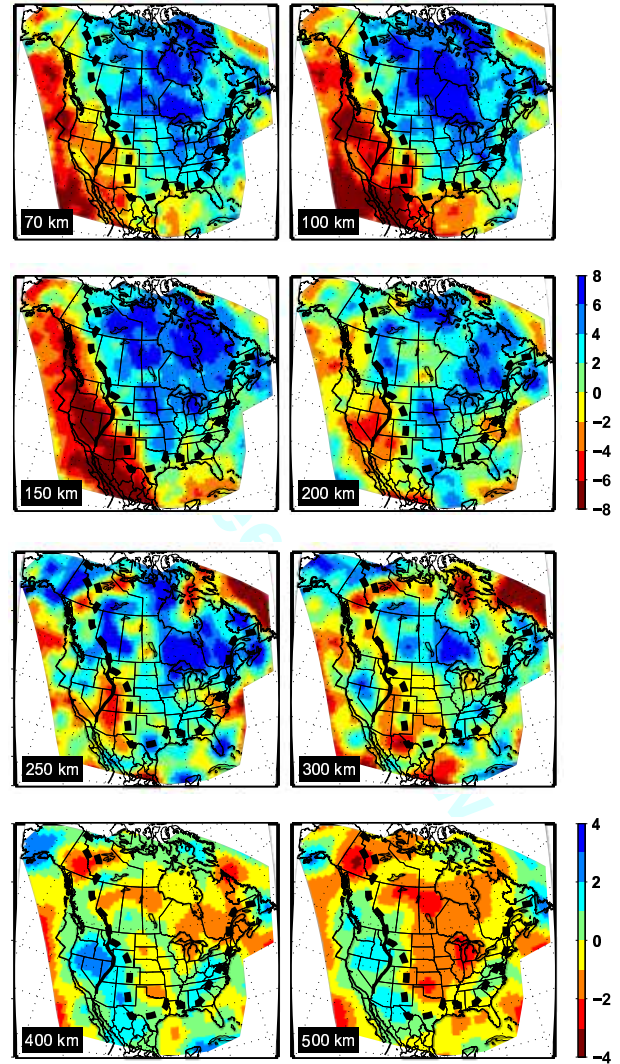


Figure 2.22: Isotropic velocity (V_s) perturbations, plotted with respect to the North America regional average shown (Figure 3 in *Yuan and Romanowicz, 2010*). Black dashed line approximately delineates the continent cratonic region, which approximately follows the Rocky Mountain front to the west, and the Ouachita and Appalachian fronts to the south and east. Velocity variations are saturated at -8% to 8% scale at ≤ 200 km depth, and -4% to 4% below 200 km. The Paleozoic continent rift margin in the western US, which spatially correlates with the Sevier thrust and fold belt in the western US, is shown as a black line for reference.

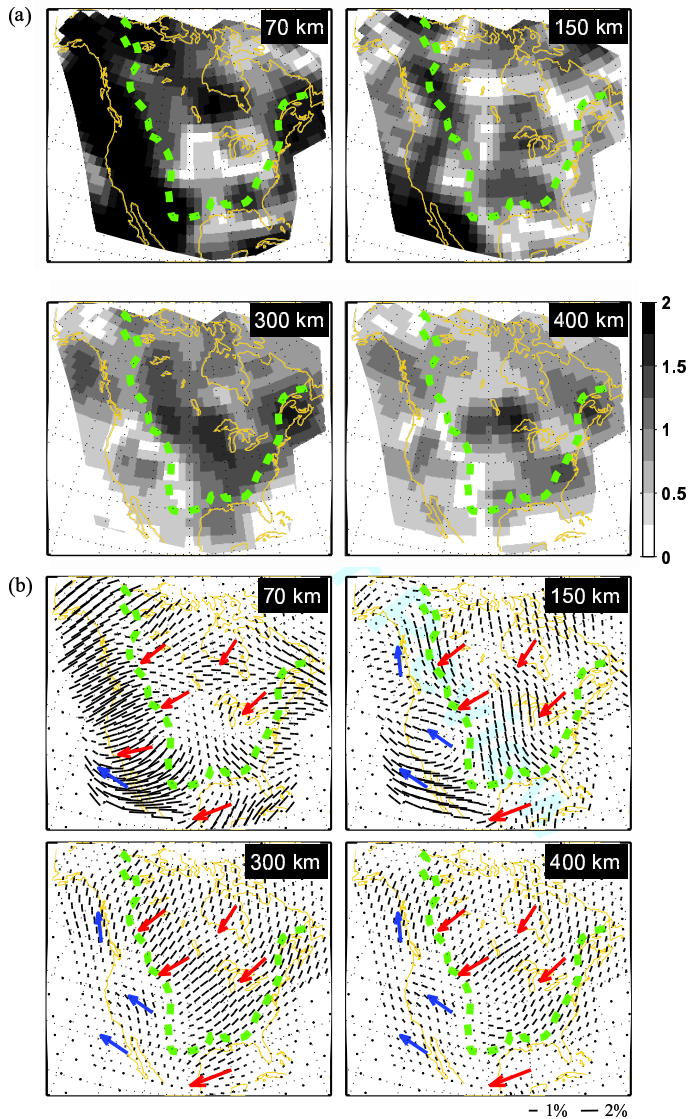


Figure 2.23: (a) Azimuthal anisotropy strength G . (b) Depth dependent fast axis direction. Red arrows show the absolute plate motion (APM) direction of the North American Plate, and blue arrows are those for the Pacific plate APM (Gripp and Gordon, 2002). Green dashed line approximately delineates the continent cratonic region as in Figure 2.22.

low 200 km, alternating zones of weaker and stronger radial anisotropy, with predominantly $\xi < 1$, correlate with zones of small lateral changes in the fast axis direction of anisotropy, and faster than average V_s below the LAB, suggesting the presence of small scale convection with a wavelength of ~ 2000 km.

11.2 References

Yuan, H. and Romanowicz, B., Lithospheric layering in the North American Craton, *Nature*, 466, 1063-1068, 2010a.

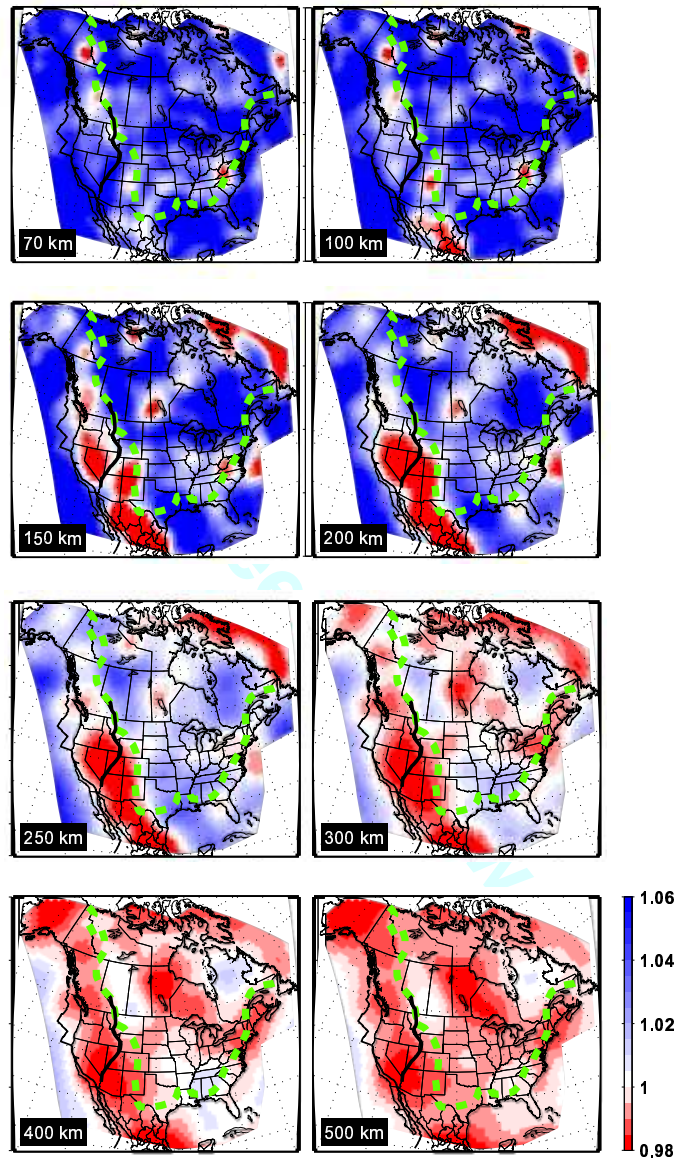


Figure 2.24: Radial anisotropy parameter ξ , plotted with respect to isotropy. Green dashed line approximately delineates the continent cratonic region, as in Figure 2.22. The Sevier thrust and fold belt in the western US is shown as a black line for reference.

Yuan, H. and Romanowicz, B., Depth Dependent Azimuthal anisotropy in the western US upper mantle, *Earth Planet. Sci. Lett.*, doi:10.1016/j.epsl.2010.10.020, 2010b.

Yuan, H., Romanowicz, B., Fisher, K. and Abt, D., 3-D shear wave radially and azimuthally anisotropic velocity model of the North American upper mantle, *Geophys. J. Int.*, accepted, 2010.

12 Depth Dependent Azimuthal Anisotropy in the Western US Upper Mantle

Huaiyu Yuan and Barbara Romanowicz

12.1 Summary

We present the results of a joint inversion of long period seismic waveforms and SKS splitting measurements for 3D lateral variations of anisotropy in the upper mantle beneath the western US, incorporating recent datasets generated by the USArray deployment as well as other temporary stations in the region (Yuan and Romanowicz, 2010). We find that shallow azimuthal anisotropy closely reflects plate motion generated shear in the asthenosphere in the shallow upper mantle (70-150 km depth), whereas at depths greater than 150 km, it is dominated by northward and upward flow associated with the extension of the East-Pacific Rise under the continent, constrained to the east by the western edge of the North-American craton, and to the north by the presence of the east-west trending subduction zone. In particular, the depth integrated effects of this anisotropy explain the apparent circular pattern of SKS splitting measurements observed in Nevada without the need to invoke any local anomalous structures.

12.2 Circular pattern of the SKS splitting: Depth Integrated Effects

The recent deployment of the Transportable Array (TA) of EarthScope, as well as several other temporary broadband networks in the western US, have provided the opportunity to measure SKS splitting at a significantly larger number of locations in the region than was previously possible. Combined with previously available SKS splitting data, these measurements have revealed an intriguing apparent “circular” pattern in the distribution of fast axis directions and amplitude of anisotropy, centered in south-central Nevada, with vanishing strength in the center of the pattern (Savage and Sheehan, 2000; Liu, 2009; West et al., 2009). Interestingly, some recent regional body wave tomographic studies also show the presence of a fast velocity anomaly extending into the transition zone, beneath the Cascades and High Lava Plains (e.g. van der Lee and Nolet, 1997; Xue and Allen, 2007; Sigloch et al., 2008; Burdick et al., 2009). Various geodynamic models have been proposed to address the mantle flow associated with these features, including: 1) initial impinging of the Yellowstone Plume into the lithosphere in the Basin and Range province (Savage and Sheehan, 2000; Walker et al., 2004); 2) toroidal flow around the southern edge of the sinking Gorda-Juan de Fuca plate, associated with its retreating and the creation of a slab (Zandt and Humphreys, 2008); and 3) astheno-

spheric flow associated with a sinking lithospheric instability (or “drip”) in the center of the Basin and Range (West et al., 2009).

Our 3-D azimuthal anisotropy model (Figure 2.25; Yuan and Romanowicz, 2010) shows a strongly depth dependent azimuthal anisotropy pattern in the western US, with orientation of the fast axis controlled by plate motion related lithosphere-asthenosphere coupling at depths shallower than 150 km, and other processes at greater depths, likely representing the channeling of deep flow from the East Pacific Rise constrained by the presence of the craton margin to the west and subducted slabs to the north. We infer that all of these features combined significantly contribute to the circular pattern and large splitting times of the SKS splitting observations. The strong lateral and vertical variations throughout the western US revealed by our azimuthal anisotropy model reflect complex past and present tectonic processes. In particular, the depth integrated effects of this anisotropy (Figure 2.26) explain the apparent circular pattern of SKS splitting measurements observed in Nevada without the need to invoke any local anomalous structures (e.g. ascending plumes or sinking lithospheric instabilities; Savage and Sheehan, 2000; West et al., 2009): the circular pattern results from the depth-integrated effects of the lithosphere-asthenosphere coupling to the North American, Pacific and Juan de Fuca plates at shallow depths, and in the depth range 200-400 km, northward flow from the East Pacific Rise channeled along the craton edge and deflected by the Juan de Fuca slab, and, more generally, slab-related anisotropy.

12.3 References

- Burdick, S., van der Hilst, R.D., Vernon, F.L., Martynov, V., Cox, T., Eakins, J., Mulder, T., Astiz, L. and Pavlis, G.L., Model Update December 2008: Upper Mantle Heterogeneity beneath North America from P-wave Travel Time Tomography with Global and USArray Transportable Array Data, *Seismol. Res. Lett.*, 80, 638-645, 2009.
- Gripp, A.E. and Gordon, R.G., Young tracks of hotspots and current plate velocities, *Geophys. J. Int.*, 150, 321-361, 2002.
- Liu, K.H., NA-SWS-1.1: A uniform database of teleseismic shear wave splitting measurements for North America, *Geochem. Geophys. Geosyst.*, 10, Q05011, doi:10.1029/2009GC002440, 2009.
- Savage, M.K. and Sheehan, A.F., Seismic anisotropy and mantle flow from the Great Basin to the Great Plains, western United States, *J. Geophys. Res.*, 105(13), 715-713, 734, 2000.
- Sigloch, K., McQuarrie, N. and Nolet, G., Two-stage subduction history under North America inferred from multiple-

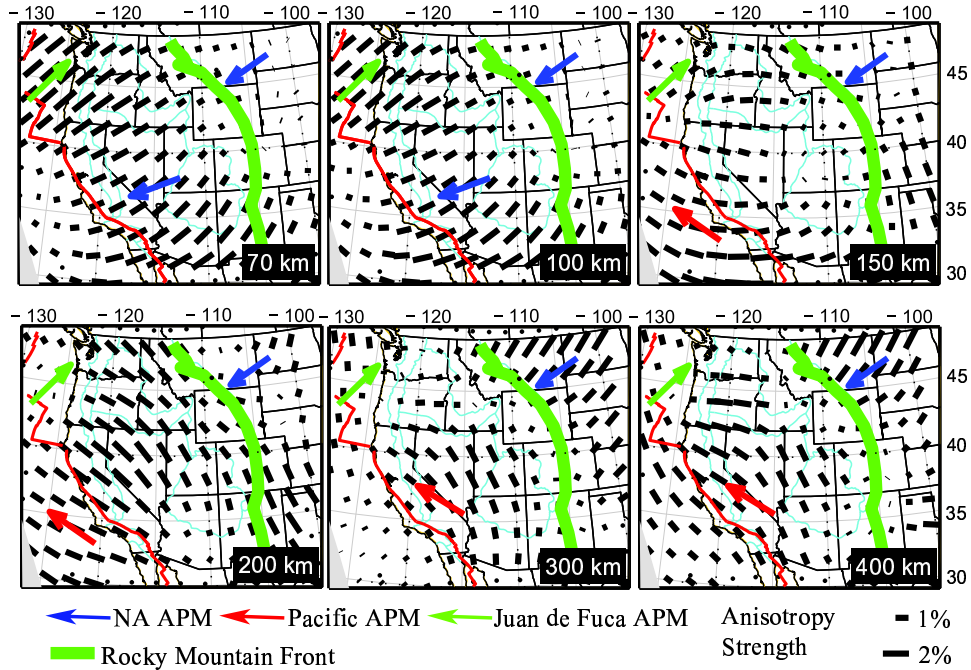


Figure 2.25: Azimuthal anisotropy variations with depth. Black bars indicate the fast axis direction and the bar length is proportional to the anisotropy strength. Blue, green and red arrows show the absolute plate motion (APM) directions of the North American, Juan de Fuca, and Pacific plates respectively, computed at each location using the HS3-NUVEL 1A model (*Gripp and Gordon, 2002*).

frequency tomography, *Nature Geosci.*, 1, 458-462, 2008.

van der Lee, S. and Nolet, G., Upper mantle S velocity structure of North America, *J. Geophys. Res.*, 102, 22815-22838, 1997.

Walker, K.T., Bokelmann, G.H.R. and Klemperer, S.L., Shear-wave splitting beneath the Snake River Plain suggests a mantle upwelling beneath eastern Nevada, USA, *Earth Planet. Sci. Lett.*, 222, 529-542, 2004.

West, J.D., Fouch, M.J., Roth, J.B. and Elkins-Tanton, L.T., Vertical mantle flow associated with a lithospheric drip beneath the Great Basin, *Nature Geosci.*, 2, 439-444, 2009.

Xue, M. and Allen, R.M., The fate of the Juan de Fuca plate: Implications for a Yellowstone plume head, *Earth Planet. Sci. Lett.*, 264, 266-276, 2007.

Yuan, H. and Romanowicz, B., Depth Dependent Azimuthal anisotropy in the western US upper mantle, *Earth Planet. Sci. Lett.*, doi:10.1016/j.epsl.2010.10.020, 2010.

Zandt, G. and Humphreys, E., Toroidal mantle flow through the western US slab window, *Geology*, 36, 295-298, 2008.

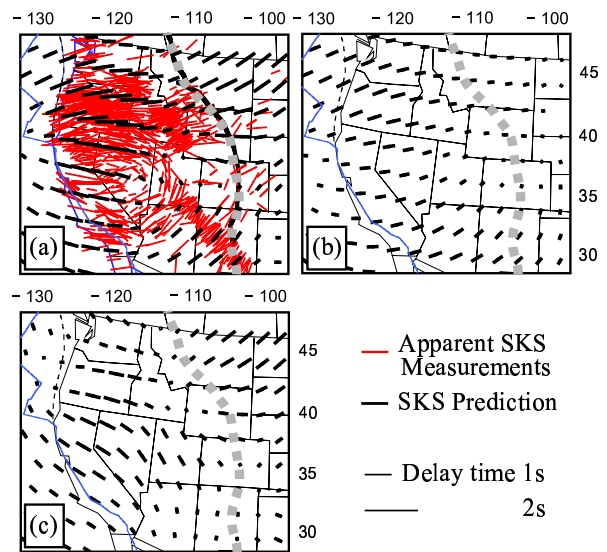


Figure 2.26: Comparison of observed and predicted station averaged SKS splitting direction and time. Red bars indicate observations and are shown in the left panels only, for clarity. Black bars indicate the model predictions. Predicted splitting is shown for integration of the models over, (a) the full depth range of the azimuthal anisotropy models, (b) the top 150 km of the models, and (c) the portion of the model between 150 and 500 km, respectively.

13 Seismic Signature of Perovskite and Postperovskite in the D''

Sanne Cottaar, Allen McNamara, Barbara Romanowicz and Rudy Wenk

13.1 Introduction

The D'' zone at the base of the mantle is a boundary layer, both chemically and thermally. Complex dynamic processes are the cause of lateral heterogeneities, with sharp boundaries at the edge of superplumes (e.g. *Toh et al.*, 2005). Another characteristic of D'' is the presence of strong and laterally varying anisotropy. A global long-wavelength model for S-wave velocity and radial anisotropy shows that, in general, SH phases are faster than SV phases (*Panning and Romanowicz*, 2006). This transverse isotropy is strongest in a ring around the Pacific, a.k.a. "the slab graveyard," and confirmed by a large number of regional studies. These observations lead to the idea that flow causes anisotropy by alignment of anisotropic minerals. This study combines geodynamics and mineral physics to investigate seismic heterogeneities and anisotropy in the D''. Different seismic velocity models are created to constrain possible microscopic and macroscopic processes.

13.2 Method

The two-dimensional isochemical convection model is refined to emphasize deformation in D'' (*McNamara and Zhong*, 2004). Lagrangian tracers travel through the lowermost part of the model providing strain information. Deformation is strong in the lowermost mantle, and if dislocation creep occurs, preferred orientation of minerals can cause seismic anisotropy. The exact resulting anisotropy depends on dominant deformation mechanisms and single crystal elastic constants. Using results from different experimental studies, we calculate the texturing of assemblages of perovskite and post-perovskite with periclase using VPSC (*Lebensohn and Tomé*, 1993). Averaging the single crystal elastic constants (*Stackhouse et al.*, 2005, *Wentzcovitch et al.*, 2007) over the orientation of the textured grains results in the prediction of a 2D, fully anisotropic model. Here we present a least squares fit of isotropic and transverse isotropic models to the fully anisotropic models.

13.3 Isotropic velocities

Results for the isotropic velocity models are presented in Figure 2.27A for 75% perovskite or 75% post-perovskite with 25% periclase. Variations are mainly due to variations in pressure and temperature and are stronger than in typical inverted models. The temperature sensitivity of the shear modulus causes strong lateral S-wave velocity variations, while the bulk modulus, and

thus the bulk sound velocity, have more sensitivity to vertical pressure variations. S-wave velocity variations are predicted to be stronger for post-perovskite than for perovskite. The occurrence of post-perovskite can thus explain the increase in $d \ln V_s$ in the lowermost mantle in inverted models.

13.4 Transverse isotropic signature

Transversally isotropic models are shown in Figure 2.27B, in which the case for post-perovskite is expanded for three different dominant slip planes. Although all slip planes are activated during dislocation creep, different mineral physics experiments have concluded that different slip planes are dominant (*Merkel et al.*, 2007, *Miyagi et al.*, 2009, 2010). As the figures show, the different assemblages and deformation regimes result in different anisotropic signatures. The post-perovskite assemblage for dominant slip planes of [010] and [001] corresponds with these observations, while the perovskite assemblage has an opposite signature.

The results for dominant slip planes of [010] and [001] have opposite signatures for P-wave anisotropy. *Beghein et al.* (2006) find a likely anti-correlation between P and S wave anisotropy using normal modes, similar to the [001] case here. A number of local studies find anti-correlation between P and S wave velocities (*Wyssession et al.*, 1999, *Tkalcic and Romanowicz*, 2002), as well as global studies, which find an anti-correlation between shear wave and bulk sound velocities (*Su and Dziewon-ski*, 1997). Possibly these measurements reveal the anti-correlation between SH and PH (or horizontal bulk sound velocity) caused by anisotropy, as isotropic variations (Figure 2.27A) cannot explain them.

The plumes on the right in the figures are more difficult to interpret as we use a 2D model for these 3D features, and it is more implausible for dislocation creep to occur at these higher temperatures.

13.5 Discussion and Conclusions

From a mineral physics point of view, the occurrence of the perovskite to post-perovskite transition a couple hundred kilometers above the D'' is the subject of strong debate. *Shim et al.* (2009) show that adding Al and Fe causes the phase transition to broaden and shift to higher pressures.

From a seismological point of view, postperovskite can explain observations of strong S-wave heterogeneities, SH faster than SV in subduction regions, and anti-correlation between S and P wave anisotropy. Additionally, seismic

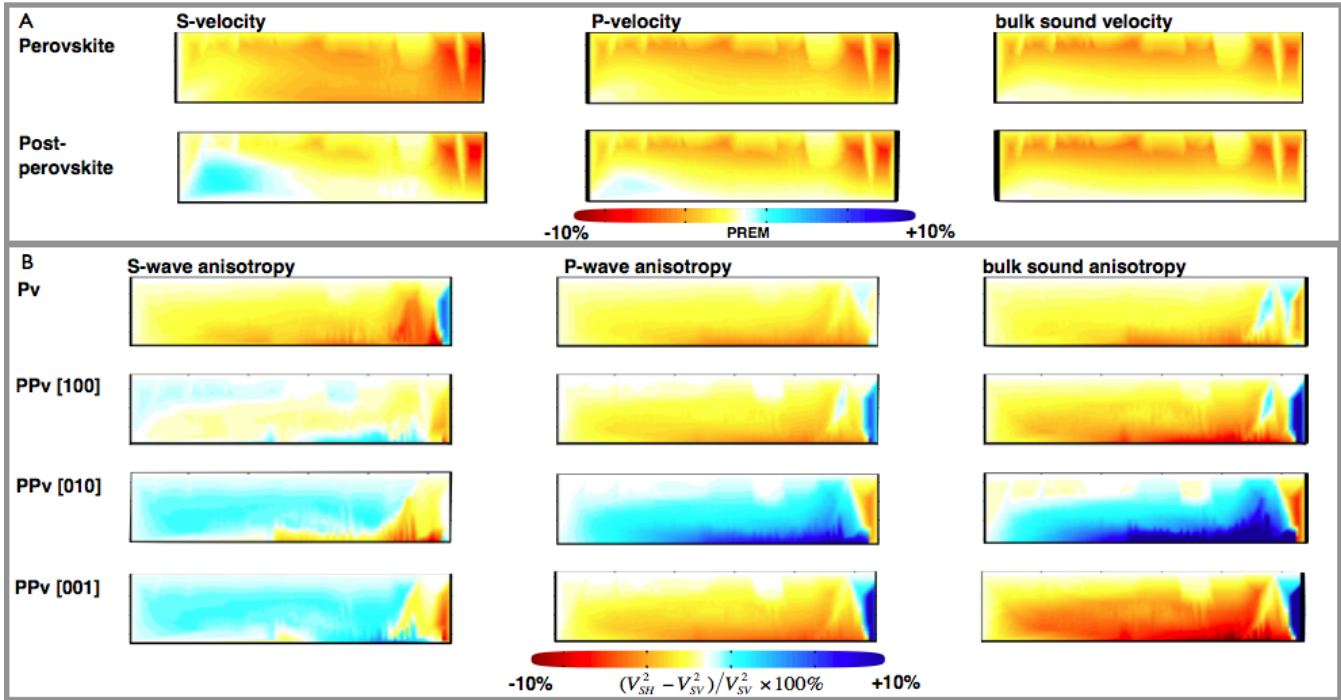


Figure 2.27: Best fitting isotropic and transversely isotropic models for the D". Figures are strongly vertically exaggerated: dimensions are ~ 72 degrees horizontally to 300 km vertically above the core-mantle boundary (CMB). Slab subduction takes place on the left, and upwelling on the right. A. Isotropic velocities for perovskite and postperovskite plotted relative to PREM. B. Transversely isotropic models in which blue is SH faster than SV and red the opposite.

observations can constrain postperovskite to have a dominant slip plane along [001] as measured by Miyagi *et al.* (2010).

13.6 Acknowledgements

This project is funded by NSF's CSEDI program under grant number NSF EAR-0757608.

13.7 References

Beghein C., J. Trampert and H.J. van Heijst, Radial anisotropy in seismic reference models of the mantle, *J. Geophys. Res.* **111**, B02303, 2006.

Lebensohn R.A., and C.N. Tomé, A self-consistent anisotropic approach for the simulation of plastic deformation and texture development of polycrystals, *Acta Metall. Mater.* **41**, 2611-2624, 1993.

McNamara, A.K. and S. Zhong, The influence of thermochemical convection on the fixity of mantle plumes, *EPSL*, **222**, 485-500, 2004.

Merkel S, A.K. McNamara, A. Kubo, S. Speziale, L. Miyagi, Y. Meng, T. S. Duffy, H.-R. Wenk, Deformation of (Mg,Fe)SiO₃ post-perovskite and D anisotropy, *Science*, **316**, 1729-1732, 2007.

Miyagi L., S. Merkel, T. Yagi, N. Sata, Y. Ohishi, H.-R. Wenk, Diamond anvil cell deformation of CaSiO₃ perovskite up to 49 GPa. *Phys. Earth Planet. Int.*, **174**, 159-164, 2009.

Miyagi L. *et al.*, *in prep.*, 2010.

Panning, M. and B. Romanowicz, A three dimensional radially anisotropic model of shear velocity in the whole mantle, *Geophys. J. Int.*, **167**, 361-379, 2006.

Shim, S., K. Catalli, and V. Prakapenka, Seismic detectability of the postperovskite boundary, *AGU fall meeting*, abstract #DI21B-01, 2009.

Stackhouse, S., J.P. Brodholt, J. Wookey, J.-M. Kendall and G.D. Price, The effect of temperature on the seismic anisotropy of the perovskite and post-perovskite polymorphs of MgSiO₃, *EPSL*, **230**, 1-10, 2005.

Su W., and A.M. Dziwonski, Simultaneous inversion for 3-D variations in shear and bulk velocity in the mantle, *Phys. Earth Planet. Int.*, **100**, 135-156, 1997.

Thalchic H. and B. Romanowicz, Short Scale heterogeneity in the lowermost mantle: insights from PcP-P and ScS-S data, *EPSL*, **201**, 57-68, 2002.

Toh, A., B. Romanowicz, Y. Capdeville and N. Takeuchi, 3D effects of sharp boundaries at the borders of the African and Pacific Superplumes: observation and modeling, *Earth and Planet. Sci. Lett.*, **233**, 137-153, 2005.

Wentzovitch R.M., T. Tsuchiya, J. Tsuchiya, MgSiO₃ post-perovskite at D" conditions. *PNAS*, **103**, 543-546, 2006.

Wyssession, M.E., A. Langenhorst, M.J. Fouch, K.M. Fischer, G. I. Al-Eqabi, P.J. Shore, and T.J. Clarke, Lateral variations in compressional/ shear velocities at the base of the mantle, *Science*, **284**, 120-125, 1999.

14 Using the SEM to Simulate Random Wavefields and Improve Noise Tomography

Paul Cupillard, Laurent Stehly and Barbara Romanowicz

14.1 Introduction

The correlation of a random wavefield recorded by distant receivers contains the Green's function (GF) of the medium. This makes the measurement of seismic wave travel times between any pair of receivers a possibility. These measurements can then be inverted to image the Earth's interior (e.g. *Shapiro et al, 2005*).

This result is valid in any medium but relies on a strong assumption: The wavefield has to be equipartitioned, that is, all the modes of the medium have to be excited with the same level of energy and a random phase (*Sánchez-Sesma and Campillo, 2006*). Equipartition is achieved, for instance, if there are white noise sources everywhere in the medium or if few sources are present in a highly scattering medium.

The seismic ambient noise comes from interactions between the atmosphere, the ocean and the sea floor. Even averaged over one year, the distribution of noise sources at the surface of the Earth is not homogeneous and does not completely match the requirements of the theories that relate noise correlations to the GF of the medium.

The uneven distribution of noise sources, the fact that one uses a finite amount of data to compute noise correlations, and the way noise correlations are inverted imply several limitations on ambient noise tomography. (i) In most of the noise tomographic studies, less than one interstation path out of three is used. Other paths are rejected because either surface waves cannot be identified unambiguously, or the surface wave travel times measured on the positive and negative side of the correlation are not consistent. This is mostly due to the uneven distribution of noise sources. (ii) The velocity of surface waves can be systematically over- or underestimated for certain azimuths, since noise sources are not evenly distributed. This could be erroneously interpreted as anisotropy of the medium. (iii) Most of the time, surface wave dispersion curves are inverted using the Path Average approximation. This procedure does not account for the complexity of the wave propagation within the Earth. When using noise correlations, this is an important problem because noise correlations are very sensitive to the crust, which is a very heterogeneous structure.

14.2 Simulating seismic ambient noise using the Spectral Element Method

In this work, we explore the possibility of taking into account the distribution of noise sources when inverting

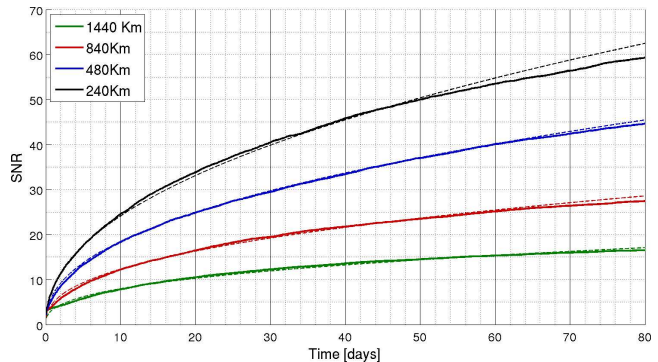


Figure 2.28: SNR of noise correlation surface waves as a function of the number of days of correlated noise (plain lines). Four interstation distances are considered. Each SNR curve is compared to the semi-empirical expression from *Larose et al (2008)* (dashed lines).

noise correlations. A first step towards such a goal is to perform a forward modeling which includes noise sources. To do so, we use the Spectral Element method (SEM). Computing synthetic correlations by simulating a random wavefield using the SEM would eliminate most of the biases arising from the uneven distribution of noise sources during the forward problem. We use the SEM instead of other methods such as the normal mode summation technique (*Cupillard and Capdeville, 2010*) because it enables us to solve the wave equation with no restriction on the velocity contrast of the model.

The code we use enables us to impose a three-component random traction on the top surface of the region. Because it makes the implementation very easy, the traction is discretized over the grid points of the spectral element mesh. For each grid point, three random signals are generated: one to define the normal traction and two to define the tangential traction. In the present work, we only use the normal component (the two tangential components are set to zero). All the random signals are filtered in the 25 - 80 s period band and are then used in the SEM simulation as an external surface force.

We start by investigating the easiest case: an homogeneous distribution of noise sources at the free surface of an attenuating and spherically symmetric Earth. Our simulation consists of 37 numerical runs computed in PREM and lasting 4000 s each. We consider a 75x35 degree wide region surrounded by absorbing boundaries and a bottom lying at 600 km. An array of 40x5 receivers separated by 60 km records the vertical displacement. The

GF is retrieved between each station pair by correlating the background seismic noise records. No processing is performed on the noise records, such as frequency whitening or one-bit normalization.

Since we consider a 1D model, the GF only depends on the source-receiver distance. This implies that all correlations computed between station pairs separated by the same distance converge towards the same GF. Therefore, we consider that averaging the correlation over time T or over station pairs is equivalent. Since we perform 37 runs of 4000 s, each receiver records $37 * 4000s = 1.7$ days of noise. As we have, for instance, 140 pairs of stations separated by 720 km, summing the corresponding correlations provides a result similar to correlating $37 * 140 * 4000 s = 237$ days of noise.

14.3 The convergence towards the GF

For scalar waves in a 2D homogeneous medium with a uniform source distribution, the signal-to-noise ratio (SNR) of the correlations is (Larose *et al*, 2008):

$$\text{SNR}(T, r) = C \sqrt{\frac{nT \Delta f c}{r f}}, \quad (2.2)$$

where r is the interstation distance, n the number of noise sources, c the velocity of the medium, f the frequency, Δf the bandwidth and C a constant.

We compare this theoretical prediction with our observations. Figure 2.28 shows how the SNR of the correlations evaluated in the 25-60s period band evolves with the amount of data used for stations separated by 240, 480, 840, and 1440 km. For a short offset, less than two days are required to get a $\text{SNR} > 10$, and 20 days are required for stations separated by 1440 km. We fit this SNR vs time curve with a function of the form $a \left(\frac{nT \Delta f c}{r f}\right)^b$, a and b being two free parameters we want to determine. We find that our SNR measurements are best fitted with $a=27.8$ and $b=0.45$, i.e the SNR increases with $T^{0.45}$ whereas theoretically one expects $T^{0.5}$. However, this difference is only an artifact, coming from our assumption that averaging correlation over time is equivalent to averaging them over the interstation pairs.

14.4 Improving synthetic noise correlations using curvelet filters

Our numerical results show that (i) it takes only a few days to reconstruct accurately the surface wave part of the Green's function and (ii) several months of data are required for the random fluctuations of the correlation to disappear. If most of the information on the medium is already present in a correlation averaged over a few days, then it should be possible to isolate this information from the random fluctuations of the correlation. This would allow us to not only measure surface wave travel times

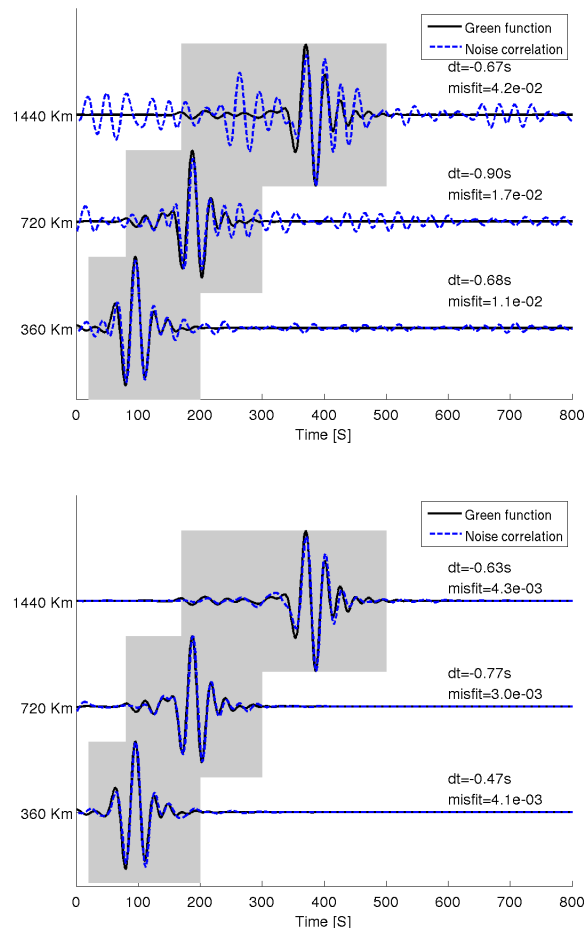


Figure 2.29: Correlations of 11 days of noise between stations separated by 320, 720 and 1440 km (dashed lines) vs corresponding GF (plain lines). For each comparison, we show the misfit of the correlation and GF waveforms measured in the shaded area and the surface wave travel time difference dt . Top: raw correlations. Bottom: correlations de-noised by curvelet filters.

more accurately, but also reconstruct the full waveform of the GF using a smaller amount of data. Figure 2.29 shows that curvelet filters achieve this goal very well.

14.5 References

- Cupillard, P. and Y. Capdeville, On the amplitude of surface waves obtained by noise correlation and the capability to recover the attenuation: a numerical approach, *Geophys. J. Int.*, 181(3), 1687-1700, 2010.
- Larose, E., P. Roux, M. Campillo and A. Derode, Fluctuations of correlations and Green's function reconstruction: role of scattering, *J. Appl. Phys.*, 103, 114907, 2008.
- Sánchez-Sesma, F. J. and M. Campillo, Retrieval of the Green's function from cross-correlation: The canonical elastic problem, *Bull. Seism. Soc. Am.*, 96, 1182-1191, 2006.
- Shapiro, N. M., M. Campillo, L. Stehly and M. H. Ritzwoller, High-resolution surface wave tomography from ambient seismic noise, *Science*, 307, 1615-1618, 2005

15 Toward the Future of Global Waveform Tomography: Scalable Gauss-Newton and Alternative Data-Partitioning Schemes

Scott French, Vedran Lekic, and Barbara Romanowicz

15.1 Introduction

With increasingly fine-scale parameterization of global tomographic models comes growth of the linear systems that underlie most iterative inversion schemes (e.g. SEMum: *Lekic and Romanowicz, 2010*). As assembly and solution of these systems becomes intractable on modern workstations, distributed-memory parallel solvers provide an attractive alternative. We summarize the development of a parallel solver tailored to the regularized Gauss-Newton scheme often used in global tomography.

In a separate effort, we explore alternative data-partitioning schemes for waveform inversion using a synthetic dataset. The SPICE tomographic benchmark was developed to evaluate the effects of inversion methodology on the resolving power of tomographic images (*Qin et al., 2008*). We discuss our use of the simpler SPICE “preliminary” waveform dataset to examine data-partitioning schemes different from those employed in Berkeley global tomographic efforts to date.

15.2 A parallel Gauss-Newton solver for waveform tomography

In waveform tomography, we seek to invert a dataset of long-period waveforms \mathbf{d} for a model of earth structure \mathbf{m} . The non-linear dependence of the wavefield upon \mathbf{m} requires structural sensitivity to be linearized and \mathbf{m} iteratively estimated. The generalized least-squares formalism is popular choice for such problems (e.g. *Tarantola, 2005*), and gives rise to the following regularized Gauss-Newton scheme:

$$(\mathbf{G}_k^T \mathbf{C}_d^{-1} \mathbf{G}_k + \epsilon^2 \mathbf{C}_m^{-1}) \delta \mathbf{m}_k = \mathbf{G}_k^T \mathbf{C}_d^{-1} \delta \mathbf{d}_k + \epsilon^2 \mathbf{C}_m^{-1} \delta \mathbf{m}_p$$

where \mathbf{m}_k and \mathbf{m}_{k+1} are current and updated model estimates, \mathbf{m}_p and \mathbf{C}_m are *a priori* model and covariance matrix estimates, \mathbf{C}_d the data covariance matrix, and \mathbf{G}_k the current waveform Jacobian matrix. Also, for clarity: $\delta \mathbf{m}_k = \mathbf{m}_{k+1} - \mathbf{m}_k$, $\delta \mathbf{d}_k = \mathbf{d} - g(\mathbf{m}_k)$, and $\delta \mathbf{m}_p = \mathbf{m}_p - \mathbf{m}_k$, where $g(\cdot)$ is the forward modeling operator.

While \mathbf{G}_k possesses a sizable zero component, it is generally non-sparse. Thus, the m -by- m matrix $\mathbf{G}_k^T \mathbf{C}_d^{-1} \mathbf{G}_k + \epsilon^2 \mathbf{C}_m^{-1}$, where m is the dimension of \mathbf{m} , is likely fully dense. In the case of the SEMum model of *Lekic and Romanowicz (2010)*, where $m \simeq 38500$, wall-clock times of approximately one day were observed during assembly and sequential solution of the above system using MATLABTM on a modern workstation. Further,

repeated solution is required at each linearized iteration ($k \rightarrow k + 1$) in order to evaluate model sensitivity to regularization. Thus, parallel solution for the regularized Gauss-Newton update described above is a desirable capability.

A parallel solver mimicking the functionality of the sequential code was developed and validated, utilizing the Scalable Linear Algebra PACKage (ScaLAPACK) - named for its attractive weak-scaling behavior on large dense problems such as these (*Choi et al., 1996*). A robust parallel implementation of LU decomposition with partial pivoting was used. Benchmark tests were performed for realizations of the above system arising in the development of SEMum, and wall-clock solve times for a range of processor grids are shown in Table 2.1.

| Processor Cores | 4 | 16 | 64 |
|--------------------------|------|------|-------|
| Mean Wall-clock Time (s) | 4388 | 1612 | 464.7 |

Table 2.1: Mean wall-clock times for a series of validation solves.

Perhaps most importantly, this savings in compute-time allows for faster and more detailed enumeration of model sensitivity to regularization - hopefully leading to greater flexibility in scheduling of compute resources for far heavier workloads, such as wavefield modeling with the Spectral Element Method (SEM: e.g. *Komatitsch and Vilotte, 1998*).

15.3 Synthetic tests of alternative data-partitioning schemes

The simple isotropic model underlying the SPICE “preliminary” benchmark contains three large ($r > 2500$ km) and five small ($r \simeq 1000$ km) columnar V_s perturbations of $\pm 2.5\%$ and $\pm 6\%$ respectively, from which V_p and ρ are scaled (*Qin et al., 2008*). These structures have roughly Gaussian profile and extend from the surface to the CMB. The associated SEM synthetic dataset is valid to 50 s period, which we further bandpass filtered with corners at 80 and 250 s and cutoff at 60 and 400 s. Following the waveform partitioning and weighting scheme of *Li and Romanowicz (1996)*, first and second orbit Rayleigh wave fundamental mode and overtone wavepackets were selected from vertical component waveforms for all 27 synthetic events recorded at the 256 stations in the dataset.

While maintaining a 1D crust, we inverted for mantle structure using the path-average approximation (PAVA:

Woodhouse and Dziewonski, 1984) and non-linear asymptotic coupling theory (NACT: Li and Romanowicz, 1995) for fundamental mode and overtone data, respectively. We partitioned the inversion at ~ 300 km, below which the resolving power of fundamental mode data rapidly decreases, and adjusted the relative weight assigned to the fundamental mode and overtone datasets in each partition. We found that we could more effectively extend model sensitivity into the transition zone over simply merging the datasets with a uniform weighting. The cubic spline model parametrization was kept continuous across the partition so that the model would remain smooth. This represents a methodology broadly consistent with Berkeley tomographic studies to date.

To explore alternative approaches to optimizing depth sensitivity, we proposed a simple multi-frequency scheme. Overlapping filters with cutoff periods of 60/140 s, 120/200 s, and 180/260 s were applied to SPICE vertical component waveforms, which were further weighted according to path redundancy as in Li and Romanowicz (1996), as well as maximum waveform amplitude. As the filtered waveforms are dominated by fundamental mode surface waves, we chose to invert full waveforms using PAVA only. During the inversion, sensitivities of each of the filtered datasets were independently weighted to maximize smoothness of total sensitivity with depth. Unsurprisingly, resolution of structure through the transition zone, best constrained by overtone surface waves, was notably degraded relative to the wavepacket-partitioned inversion. A far more complex multi-frequency scheme (e.g. AMI: Lebedev *et al.*, 2005) would likely be required in order to compete with the wavepacket-based scheme.

As approximate forward modeling schemes are supplanted by SEM in waveform tomography (e.g. SEMum: Lekic and Romanowicz, 2010), mitigation of computational cost takes on new importance. One proposed solution is the source-stacking technique (Capdeville *et al.*, 2005). Linearity of the elastic wave equation with respect to source implies that SEM waveforms stacked over individual sources are equivalent to those resulting from simultaneous triggering of sources in a single simulation. Thus, inversion of source-stacked traces may provide a novel avenue for waveform tomography at vastly reduced cost. As a naïve test, we sought to invert the SPICE preliminary benchmark using PAVA for both the sensitivity kernels and as a stand-in for SEM.

Vertical component SPICE synthetic waveforms were bandpassed with corners at 120 and 250 s (cutoff at 100 and 400 s), aligned on event origin time, weighted by scalar moment magnitude, and stacked over all 27 events. PAVA sensitivity kernels and synthetics were similarly weighted and stacked. Using these approximate methods alone, the structure of the SPICE model became recognizable as early as the second inversion iteration (see Figure 2.30). Of course, while these results are highly

preliminary and do not reflect realistic data reliability and noise conditions, they reiterate the promise of the source stacking method. Overcoming the shortcomings present in realistic datasets, as well as developing methods for optimized event-station clustering, are of primary concern moving forward.

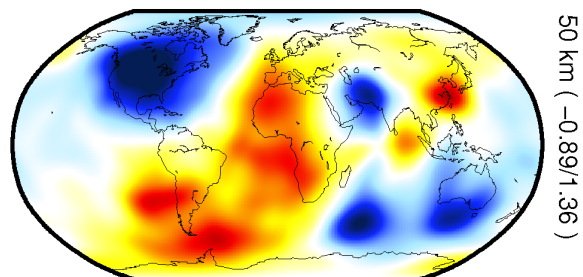


Figure 2.30: Depth snapshot at 50 km after stacked-waveform inversion iteration 2, PAVA only.

15.4 Acknowledgements

This research was supported by National Science Foundation grant NSF/EAR-0738284.

15.5 References

- Capdeville, Y., Y. Gung, and B. Romanowicz, Towards global earth tomography using the spectral element method: a technique based on source stacking, *Geophys. J. Int.*, 162, 541-554, 2005.
- Choi, J., J. Demmel, I. Dhillon, J. Dongarra, S. Ostrouchov, A. Petit, K. Stanley, D. Walker, and R.C. Whaley, ScaLAPACK: a portable linear algebra library for distributed memory computers - design issues and performance, *Comp. Phys. Comm.*, 97, 1-15, 1996.
- Komatitsch, D. and J. Vilotte, The spectral element method: an efficient tool to simulate the seismic response of 2D and 3D geological structures, *Bull. Seism. Soc. Am.*, 88, 368-392, 1998.
- Lebedev, S., G. Nolet, T. Meier, and R.D. van der Hilst, Automated multimode inversion of surface and S waveforms, *Geophys. J. Int.*, 162, 951-964, 2005.
- Lekic, V. and B. Romanowicz, Inferring upper mantle structure by full waveform tomography with the Spectral Element Method, Submitted to *Geophys. J. Int.*, 2010.
- Li, X.D. and B. Romanowicz, Comparison of global waveform inversions with and without considering cross-branch modal coupling, *Geophys. J. Int.*, 121, 695-709, 1995.
- Li, X.D. and B. Romanowicz, Global mantle shear-velocity model developed using nonlinear asymptotic coupling theory, *Geophys. J. R. Astr. Soc.*, 101, 22,245-22,272, 1996.
- Qin, Y., Y. Capdeville, V. Maupin, J.-P. Montagner, S. Lebedev, and E. Beucler, SPICE Benchmark for global tomographic methods, *Geophys. J. Int.*, 175, 598-616, 2008.
- Tarantola, A., *Inverse problem theory and methods for model parameter estimation*, SIAM, 2005.
- Woodhouse, J.H. and A.M. Dziewonski, Mapping the upper mantle: Three dimensional modeling of earth structure by inversion of seismic waveforms, *J. Geophys. Res.*, 89, 5953-5986, 1984.

16 Towards Constraining Lateral Variation of Attenuation Structure With Low-Degree Normal Modes Splitting Coefficients

Shan Dou and Barbara Romanowicz

16.1 Introduction

The study of attenuation is very challenging because of the complexity in its measurements and interpretation. However, attenuation is important for at least two reasons:

1) Attenuation is considerably more sensitive to temperature variations than elastic velocities. While elastic velocities have a quasi-linear dependence upon temperature variations, seismic attenuation depends exponentially on temperature (e.g., *Jackson, 1993; Karato, 1993*). Therefore, attenuation tomography is important for studying temperature variations within the Earth, and combining elastic and anelastic studies has the potential to separate different effects of chemical composition, water content, partial melting, etc.

2) Attenuation causes physical dispersion of seismic velocities, and this effect needs to be corrected for in velocity models.

16.2 Motivation and Theory

The two large regions of low shear velocity (Very Low Shear Velocity Provinces, denoted as LLSVPs in the following content) in the lowermost mantle located beneath the south-central Pacific Ocean and southern Africa/southern Atlantic/Southern Indian ocean regions are unusual deep structures that could offer important indications about the dynamic structures. Because these two LLSVPs each have a lateral extent that is much greater than what might be expected for a hot upwelling plume rising from a thermal boundary layer, they are usually referred to as “superplumes.” However, resolving the dynamical significance of these large scale features is nontrivial as well as complicated: Low velocities may be caused by high temperatures or by chemical differences or the competing effects of the two. A variety of body wave studies have reported large velocity anomalies (varying from 1% to 10%) and strong lateral gradients (e.g. *Ritsma et al., 1998; Ni and Helmberger, 2003a, 2003b; Wen et al., 2001; Wang and Wen, 2004, 2006; Tanaka, 2002; Toh et al., 2005; Ford et al., 2006; He et al., 2006*). Shear wave velocities tend to reduce at deep-mantle pressures, and thus lateral variations of 500 ~ 1000_o over ~ 100 km are needed to contribute to the observed velocity anomalies. Thermal anomalies to this extent could lead to the onset of partial melting that can generate strong velocity reductions. On the other hand, of chemical variations appear to be important in LLSVPs, the temperature contrasts may be far lower.

Comparing P-wave and S-wave velocities can offer important indications that LLSVPs involve chemical heterogeneities. One of the most important results from previous studies is that LLSVPs have a bulk-sound-velocity anomaly that is anti-correlated with the shear wave velocity anomalies (e.g. *Resovsky and Trampert, 2003; Trampert et al., 2004*). Several normal modes studies (*Ishii and Tromp, 1999; Trampert et al., 2004*) also indicate that density heterogeneity exists at the base of the mantle, which is dominated by the two LLSVPs on a large scale. The anti-correlation between density and shear velocity anomalies that are proposed in these studies favors chemical heterogeneity. This remains a topic of controversy (e.g. *Romanowicz, 2001; Kuo and Romanowicz, 2002*), but at the same time, it is equally critical to better resolve the density and anelastic structure to assess the effect of thermal buoyancy and chemical negative buoyancy. Nonetheless, resolving the attenuation signature of LLSVPs is quite challenging due to the contamination from the elasticity effect and strong lateral variations existing in the upper mantle. Because surface waves lose their sensitivity to such deep structures, lower mantle tomography mostly relies on deep-turning teleseismic body waves and normal mode data. Different from body wave datasets that could be degraded by uneven distribution of events and stations, the Earth’s free oscillations involve the vibration of the whole planet and thus are much less likely to be biased by source-receiver geometry. In this way, information carried by normal modes signals can serve quite well for the purpose of exploring the physics properties of the large scale lateral variations in the lowermost mantle.

For normal mode multiplets well isolated in complex frequency, the effect of even-order aspherical structure on the splitting behavior of the spectra can be quantitatively represented by a discrete set of “splitting coefficients.” These coefficients determine the coupling of the singlets within a multiplet. The splitting coefficients describe a radial average of three-dimensional heterogeneity, and can be related to internal properties by:

$$c_{st} = e_{st} + ia_{st}$$

$$e_{st} = \int_0^a \delta m_s^t(r) K_s(r) r^2 dr + \sum_d h_{sd}^t B_{sd} r_d^2$$

$$a_{st} = \int_0^a (\delta q_{\kappa s}^t K_{q\kappa} + \delta q_{\mu s}^t K_{q\mu}) r^2 dr$$

Owing to the high quality digital data set assembled in the last 20 years on the global broadband seismic network, and owing to the occurrence of several very large earthquakes, putting new constraints on the large-scale attenuation in the lower mantle from normal modes is promising.

16.3 Preliminary Results and Prospective Work

We applied the Iterative Spectral Fitting (ISF) method (Ritzwoller *et al.* 1986, 1988) in the study. In the ISF approach, the technique breaks down naturally into two parts: A discrete regression for the interaction coefficients for a number of lower mantle sensitive modes followed by a continuous inverse problem to solve for the three-dimensional structure from the splitting coefficients. Figure 2.31 shows examples of elastic splitting functions obtained from the ISF approach, and we can clearly see the dominant degree-2 pattern in all of the mantle modes shown in the figure.

We applied the same technique to resolve anelastic splitting coefficients, but due to the data noise and very limited size of the dataset used in the study, the retrieved anelastic coefficients are generally below the error level, and appear to be quite unstable and strongly rely on the elastic starting model. With more data involved in the inversion, and more optimum regularization design, we hope to improve the stability of the anelastic splitting coefficients and then go further to invert for a three-dimensional anelastic model of the lower mantle from normal modes. Even if we can only resolve the longest wavelengths (degrees 2 or possibly up to 4), this will be important for the understanding of the nature of the two low velocity regions at the base of the mantle, commonly referred to as “superplumes,” whose thermo-chemical nature is still under debate (e.g. Masters *et al.*, 1982; Romanowicz, 1998; Bijwaard and Spakman, 1999; Ishii and Tromp, 1999; Romanowicz, 2001; Trampert *et al.*, 2004; Gung and Romanowicz, 2004; Anderson, 2005).

16.4 References

Ritzwoller M, Masters G, and Gilbert F, Observations of anomalous splitting and their interpretation in terms of aspherical structure with low frequency interaction coefficients: Application to uncoupled multiplets, *Journal of Geophysical Research*, 91, 10203-10228, 1986.

Ritzwoller M, Masters G, and Gilbert F, Constraining aspherical structure with low frequency interaction coefficients: Application to uncoupled multiplets, *Journal of Geophysical Research*, 93, 6369-6396, 1988.

Romanowicz B and Mitchell B, Deep Earth Structure — Q of the Earth from Crust to Core, *Treatise on Geophysics*, Volume 1, 775-803, 2007.

Widmer-Schmidrig R and Laske G, Theory and Observations — Normal Modes and Surface Wave Measurements, *Treatise on Geophysics*, Volume 1, 67-125, 2007.

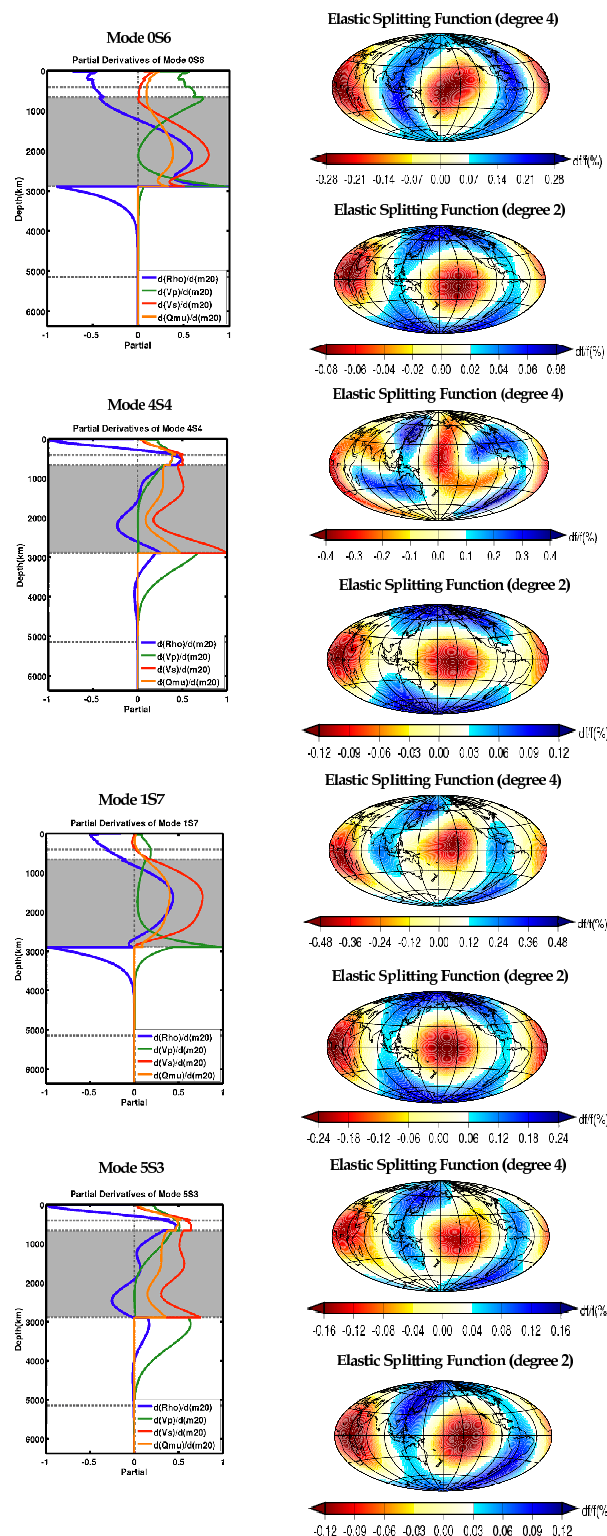


Figure 2.31: Examples of splitting function for mantle-sensitive modes $0S_6$, $4S_4$, $1S_7$, and $5S_3$

17 Efficient Computation of NACT Seismograms: Toward Application in Imaging Upper Mantle Discontinuities

Zhao Zheng and Barbara Romanowicz

17.1 Introduction

The Berkeley Global Seismology group has been developing global mantle tomographic models (*Li and Romanowicz, 1996; Mégnin and Romanowicz, 2000; Pan-ning and Romanowicz, 2006*) by inverting a dataset of surface waveforms down to 60 sec and long-period body waveforms down to 32 sec. A normal mode coupling method known as the Non-linear Asymptotic Coupling Theory (NACT; *Li and Romanowicz, 1995*) has been successfully applied to compute 3D synthetic seismogram and sensitivity kernels. It is an approximate approach which collapses sensitivity over the whole volume onto the vertical plane containing source and receiver. By taking into account the depth variation of sensitivity, NACT is able to bring out the ray character of body waves as well as the finite-frequency behavior of sensitivity kernels. On the other hand, as an approximate approach, it is computationally much faster than purely numerical methods such as the Spectral Element Method (SEM).

The frequency band (≥ 32 sec) of the current tomographic dataset is too low to retrieve fine scale structures of upper mantle discontinuities, which place vital constraints on the temperature, composition and dynamics of the mantle. In order to retrieve them, it is necessary to incorporate phases such as the *SS* precursors.

Most *SS* precursor studies so far measure *SS-SdS* differential travel time and translate that to discontinuity depth, therefore suffering from the tradeoff between volumetric perturbation and discontinuity topography (for a review, see *Deuss, 2009*). Modeling the 3D waveforms of precursors will help to resolve this tradeoff. However, these precursor phases are typically peaked at a much shorter period (~ 10 sec), therefore presenting a great computational challenge to the current mode coupling scheme of NACT, in which the computational cost grows as f_{max}^4 with f_{max} being the cutoff frequency.

17.2 An Efficient NACT Formalism

In the NACT theory, the perturbed seismogram consists of an along-branch coupling term, which is computed under the well-known PAVA approximation (*Woodhouse and Dziewonski, 1984*), and an across-branch coupling term, which is computed under the linear Born approximation. In the classical formalism, the Born part is obtained by a double summation over all

pairs of coupling modes (*Li and Romanowicz, 1995*):

$$\delta u(t) = \sum_k \sum_{k'} A_{kk'} \frac{\exp(i\omega_k t) - \exp(i\omega_{k'} t)}{\omega_k^2 - \omega_{k'}^2} \quad (2.3)$$

where $k = (n, l)$ and $k' = (n', l')$ are indices for normal modes (n the radial and l the angular order), and

$$A_{kk'} = \sum_m \sum_{m'} R_k^m H_{kk'}^{mm'} S_{k'}^{m'} \quad (2.4)$$

where R_k^m and $S_{k'}^{m'}$ (m being the azimuthal order of normal mode) are the receiver and source terms as defined in *Woodhouse and Girnius (1982)*, and the coupling matrix $H_{kk'}$ due to perturbation in the elastic tensor \mathbf{C} is:

$$H_{kk'}^{mm'} = \int_V \mathbf{e}_k^{m*}(\mathbf{r}; \mathbf{r}_R) : \delta \mathbf{C}(\mathbf{r}) : \mathbf{e}_{k'}^{m'}(\mathbf{r}; \mathbf{r}_S) dV \quad (2.5)$$

with \mathbf{e}_k^m being the strain of mode (k, m) , subscript R and S for the location of seismic receiver and source, “*” denoting complex conjugate, and “:” double dot product.

In practice, the summation is truncated below some cutoff frequency f_{max} . Since the number of modes with eigenfrequencies below a certain cutoff frequency is roughly proportional to f_{max}^2 , the cost of computing one seismogram grows with frequency as f_{max}^4 . For multiple sources and receivers, the computational cost goes $(N_S * N_R) * f_{max}^4$, where N_S and N_R are the number of sources and receivers, respectively.

Here we present a more efficient formalism. From the physical inspiration that the Born approximation is a single-scattering approximation, i.e., the seismic wavefield due to a heterogeneity scatterer is the convolution of a source-to-scatterer term and a scatterer-to-receiver term, we see it is possible to separate the double summation over mode pairs to two single summations (*Capdeville, 2005*). In particular, the Born seismogram can be expressed in the frequency domain as (*Tanimoto, 1984*):

$$\delta u(\omega) = \sum_k \sum_{k'} A_{kk'} \frac{1}{i\omega(\omega^2 - \omega_k^2)(\omega^2 - \omega_{k'}^2)} \quad (2.6)$$

Upon substituting (2) in (4) and separating the terms that are indexed by (k, m) and those by (k', m') , one finds

$$\delta u(\omega) = \int_V \mathbf{R}(\mathbf{r}, \omega) : \delta \mathbf{C}(\mathbf{r}) : \mathbf{S}(\mathbf{r}, \omega) dV \quad (2.7)$$

with

$$\mathbf{R}(\mathbf{r}, \omega; \mathbf{r}_R) = \sum_k \left(\sum_m R_k^m \mathbf{e}_k^{m*} \right) \frac{1}{\omega^2 - \omega_k^2} \quad (2.8)$$

$$\mathbf{S}(\mathbf{r}, \omega; \mathbf{r}_S) = \sum_{k'} \left(\sum_{m'} S_{k'}^{m'} \mathbf{e}_{k'}^{m'} \right) \frac{1}{i\omega(\omega^2 - \omega_{k'}^2)} \quad (2.9)$$

accounting for the scatterer-to-receiver and the source-to-scatterer contributions, respectively. Returning to the time domain, one can write

$$\delta u(t) = \int_V \mathbf{R}(\mathbf{r}, t) : \delta \mathbf{C}(\mathbf{r}) \star : \mathbf{S}(\mathbf{r}, t) dV \quad (2.10)$$

with

$$\mathbf{R}(\mathbf{r}, t; \mathbf{r}_R) = \sum_k \left(\sum_m R_k^m \mathbf{e}_k^{m*} \right) \frac{\sin(\omega_k t)}{\omega_k} \quad (2.11)$$

$$\mathbf{S}(\mathbf{r}, t; \mathbf{r}_S) = \sum_{k'} \left(\sum_{m'} S_{k'}^{m'} \mathbf{e}_{k'}^{m'} \right) \frac{1 - \cos(\omega_{k'} t)}{\omega_{k'}^2} \quad (2.12)$$

and “ \star ” in (8) denoting temporal convolution.

As commented by *Capdeville* (2005), this formalism is similar to the adjoint method (e.g. *Tarantola*, 1984). Since the summations in (9) and (10) can be performed simultaneously, the cost of computing one seismogram now grows as f_{max}^2 as opposed to f_{max}^4 in the original NACT. For multiple paths, the cost is $(N_S + N_R) * f_{max}^2$, as compared to $(N_S * N_R) * f_{max}^4$. Asymptotic approximation can still be applied to collapse the integral over whole volume in (8) onto the great circle plane, as did the original NACT.

17.3 Numerical Validation

A numerical test is designed to validate the new formalism. Synthetic seismograms are computed for a path geometry shown in Figure 2.32 using the old and new formalisms, respectively. The result shows that the two synthetics agree very well in both phase and amplitude.

Table 2.2 lists the CPU time of computing a single synthetic seismogram with the two formalisms, respectively, for several cutoff frequencies. Time cost of the new formalism scales roughly as f_{max}^2 , whereas that of the original NACT scales as f_{max}^3 (rather than the theoretically f_{max}^4 , because in practice the mode coupling was restricted to some fixed coupling width s such that $|l' - l| \leq s$, where l is the angular order of modes). Therefore, the new formalism is computationally preferable when approaching higher frequencies. It is even more advantageous in the case of many sources and receivers, which is the reality of seismic tomography.

17.4 References

Capdeville, Y., An efficient Born normal mode method to compute sensitivity kernels and synthetic seismograms in the Earth, *Geophys. J. Int.*, 163, 639-646, 2005.

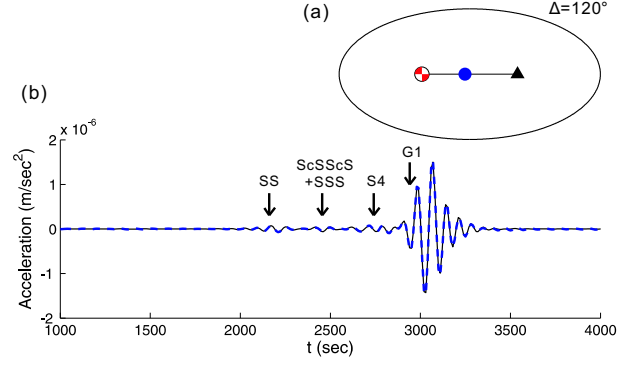


Figure 2.32: (a) Path geometry of the numerical test. A cylindrical anomaly (blue) between 0 and 1000 km depth with 2% faster V_S than PREM is located halfway between the source and the receiver. (b) Transverse component synthetic seismogram computed up to 60 sec with the original NACT (black line) versus the new formalism (blue dashed line). Major seismic phases are labeled.

Table 2.2: Time cost for computing one synthetic seismogram on a 1 GHz single CPU.

| f_{max} (period) | original NACT | new formalism |
|--------------------|---------------|---------------|
| 60 sec | 6.9 min | 22 min |
| 30 sec | 56 min | 72 min |
| 10 sec | 25 hr | 10 hr |

Deuss, A., Global observations of mantle discontinuities using SS and PP precursors, *Surv. Geophys.*, 30, 301-326, 2005.

Li, X.D. and B. Romanowicz, Comparison of global waveform inversions with and without considering cross-branch modal coupling, *Geophys. J. Int.*, 121, 695-709, 1995.

Li, X.D. and B. Romanowicz, Global mantle shear-velocity model developed using nonlinear asymptotic coupling theory, *J. Geophys. Res.*, 101(B10), 22,245-22,272, 1996.

Méglin, C. and B. Romanowicz, The three-dimensional shear velocity structure of the mantle from the inversion of body, surface and higher-mode waveforms, *Geophys. J. Int.*, 143(3), 709-728, 2000.

Panning, M. and B. Romanowicz, A three dimensional radially anisotropic model of shear velocity in the whole mantle, *Geophys. J. Int.*, 167, 361-379, 2006.

Tanimoto, T., A simple derivation of the formula to calculate synthetic long-period seismograms in a heterogeneous earth by normal mode summation, *Geophys. J. Int.*, 77, 275-278, 1984.

Tarantola, A., Inversion of seismic reflection data in the acoustic approximation, *Geophysics*, 49, 1259-1266, 1984.

Woodhouse, J.H. and A.M. Dziewonski, Mapping the Upper Mantle: Three-Dimensional Modeling of Earth Structure by Inversion of Seismic Waveforms, *J. Geophys. Res.*, 89(B7), 5953-5986, 1984.

Woodhouse, J.H. and T.P. Girnius, Surface waves and free oscillations in a regionalized earth model, *Geophys. J. R. Astr. Soc.*, 68(3), 653-673, 1982.

18 Modeling of the Byerly’s False S Phase

David Dolenc (U of Minnesota) and Doug Dreger

18.1 Introduction

Byerly’s False S phase was first observed more than 70 years ago (Byerly, 1937) for earthquakes off the coast of Northern California. We used the recent dense station coverage in the region (USArray, Northern California Seismic Network, Berkeley Digital Seismic Network, Mendocino Array) to study the False S observations. We identified offshore events that produced the False S phase, relocated them using a double-difference algorithm, and inverted for the seismic moment tensor. With the location and source parameters constrained, we modeled the broadband waveforms using 2D and 3D velocity structures to find the origin of the False S arrivals.

18.2 History of False S

Byerly (1937) observed False S for the events located in the Mendocino Triple Junction (MTJ) at the stations to the south in the 2°-9° distance range. The speed of False S and the fact that the phase died out at distance led Byerly to believe that False S is a P wave that propagated through the sedimentary layer. However, Byerly noted that False S was not observed at Ferndale, the closest station to the MTJ at that time, and concluded that his proposed origin of the False S was open to objection. Cameron (1961) determined that False S is a longitudinal wave that arrives at the observing stations with a small angle of emergence. He also concluded that False S could be a P wave that propagated in the upper sedimentary layer. Oliver and Major (1960) suggested that False S results from the amplitude variation in the leaking-mode propagation within the near-surface wave guide. Maulik (1964) tried to explain the propagation of the phase through the sedimentary layer and concluded that a similar “false” phase should follow the true S wave, corresponding to S-wave propagation in the sedimentary layer. However, no such phase was observed. Ghosh (1964) suggested that False S resulted from the Stoneley wave propagating along the inclined continental margin. But Auld *et al.* (1969) showed that the phase was not observed at an ocean-bottom seismometer and ruled out the Stoneley-wave hypothesis.

18.3 Results

Our analysis of the offshore Mendocino events showed that (1) False S is observed for some offshore events along the Mendocino Escarpment (E of 127°W) and to the north (up to 41°N), (2) for events that generate False S, the phase is always observed on the near-coast sta-

tions north of the MTJ (up to station L02A), (3) events that generate False S always generate False S at the near shore station JCC, (4) False S is never observed at the closest stations KCT and KMPB, (5) strong False S is observed when the S phase is strong, (6) for strong False S events, the phase can be observed to the south, all the way to the San Francisco Bay region, and (7) no “false” phase after the true S wave is observed. The results support our starting hypothesis that False S is an SP phase that propagates as an S wave through the crustal layer above the Gorda plate and is refracted as a P wave back to the surface when it hits the thicker part of the subducting plate. This model can explain (1) the time delay between P and False S, (2) why a strong False S is observed when the S phase is strong, (3) why False S is never observed at the closest stations, (4) why the phase dies out at long distances, and (5) why False S phase has a small angle of emergence. We modeled the False S observations by developing a network of 2D structures to explain False S on all the stations leading to 3D modeling. The results showed that the origin of the False S phase could be explained by simple 2D modeling. The finite-difference modeling so far could not reproduce the False S observations. We are further testing the 2D and 3D models using finite-difference code to complete this work.

18.4 Acknowledgements

This project was funded by NSF grant EAR-0745803. We thank R. Allen, E. Humphreys, and A. Levander for sharing the Mendocino Array data with us.

18.5 References

- Auld, B. et al., Seismicity off the coast of northern California determined from ocean bottom seismic measurements, *Bull. Seism. Soc. Am.*, 59, 2001-2015, 1969.
- Byerly, P., Earthquakes off the coast of northern California, *Bull. Seism. Soc. Am.*, 27, 73-96, 1937.
- Cameron, J. B., Earthquakes in the northern California coastal region (Part II), *Bull. Seism. Soc. Am.*, 51, 337-354, 1961.
- Ghosh, M. L., On a possible explanation of the PF-phase, *Bull. Seism. Soc. Am.*, 54, 1417-1427, 1964.
- Maulik, T. N., On the PF and other phases in the early part of seismogram, *Pure and Applied Geophysics*, 58, 49-62, 1964.
- Oliver, J. and M. Major, Leaking modes and the PL phase, *Bull. Seism. Soc. Am.*, 50, 165-180, 1960.
- Zelt, C. A. and R. B. Smith, Seismic traveltimes inversion for 2-D crustal velocity structure, *Geophys. J. Int.*, 108, 16-34, 1992.

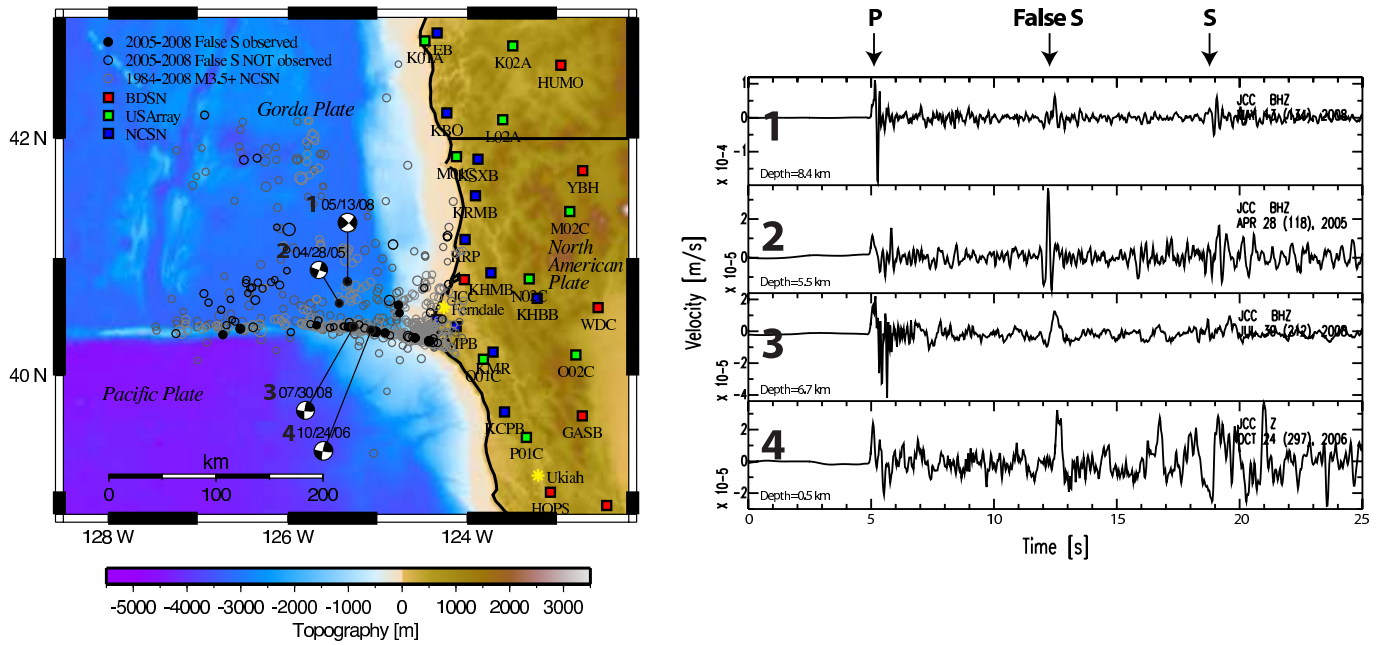


Figure 2.33: Left: Locations of the offshore events included in the study. Filled black circles are 2005-2008 events for which False S was observed on at least some stations. Open black circles are 2005-2008 events for which False S was not observed. Right: Velocity waveforms for the four numbered events. Shown is the vertical JCC component that had instrument response deconvolved.

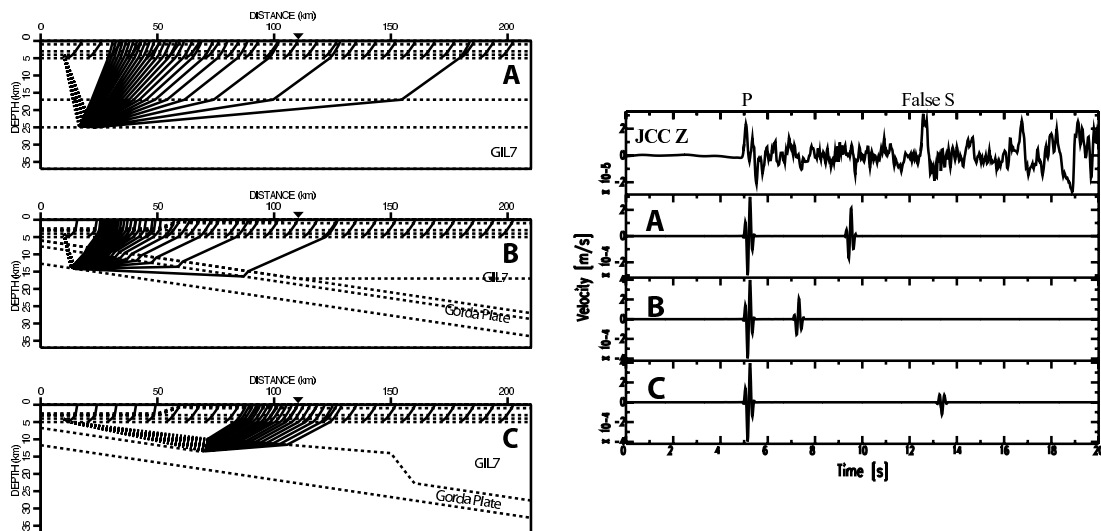


Figure 2.34: Example of 2D ray-tracing (RAYINV; *Zelt and Smith, 1992*) used to model travel times and amplitudes. Left: (A) P-wave modeled as a head wave that propagated just below the 5 km interface. We looked for the phase that arrives at the station as a P wave, does not reflect more than once, and arrives with the largest possible delay relative to P. The resulting phase SP is shown on the right. (B) Gorda plate is modeled as a 2-layer slab with a 6° dip. The phase that has the largest delay relative to the P-wave and satisfies the above conditions is shown as an SP phase that is reflected at the bottom of the Gorda plate. (C) Gorda plate has non-uniform thickness. S wave propagates through the GIL7 crustal layer above the Gorda plate, and when it hits the thicker part of the Gorda plate, it is refracted back to the surface as a P wave. This type of model can explain the observed time delay between P and False S. Right: Synthetic seismograms for the 3 models are compared to the observations at JCC. Only model C can produce a phase that has travel-time comparable to that of the observed False S.

19 ShakeAlert: A Unified EEW System for California

Holly Brown, Richard Allen, Maren Böse (Caltech), Georgia Cua (ETH), Egill Hauksson (Caltech), Thomas Heaton (Caltech), Margaret Hellweg, Oleg Khainovski, Doug Neuhauser, Kalpesh Solanki (Caltech), Michael Fischer (ETH)

19.1 Introduction

Earthquake Early Warning (EEW) is a method of rapidly identifying an earthquake in progress and transmitting warning messages to nearby population centers before damaging ground shaking arrives. The first few seconds of the initial P-wave arrival are used to detect the event and predict magnitude and peak shaking from a single or multiple stations, and combined station detections are used to locate the event. Warnings of imminent shaking can be used to activate automatic safety measures, such as slowing down trains, isolating sensitive factory equipment, or opening elevator doors. Warnings can also be sent directly to the public via cell phone, computer, television, or radio.

The Berkeley Seismological Laboratory (BSL) worked for several years to develop the Earthquake Alarm Systems (ElarmS), an EEW system specifically for California. ElarmS was tested in conjunction with two other prototype EEW systems in a three-year proof of concept project by the California Integrated Seismic Network (CISN) to demonstrate the potential for EEW in California. In August 2009, the proof of concept project was completed and declared a success. The CISN EEW partners, the BSL, the California Institute of Technology (Caltech) and the Swiss Institute of Technology (ETH), are now collaborating again in a new three-year project, to build a single, integrated, production-grade system for testing purposes in California. The new system, called ShakeAlert, will be capable of continuous long-term operation, exhibit reliability and redundancy during extreme ground shaking, and rapidly provide warning to large numbers of users across the state. ShakeAlert is already under development and will provide warnings to a small group of test users by August 2012.

19.2 Project goals

The new ShakeAlert algorithm utilizes the best aspects of each of the three test systems from the proof-of-concept project. Caltech's OnSite algorithm uses P-wave data from the single station nearest the epicenter to provide an extremely rapid estimate of likely ground shaking. The BSL's ElarmS algorithm and ETH's Virtual Seismologist algorithm use data from multiple stations around an event epicenter to produce a slightly slower but more reliable estimate of magnitude and location. Combining these methods produces an algorithm which has the speed of a single-station method but is then promptly confirmed and adjusted by additional station

data to form a more accurate description of the event.

When an event is identified and determined to be above pre-defined thresholds for magnitude, ground shaking intensity and statistical likelihood, event data is broadcast to system users. Currently, event information is only being sent to the developers while system components are being developed and refined. By 2012, event information will be sent to a small group of test users outside the seismological community. The event data will be received by a user-configurable alert program, which will sound an alarm, predict shaking at the user's specific location, and/or display a map of regional shaking. Emergency responders and regionally diverse industries (e.g. trains, utilities) may choose to display a map, showing multiple points of interest, while an individual may only be concerned with the immediate hazard at their specific location.

19.3 Current Progress

ShakeAlert will be comprised of four primary software components (Figure 2.35). The first, called the Waveform Processing Module, receives seismic waveforms from every early-warning capable seismometer or accelerometer in California (Figure 2.36), identifies P-wave arrivals, and calculates the relevant P-wave parameters necessary for EEW magnitude estimation. The second component, called the Event Monitoring Module, combines the current algorithms from OnSite, Virtual Seismologist, and ElarmS to recognize events in progress and calculate event magnitude and location. The third component, called the Decision Module, can receive event notifications from multiple systems include the existing three test systems and the new integrated system, reviews events, and determines whether to send warnings to users. The final component is the User Display, which will be installed at an EEW user's site. The User Display will receive warnings from the Decision Module and generate an alert message, a map of ground shaking intensities at various locations, or other output, as per the user's preconfigured settings.

During the last year, Caltech programmers developed an initial prototype of the User Display Module, while Berkeley programmers built an initial prototype of the Decision Module to combine output from the three original event monitoring algorithms. The three CISN EEW partners (Caltech, BSL, ETH) are working together to jointly build a new, robust Waveform Processing Module. The BSL, with significant input from the other part-

CISN's New ShakeAlert EEW System

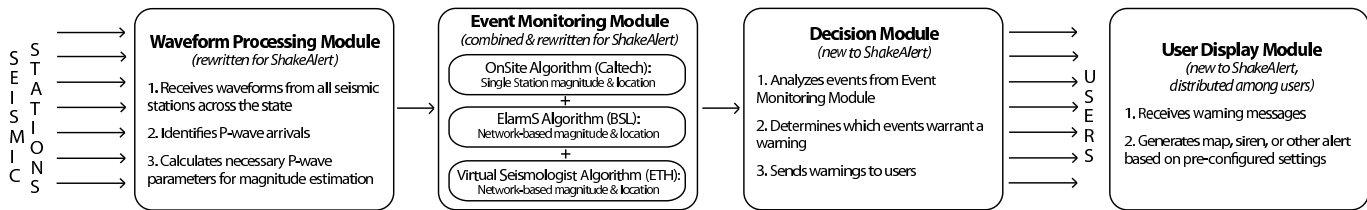


Figure 2.35: Components of the new ShakeAlert EEW System

ners, is also beginning work on the new Event Monitoring Module, combining the three original algorithms into a single, efficient algorithm that takes advantage of the best parts of each original algorithm.

stations provide P-wave data, none of the three original test algorithms offer insight into how to combine data from exactly two stations. The CISN EEW group has been investigating the best method for analyzing two-station events using Bayesian statistics.

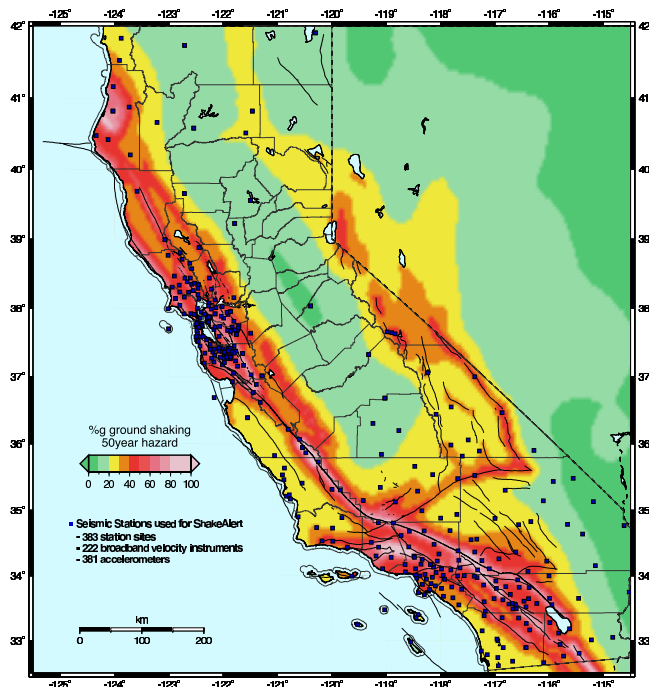


Figure 2.36: Seismic Stations used by ShakeAlert

19.4 Future Steps

During the coming year, the CISN EEW project members will connect all the new modules into a single end-to-end data flow. We will also begin sending warning messages to a few test users outside of the seismology community. Concurrently, we will continue to update and improve our new modules for speed and accuracy. The new event monitoring module in particular presents many opportunities for testing new methods and theories of EEW. While it will use the OnSite algorithm for estimating earthquake characteristics from a single station's P-wave data, and the Virtual Seismologist and ElarmS algorithms for analyzing earthquakes when three or more

19.5 References

Allen, R.M., H. Brown, M. Hellweg, O. Khainovski, P. Lombard, D. Neuhauser, Real-time earthquake detection and hazard assessment by ElarmS across California, *Geophys. Res. Lett.*, *36*, L00B08, doi:10.1029/2008GL036766, 2009.

Allen, R.M., P. Gasparini, O. Kamigaichi, M. Böse, The status of earthquake early warning around the world: An introductory overview, *Seism. Res. Lett.*, *80(5)*, 682-693, 2009.

Böse, M., E. Hauksson, K. Solanki, H. Kanamori, T.H. Heaton, Real-time testing of the on-site warning algorithm in southern California and its performance during the July 29 2008 M_w 5.4 Chino Hills earthquake, *Geophys. Res. Lett.*, *36*, L00B03, doi:10.1029/2008GL036366, 2009.

Cua, G., M. Fischer, T. Heaton, S. Wiemer, Real-time performance of the Virtual Seismologist earthquake early warning algorithm in southern California, *Seism. Res. Lett.*, *80(5)*, 740-747, 2009.

20 January 10, 2010 M_w 6.5 Gorda Plate Earthquake: Automated Finite-Source Modeling

Douglas S. Dreger

20.1 Introduction

On January 9, 2010 at 16:27:38 (January 10, 00:27:38 UTC) a M_w 6.5 Gorda Plate event occurred approximately 43 km offshore of Ferndale, California. Despite its offshore location it was well recorded by broadband, strong motion and GPS stations operated by the BSL, USGS, and CGS (California Geological Survey). Several years ago, we implemented finite-source inversion algorithms to rapidly, and automatically determine the causative fault plane of an earthquake from the automatic seismic moment tensor solution (e.g. *Pasyanos et al.*, 1996), and to solve for both line and planar models of the slip distribution (e.g. *Dreger and Kaverina*, 2000, and *Dreger et al.*, 2005).

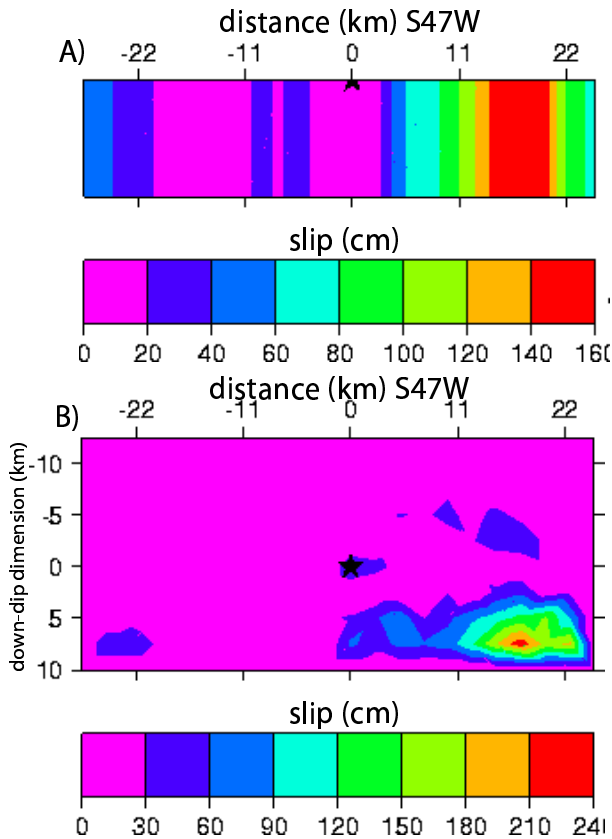


Figure 2.37: A) Line-source slip model. B) Plane-source slip model. In both cases the hypocenter is at 16.9 km depth. Both models show unilateral rupture to the SW.

20.2 Automatic Finite-Source Solutions

The moment tensor solution (Figure 2.39) is typical for this offshore region with near-vertical nodal planes and a predominant strike-slip motion. Events in the offshore region occur on both the NW and NE striking nodal planes. The November 8, 1980 M7.2 Mendocino earthquake occurred on a NE striking plane approximately 50 km NW of the 2010 event.

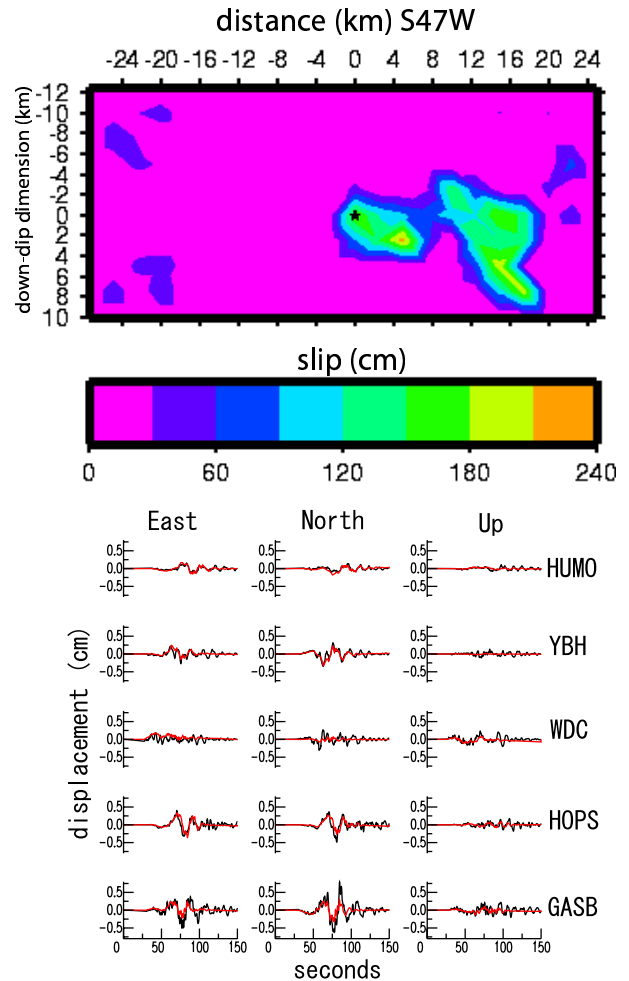


Figure 2.38: Revised slip model obtained by adjusting hypocenter depth to 21.7 km and adjusting the timing of Green's functions to align with observed S-wave arrival times. Broadband (0.01 to 10 Hz) data (black) and synthetics (red) are compared. The same amplitude scale was used for all stations.

The automatic finite-source code tested both nodal plane orientations with both line-source (Figure 2.37A) and plane-source (Figure 2.37B) slip inversions of three-component broadband (0.01 to 10 Hz) displacement waveforms. Despite the poor station coverage due to the offshore location of the earthquake, the stations do sample enough of the focal sphere to capture the directivity of the event. These automatic finite-source calculations were completed within 22 minutes of the occurrence of the earthquake, and the results showed that the NE striking nodal plane was the causative structure. Furthermore, as Figure 2.37 shows, the earthquake ruptured unilaterally to the SW, away from the coast, on the NE striking fault plane. The scalar seismic moment of the plane-source model is 6.76×10^{25} dyne cm, corresponding to M_w 6.5. A rise time of 1 second was assumed, and the best fitting rupture velocity was 2.2 km/s.

The initial hypocentral depth was 16.4 km, which was used in the finite-source calculations. Figure 2.37 suggests that the actual slip is deeper. The moment tensor solution yielded a centroid depth of 24 km. Revisions of the hypocenter location resulted in updates of the depth to 21.7, and 29.3 km.

20.3 Finite-Source Model Revisions

The initial analyst review of the automatic solution updated the hypocenter to the first revised depth of 21.7 km, and a 1 second timing adjustment was applied to all stations to align the Green's functions to the observed S-wave arrivals. A rise time of 2 seconds (increased from 1 second to match the long-period character of the data) and the 2.2 km/s rupture velocity from the automatic processing were assumed. The revised solution (Figure 2.38) shows the rupture was unilateral to the SW with slip occurring in the 17 to 30 km depth range. The peak slip was 2.7m, and the scalar seismic moment increased to 9.33×10^{25} dyne cm (M_w 6.6).

As Figure 2.38 shows, the fit to the broadband displacement waveforms is quite good. Stations GASB and HOPS have the largest amplitudes. These stations are approximately the same distance from the source as stations HUMO and YBH, which show much lower amplitudes. In fact, the small amplitudes at HUMO, YBH and WDC, and the notably larger amplitudes at GASB and HOPS illustrate the strong directivity of the source.

20.4 Implications for Ground Motion Reporting

Automated finite-source models may be used to improve ShakeMap ground motion reporting by taking the finite rupture extent into account in the computation of ground motions from empirical relations for the purpose of interpolating the observed values (*e.g.* Dreger *et al.*, 2005). Although the application of the finite-source

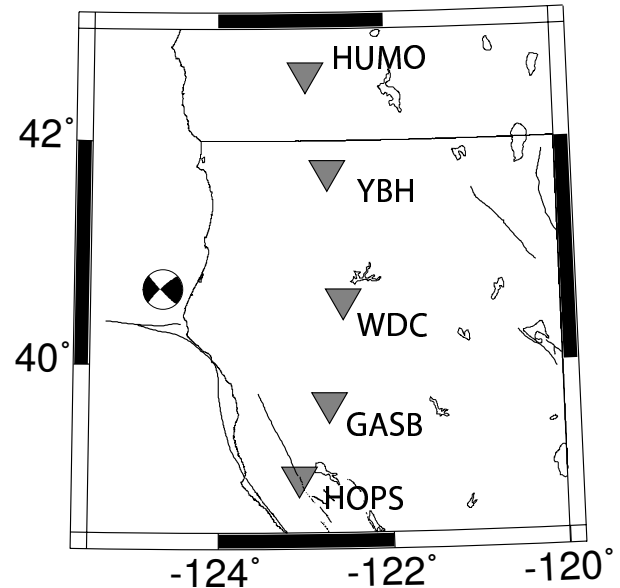


Figure 2.39: Location of event and stations (triangles). The focal mechanism was obtained from moment tensor inversion of long-period (20 to 50 seconds) three-component waveforms.

model in ShakeMap for this event had minimal impact due to the distant offshore location of the event, the 22 minute processing time, and the success of the system in the identification of the causative fault, the slip distribution and the unilateral rupture characteristics, despite the poor station coverage, demonstrates that such information can be made routinely available in a time frame suitable for rapid ground motion reporting.

Ongoing efforts involve improving automated processing times and solutions as well as updating the analyst interface used to examine and revise solutions.

20.5 References

- Dreger, D. S., and A. Kaverina, Seismic remote sensing for the earthquake source processes and near-source strong shaking: A case study of the October 16, 1999 Hector Mine earthquake, *Geophys. Res. Lett.*, 27, 1941, 2000.
- Dreger, D. S., L. Gee, P. Lombard, M. H. Murray, and B. Romanowicz, Rapid finite-source analysis and near-fault strong ground motions: Application to the 2003 Mw6.5 San Simeon and 2004 Mw6.0 Parkfield earthquakes *Seism. Soc. Am.*, 76, 40, 2005.
- Pasyanos, M. E., D. S. Dreger, and B. Romanowicz, Towards real-time determination of regional moment tensors, *Bull. Seism. Soc. Am.*, 86, 1255, 1996.

21 Towards a Real-time Earthquake Source Determination and Tsunami Early Warning in Northern California

Aur lie Guilhem and Douglas S. Dreger

21.1 Introduction

The Mendocino Triple Junction is the most seismically active region in Northern California, with a variety of unusual seismic events in addition to regular earthquakes. It also represents the southernmost part of the Cascadia subduction zone (CSZ) where potential damaging thrust earthquakes can occur. The current real-time earthquake monitoring is a cascade-type procedure following a joint effort of the USGS Menlo Park and the Berkeley Seismological Laboratory at UC Berkeley. For offshore earthquakes occurring outside of the seismic network, as is the case in the Mendocino region, such a procedure can generate errors in the event detections and locations resulting in incorrect source determinations. With the goal of more efficiently monitoring the offshore region of Northern California, particularly for slow/low-stress-drop and large, possibly tsunamigenic earthquakes, we develop an automatic scanning of continuous long-period (> 20 sec) broadband seismic records following the method proposed by Kawakatsu (1998) and currently in use in Japan (Tsuruoka *et al.*, 2009). In addition, we are proposing an improved algorithm for great earthquakes occurring along the CSZ, that, if implemented in real-time with a continuous scanning algorithm, will provide information that could be utilized for near-source tsunami early warning.

21.2 The approach

We are implementing a continuous seismic scanning algorithm following the method proposed by Kawakatsu (1998) that makes use of continuous long-period filtered data. By using this approach, it is possible to calculate moment tensors every two seconds for each point of a spatial grid. We generated a grid of nearly 5,000 virtual sources, with each point being separated by 0.2 degrees in latitude (between 40N and 43N) and longitude (between -123E and -128E) and a 3 km interval in depth (5 to 38 km). We selected four Berkeley broadband stations (HUMO, ORV, WDC, and YBH) for which we computed a catalog of Green's functions using a 1D velocity model of Northern California. In order to detect all earthquakes of small and large magnitudes within the region, we are implementing two parallel-running systems. The first one is an inversion of 380 seconds of data filtered between 20 and 50 sec to detect earthquakes with magnitudes between 3.5 and 7. The second system considers longer records (480 sec) filtered at longer periods (100 and 200 sec) to account for M8+ earthquakes.

21.3 Detecting a M8+ earthquake

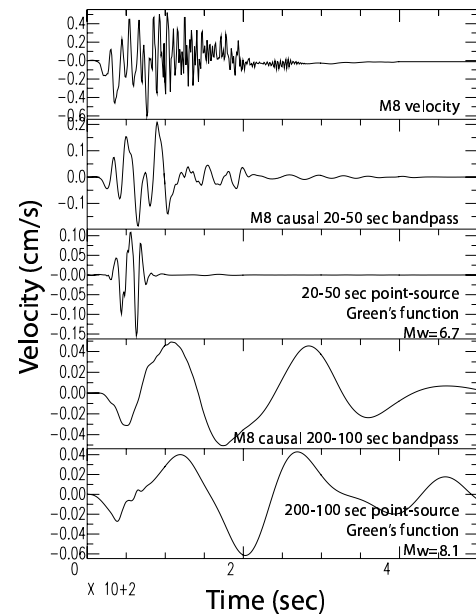


Figure 2.40: Comparison of the frequency bands (0.02-0.05 Hz and 0.005-0.01 Hz) and corresponding Green's functions for a magnitude 8 earthquake along the CSZ.

The CSZ that marks the subduction of the Pacific Plate beneath the North American Plate can produce very large and tsunamigenic earthquakes - magnitude 9.0 or greater - if rupture occurs over the entire area. The last known great earthquake in the region was in January of 1700, and geological evidence indicates that great earthquakes may have a return time of 300 to 600 years. Because there is no available seismic data for a magnitude 8+ earthquake in the study region, we performed a series of synthetic tests for such large events, defined with uniform and variable slip models along the subduction zone. Figure 2.40 illustrates the need to look for longer period data for a M8+ earthquake. Indeed we find that inversions using the 20-50 sec passband fail to recover the seismic moment and location of the tested event. The moment is underestimated, yielding only a M6.7 for a M8.2 synthetic earthquake, and our best solution is located onshore (Figure 2.41a). The narrow band processing and the point-source synthetic only fit a small portion of the record, and the inversion is not sensitive

to the total moment of the event.

However, for the 100-200 sec passband, the inversion yields a point-source location near the fault centroid (Figure 2.41), indicating that this passband works well in identifying the earthquake magnitude, mechanism and location. Furthermore, for the heterogeneous slip models, the detections show better variance reductions (VR) due to the concentration of slip that is better represented by a point-source assumption (Figure 2.41b).

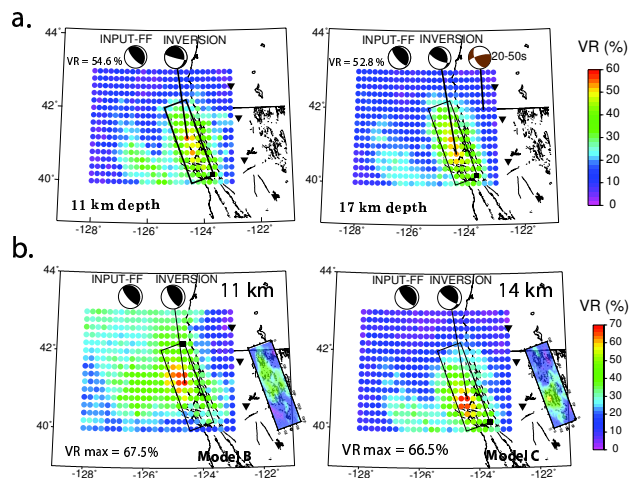


Figure 2.41: Maps of the best VRs obtained for the homogeneous slip model at 11 and 17 km depth (a.) and variable slip models (b.).

21.4 Multi-point source

For great earthquakes, the proximity of the seismic stations to the rupture segment leads to the problem of a near-field component, for which the single point-source assumption considered in the previously described method could fail. To account for the finiteness of the near-field rupture, we are testing the algorithm with multi-point sources obtained after summing together single point sources accounting for the respective distances and azimuths between source and receiver for each of the sources. By doing this, it is possible to study any type of rupture and directivity: north to south, south to north, and bilateral, depending on the grid points considered.

Figure 2.42 demonstrates that the multi-point source assumption (here a summation of three points of the grid) can deliver a better source solution of a large earthquake located off the coast of Northern California than a single point source. Indeed the VR increases from 66% (Figure 2.42b) to 75% (Figure 2.42d).

21.5 Conclusions

Such scanning will provide complete information on the events in real-time using a single stage of processing,

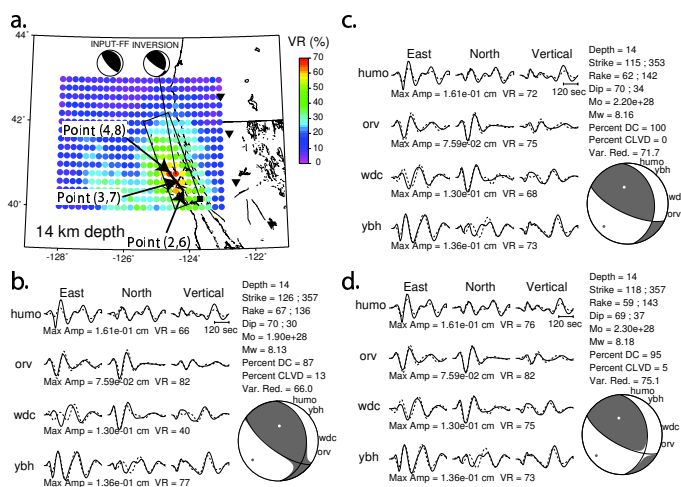


Figure 2.42: Comparison of the moment tensor (MT) using single and multi-point source assumptions. a) Map of the best VRs at 14 km depth for Model C (Figure 2.41). b) Best MT analysis obtained using a single point source. c) MT analysis after summing Points (2,6), (3,7) and (4,8). d) Same as c) but considering a south to north rupture.

and for this reason it will be faster than the current procedures. The method that we are implementing makes use of regional seismic recording stations with continuous real-time telemetry that will enable autonomous detection, location, estimation of scalar seismic moment, and determination of the mode of faulting (i.e. dip-slip versus strike-slip) within approximately 8 minutes of the earthquake occurrence and before the damaging tsunami waves reach the coastline. In the future, our efforts toward a real-time source parameter reporting system for great earthquakes may aid in the development of a tsunami early warning system in Northern California.

21.6 Acknowledgements

This project is supported by the U.S. Geological Survey through award G10AP00069 (NERHP).

21.7 References

- Kawakatsu, H., On the realtime monitoring of the long-period seismic wavefield, *Bull. Earth. Res. Inst.*, 73, 267-274, 1998.
- Tsuruoka, H. H. Kawakatsu, and T. Urabe, GRID MT (Grid-based Realtime Determination of Moment Tensors) monitoring the long-period seismic wavefield, *Phys. Earth Planet. Int., Special issue: Earthquakes in subduction zones: A multidisciplinary approach*, 175, 8-16, 2009.

22 Seismic Constraints on Fault-Zone Frictional Properties at Seismogenic Depth on the San Andreas Fault, Parkfield

Taka'aki Taira, Robert M. Nadeau, and Douglas S. Dreger

22.1 Introduction

Probing subsurface fault-zone frictional properties is a key to improving our understanding of the mechanics of postseismic deformations following larger earthquake that will control the occurrences of subsequent aftershocks and triggered earthquakes. Geodetic measurements have revealed spatially and temporally varying postseismic deformations in the crust immediately after large earthquakes (e.g., *Johanson et al.*, 2006; *Langbein et al.*, 2006). The estimations in deformation field at depth are, however, limited by surface measurements of strain. We propose a methodology for observing subsurface frictional properties of the fault zone by exploiting cumulative seismic slips derived from repeating earthquake sequences.

22.2 Frictional Properties at Depth

Repeating earthquakes are sequences of seismic events that are believed to rupture isolated asperities in creeping sections of fault zones (*Nadeau and McEvilly*, 1999). Their seismic source characteristics have been used to probe spatiotemporal fault-zone properties such as fault healing processes (*Vidale et al.*, 1994), deep creep rate (*Nadeau and McEvilly*, 1999), and fault strength (*Taira et al.*, 2009) as well as to monitor temporal changes in the crustal structure (*Niu et al.*, 2003), by utilizing seismograms from repeating earthquakes. One major advantage of making use of source characteristics of repeating earthquake sequences is that spatial changes in time-dependent fault properties can be more easily isolated than examining spatiotemporal changes in seismicity rates. An ideal test for measuring frictional properties has been provided by the 2004 M 6 Parkfield earthquake, California, because numerous repeating earthquakes have been found in the postseismic period of the 2004 Parkfield earthquake.

We explore subsurface cumulative fault slips extracted from a set of 27 repeating earthquake sequences extending over a depth range of 10 km at the Parkfield segment of the San Andreas fault. These sequences are chosen because around 5 repeating earthquakes in individual sequences typically occurred during the first month of the postseismic period, which allows us to illuminate time evolutions of cumulative seismic slips. Additionally, we have been monitoring selected sequences since 1984. We are able to well constrain background levels of cumulative seismic slips that needed to be corrected in order to address time-dependent postseismic deformations. Park-

field repeating earthquakes have been detected from continuous HRSN borehole seismograms, and their locations were determined using a double-difference relocation approach (*Nadeau et al.*, 2004). The seismic moments also were reliably evaluated through a spectral ratio method introduced by (*Nadeau and Johnson*, 1998). Those precise determinations in source characteristics of individual sequences are crucial to identifying spatiotemporal variations of cumulative seismic slips.

We have employed rate-strengthening friction (*Perfettini and Avouac*, 2005) and viscoelastic models (*Montési*, 2004) to characterize fault-zone rheological properties from seismological observations of postseismic deformation following the 2004 Parkfield earthquake. We first show that 24 of the 27 sequences can be well-explained by the rate-strengthening friction model (Figure 2.43a). We then evaluate frictional parameter $a\sigma$ where a is a frictional coefficient and σ is effective normal stress, by combining the static Coulomb stress change based on the coseismic slip model of the mainshock (*Kim and Dreger*, 2008). Our results suggest $a\sigma$ to be 0.01-0.5 MPa (Figure 2.43b), a value that is generally consistent with previous studies (*Marone et al.*, 1991).

22.3 Conclusions

Our preliminary result suggests that cumulative seismic slips inferred from repeating earthquake sequences provide a means of observing the in-situ frictional parameter. Continuing work will explore spatial variation in frictional parameters and the slip distribution of individual repeating earthquake sequences with finite source modeling.

22.4 Acknowledgements

The present study was supported by the National Science Foundation EAR-0910322. The Parkfield High-Resolution Seismic Network is operated by University of California, Berkeley Seismological Laboratory with financial support from the U.S. Geological Survey through National Earthquake Hazards Reduction Program awards 07HQAG0014 and G10AC00093. We would like to thank A. Kim for providing us with the coseismic slip model.

22.5 References

Johanson, I.A., E.J. Fielding, R. Rolandone and R. Bürgmann, Coseismic and postseismic slip of the 2004 Parkfield earthquake from space-geodetic data, *Bull. Seism. Soc. Am.*, 96, S269-S282, 2006.

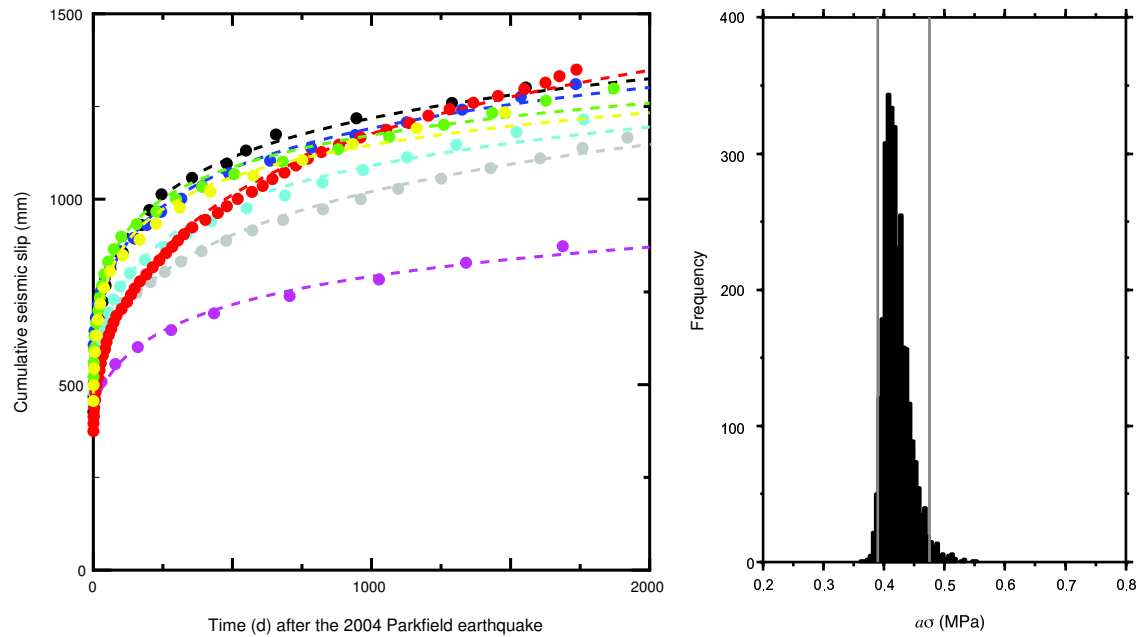


Figure 2.43: (a) Time evolutions of cumulative seismic slips derived from selected eight repeating earthquake sequences (circles) after the 2004 Parkfield earthquake. Also shown are the predicted cumulative fault slips (solid curves) from a rate-strengthening friction model. (b) Distribution of frictional parameter $a\sigma$ for one sequence. Gray vertical lines are the 95% confidence interval using a bootstrap approach with 3,000 subsample data sets.

Kim, A., and D. S. Dreger, Rupture process of the 2004 Parkfield earthquake from near-fault seismic waveform and geodetic records, *J. Geophys. Res.*, *113*, B07308, doi:10.1029/2007JB005115, 2008.

Langbein, J., J.R. Murray, and H.A. Snyder, Coseismic and initial postseismic deformation from the 2004 Parkfield, California, earthquake, observed by global positioning system, electronic distance meter, creepmeters, and borehole strainmeters, *Bull. Seismol. Soc. Am.*, *96*, S304-S320, doi 10.1785/0120050823, 2006.

Marone, C.J., C.H. Scholtz, and R. Bilham, On the mechanics of earthquake afterslip, *J. Geophys. Res.*, *96*(B5), 8441-8452, doi:10.1029/91JB00275, 1991.

Montési, L.G., Controls of shear zone rheology and tectonic loading on postseismic creep, *J. Geophys. Res.*, *109*, doi:10.1029/2003JB002925, 2004.

Nadeau, R.M. and L.R. Johnson, Seismological studies at Parkfield VI: Moment release rates and estimates of source parameters for small repeating earthquakes, *Bull. Seismol. Soc. Am.*, *88*, 790-814, 1998.

Nadeau, R.M. and T.V. McEvilly, Fault slip rates at depth from recurrence intervals of repeating microearthquakes, *Science*, *285*, 718-721, 1999.

Nadeau, R.M., A. Michelini, R.A. Uhrhammer, D. Dolenc and T.V. McEvilly, Detailed kinematics, structure and recurrence of micro-seismicity in the SAFOD target region, *Geophys. Res. Lett.*, *31*, L12S08, doi:10.1029/2003GL019409, 2004.

Niu, F., P.G. Silver, R.M. Nadeau and T.V. McEvilly, Migration of seismic scatterers associated with the 1993 Parkfield aseismic transient event, *Nature*, *426*, 544-548, 2003.

Perfettini, H. and J.-P. Avouac, Postseismic relaxation driven by brittle creep: A possible mechanism to reconcile

geodetic measurements and the decay rate of aftershocks, application to the Chi-Chi earthquake, Taiwan, *J. Geophys. Res.*, *109*, B02304, doi:10.1029/2003JB002488, 2004.

Taira, T., P.G. Silver, F. Niu and R.M. Nadeau, Remote triggering of fault-strength changes on the San Andreas Fault at Parkfield, *Nature*, *461*, 636-639, doi:10.1038/nature08395, 2009.

Vidale J.E., W.L. Ellsworth, A. Cole and C. Marone, Variations in rupture process with recurrence interval in a repeated small earthquake, *Nature*, *368*, 624-626, 1994.

23 Postseismic Variations in Seismic Moment and Recurrence Interval of Repeating Earthquakes at Parkfield

Kate Huihsuan Chen (National Taiwan Normal Univ.), Roland Bürgmann, Robert M. Nadeau, Ting Chen (Caltech), and Nadia Lapusta (Caltech)

23.1 Observations of postseismic recurrence behavior

In laboratory experiments, longer stationary contact time leads to larger seismic moment during repeated ruptures. However, not all observations in natural fault systems agree with the prediction. We analyze a subset of 34 M -0.4~2.1 repeating earthquake sequences (RES) from 1987-2009 at Parkfield to examine the variation of their recurrence properties in space and time.

Following the 29 September 2004, M 6.0 Parkfield earthquake, a strongly accelerated rate of postseismic repeats is observed for 22 of the 34 event sequences. These repeating events have greatly reduced recurrence intervals that increase systematically with time (Figure 2.44a). The rapid event recurrences reflect increased loading of the RES asperities by coseismic stress changes and accelerated fault creep surrounding the 2004 rupture (Johanson *et al.*, 2006; Johnson *et al.*, 2006; Murray and Langbein, 2006). 36% of the 773 recurrence intervals are shorter than 0.1 times the average interval, and 100% of these short intervals follow the 2004 Parkfield event.

In addition to this recurrence acceleration, we also find systematic changes in seismic moment (M_o), where most sequences experienced an immediate increase in M_o and subsequent decay as T_r approached pre-quake durations. Figure 2.44 shows the temporal evolution of recurrence intervals and seismic moment for three example groups. The RES at shallower depth tend to have a larger range in both T_r and M_o (Figure 2.44a-b), whereas deeper RES show smaller variation (Figure 2.44d-e). The shallowest RES with the greatest magnitude (the M1.8-2.1 SAFOD target events) among the events we studied reveal large variation in T_r but small variation in M_o (Figure 2.44g-h).

To further explore the variability in seismic moment M_o and recurrence interval T_r , and to investigate their potential relation, we plot M_o vs. T_r , with M_o normalized by the average M_o (M_{ave}) of the whole sequence in Figure 2.44c, f, and i. To quantify the relation between M_o and T_r , we fit the postseismic data with $M_o/M_{ave} \sim q \log(T_r)$ using the least squares method, for the 26 Parkfield RES with more than four postseismic events (following Peng *et al.*, 2005). The fits are shown by dashed lines in Figure 2.44c, f, and i. Positive/negative slopes q of the M_o - T_r relation correspond to an increase/decrease in moment with increasing recurrence time. We find that 19 out of 26 RES have decreasing M_o as T_r increases.

23.2 Rate and state models of repeating sequences

These observations are qualitatively consistent with earthquake simulations in 3D continuum fault models with rate- and state-dependent friction shown in Figure 2.45. In the models, RES are produced on velocity-weakening patches surrounded by velocity-strengthening fault areas (Figure 2.45a). In the simulations, the sign of the slope for the M_o - T_r relation is controlled by the ratio r/h^* , where r is the radius of the velocity-weakening patch and h^* is the so-called nucleation size dependent on the friction properties of the patch (Chen and Lapusta, 2009):

$$h^* = (\pi^2/4) \cdot \mu b L / (\pi \sigma (b - a)^2)$$

where μ is the shear modulus, σ is the effective normal stress, and a , b and L are friction parameters. Given the same nucleation size h^* (i.e., the same frictional properties and effective normal stress), smaller radii, and hence smaller seismic moments, result in negative M_o - T_r slopes, whereas larger radii, and hence larger moments, lead to weak positive M_o - T_r slopes, consistent with observations. Conversely, with only a small percentage of its slip accumulated seismically, a small asperity appears to grow in M_o under high loading rate, which is contrary to the view that M_o should decrease due to a reduced strength recovery time. Our simulations show that the recurrence intervals T_r are systematically reduced for larger loading velocity, as intuitively expected and confirmed by our observations.

23.3 Conclusion

Most shallower RES (<7 km) experienced a strong reduction in T_r accompanied by an increase in M_o immediately following the 2004 Parkfield mainshock, evolving towards pre-earthquake values in subsequent years. Among the shallow RES, larger events show less variability in seismic moment than small events, even though their transient recurrence acceleration is strong. This magnitude-dependent postseismic behavior can be qualitatively explained by 3-D models using rate and state friction laws. Small asperities tend to accumulate most of their slip aseismically, with earthquakes occupying a small fraction of their area. When experiencing higher loading rates, these small events are found to rupture a larger area of the velocity-weakening asperity, producing the observed behavior of increasing moment with increasing loading rate and decreasing recurrence intervals. For

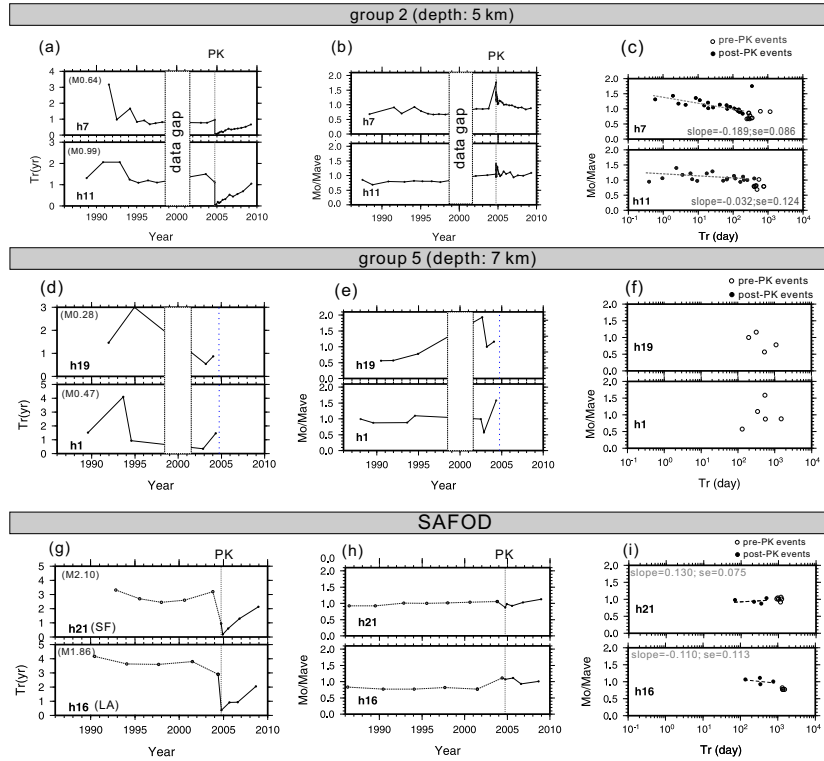


Figure 2.44: (a) Recurrence interval, (b) relative moment variation (ratio of M_o and average M_o of the sequence) as a function of time, and (c) relative moment as a function of recurrence interval for group 2 repeating sequences. Black and open circles indicate post- and pre- Parkfield events, respectively. (d-f) For group 5 repeating sequences. (g-i) For SAFOD repeating sequences.

the postseismic period, the good correlation between the observation and model predictions implies that the sudden increase in and time-variability of the loading rate on the velocity-weakening patch plays a significant role in a repeater's seismic properties. Such an inference, however,

should be tested with proper laboratory-based friction experiments in the future.

23.4 References

Chen, T., and N. Lapusta, Scaling of small repeating earthquakes explained by interaction of seismic and aseismic slip in a rate and state fault model, *J. Geophys. Res.*, *114*, B01311, doi:10.1029/2008JB005749, 2009.

Johnson, K. M., R. Bürgmann, and K. Larson, Frictional properties on the San Andreas Fault near Parkfield, California, inferred from models of afterslip following the 2004 earthquake, *Bull. Seism. Soc. Am.*, *96*(4B), S321-S338, doi: 10.1785/0120050808, 2006a.

Johanson, I. A., E. J. Fielding, F. Rolandone, and R. Bürgmann, Coseismic and postseismic slip of the 2004 Parkfield earthquake from space-geodetic data, *Bull. Seismol. Soc. Am.*, *96*(4B), S269-S282, doi: 10.1785/0120050818, 2006b.

Murray, J., and J. Langbein, Slip on the San Andreas fault at Parkfield, California over two earthquake cycles and the implications for seismic hazard, *Bull. Seismol. Soc. Am.*, *96*(4B), S283-S303, doi: 10.1785/0120050820, 2006.

Peng Z., J. E. Vidale, C. Marone, and A. Rubin, Systematic variations in recurrence interval and moment of repeating aftershocks, *J. Geophys. Res.*, *32* doi:10.1029/2005GL022626, 2005.

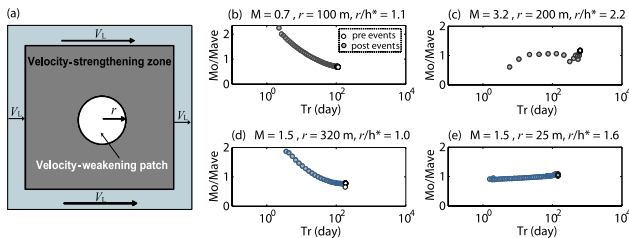


Figure 2.45: Simulation results for RES response to post-seismic effects of a large nearby event using different model parameters. (a) Fault model for 3-D simulation. A vertical strike-slip fault is embedded into an elastic medium and governed by rate and state friction laws (Chen and Lapusta, 2009). (b-e) Computed relative seismic moment as a function of recurrence interval for varying patch radius r and nucleation size h^* . Open and filled circles indicate the preseismic and postseismic events, respectively.

24 Identification of Nonvolcanic Tremors Triggered by Regional Earthquakes in the Parkfield, California Region

Aur lie Guilhem, Zhigang Peng (Georgia Institute of Technology), and Robert M. Nadeau

24.1 Introduction

Nonvolcanic tremor activity along the Parkfield-Cholame section of the San Andreas fault (SAF) in central California has been recorded since 2001 (Nadeau and Dolenc, 2005; Nadeau and Guilhem, 2009). In addition to ambient tremors, triggered tremors associated with the surface waves of large teleseisms have been recognized (Gomberg *et al.*, 2008; Peng *et al.*, 2009). However, no tremors triggered by regional earthquakes have been observed within the region and in other tremor regions. Rubinstein *et al.* (2009) explained the absence of tremor triggering from regional quakes in Cascadia by the similar frequency bands (i.e. 1-15 Hz) and waveform characteristics of the P and S coda waves from regional events. However Brodsky and Prejean (2005) showed that large earthquakes at regional and teleseismic distances have triggered microearthquakes and that the large-amplitude long-period surface waves appeared to favor the triggering more than shorter period waves of similar amplitude. To effectively separate the potential triggered tremors from the regional coda waves, we propose to examine higher frequency bands (i.e. above 15 Hz).

24.2 Detection of triggered tremors

By systematically searching the high-frequency (i.e. > 15 Hz) filtered seismograms (250 samples per second) of 99 M5+ earthquakes occurring between July 2001 and April 2010 and distributed between 100 and 1200 km from the broadband seismic station PKD located at Parkfield, we visually identified four earthquakes that triggered tremors in central California: the 15 June 2005 M7.2 Mendocino, 04 January 2006 M6.6 Baja California (BC), 03 August 2009 M6.9 BC, and 04 April 2010 M7.2 BC earthquakes. The triggered tremors constitute consecutive bursts of energy that are phase-correlated with the passing of the surface waves (Figure 2.46).

We found that between 3 and 15 Hz, which corresponds to the typical frequency band for nonvolcanic tremors, the data mainly show the emergent P and S waves without clear indication of triggered tremors. However, tremors are best observed between 15 and 30 Hz for the 2006 and 2010 earthquakes and between 25 and 40 Hz for the 2005 and 2009 events (Figure 2.46a).

We adapted the envelope-based location algorithm already used for ambient tremors to locate the four triggered tremors. Their sources, with the exception of the 2009 event, are found on or close to the main SAF segment, within the region where ambient and teleseismi-

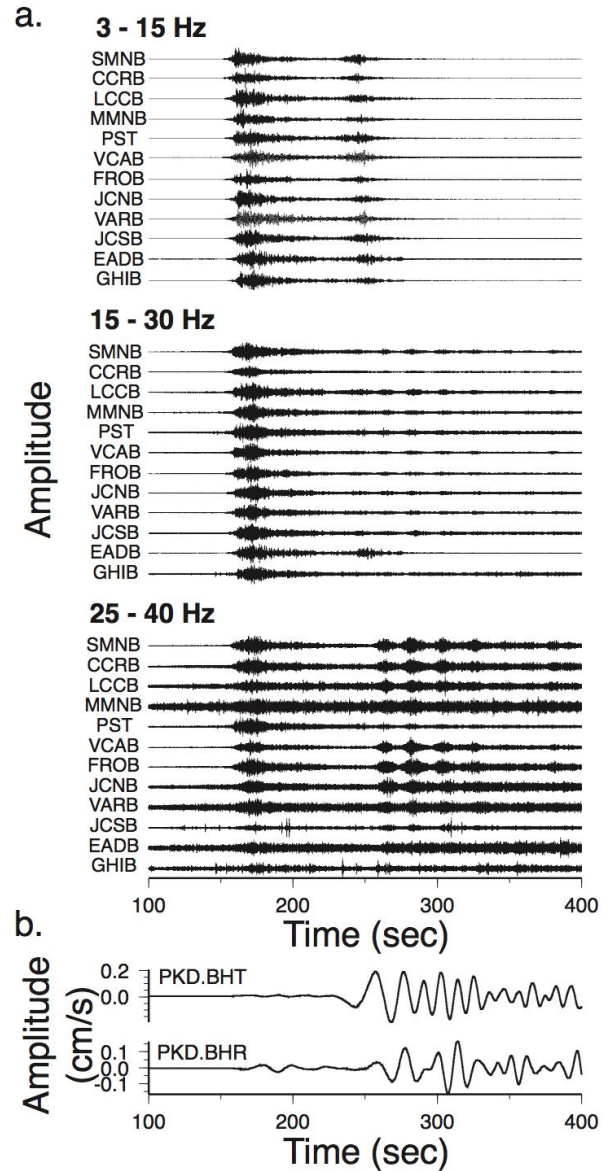


Figure 2.46: a) Velocity seismograms (relative scaling) ordered from north (top) to south (bottom) along the SAF strike recorded by the HRSN stations and the surface station PST filtered at several frequency bands for the 2005 Mendocino earthquake. The triggered tremor is seen between 250 and 350 sec. b) Unfiltered transverse (BHT) and radial (BHR) components of the station PKD from Guilhem *et al.* (2010).

cally triggered tremors have been detected. However, the 2009 BC earthquake appears to occur about 25 km NE of the fault.

24.3 Peak ground velocities

Most of tremor signals occur in phase with the surface waves, seeming to indicate a causal relationship between occurrence of tremors and surface waves. We measured the peak ground velocities (PGV) of the surface waves of the 99 earthquakes as well as of the teleseisms studied by Peng *et al.* (2009) recorded on the transverse and vertical components of the PKD station (Figure 2.47a), and we found that the events that did trigger tremors in central California have among the largest PGVs. This is emphasized after filtering the data between 30 and 200 sec (Figure 2.47b).

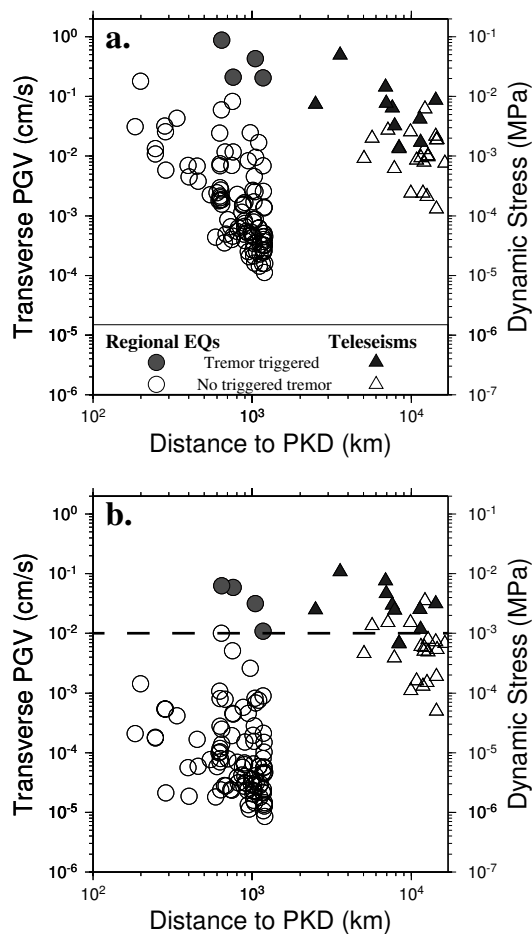


Figure 2.47: a) Peak ground velocities (PGV) recorded at PKD on unfiltered transverse components of PKD. b) PGVs recorded between 30 and 200 sec period from Guilhem *et al.* (2010).

If we consider a PGV threshold of 0.01 cm/s to separate triggering and non-triggering earthquakes at both

regional and teleseismic distances and use a nominal surface wave velocity of 3.5 km/s and the elastic modulus of 35 GPa at tremor depth we found a corresponding dynamic stress of about 1 kPa (Figure 2.47b).

24.4 Conclusions

We show that tremors are not bandpass limited to 1-15 Hz but can have significant energy at higher frequencies. By searching seismic records above 15 Hz we found four triggered tremors correlating with the passage of the surface waves. High-frequency content is also observed for teleseismically triggered tremors. Finally, our calculated dynamic stress change of 1 kPa is in agreement with other findings, indicating that it is important to continue detecting and analyzing the tremor activity in central California in order to better define the fault mechanics and interactions in the deep crust.

24.5 Acknowledgements

This project is supported by the U.S. Geological Survey through award 07HQAG0014 and 08HQGR0100 and by the National Science Foundation through award EAR-0537641. Z. Peng was supported by the National Science Foundation through awards EAR-0809834 and EAR-0956051.

24.6 References

Brodsky, E. E., and S. G. Prejean, New constraints on mechanisms of remotely triggered seismicity at Long Valley Caldera, *J. Geophys. Res.*, *110*, B04302, 2005.

Gomberg, J., J. L. Rubinstein, Z. Peng, K.C. Creager, J. E. Vidale, and P. Bodin, Widespread triggering of nonvolcanic tremor in California, *Science*, *319*, 173, 2008.

Guilhem, A., Z. Peng, and R. M. Nadeau, High-frequency identification of non-volcanic tremor triggered by regional earthquakes, *Geophys. Res. Lett.*, *37*, in press, 2010.

Nadeau, R. M., and D. Dolenc, Nonvolcanic tremors deep beneath the San Andreas Fault, *Science*, *307*, 389, 2005.

Nadeau, R. M., and A. Guilhem, Nonvolcanic tremor and the 2003 San Simeon and 2004 Parkfield, California earthquakes, *Science*, *325*, 191-193, 2009.

Peng, Z., J. E. Vidale, K. C. Creager, A. G. Wech, R. M. Nadeau, and K.C. Creager, Remote triggering of tremor along the San Andreas Fault in central California, *J. Geophys. Res.*, *114*, B00A06, 2009.

Rubinstein, J. L., J. Gomberg, J. E. Vidale, A. G. Wech, H. Kao, K. C. Creager, and G. Rogers, Seismic wave triggering of nonvolcanic tremor, episodic tremor and slip, and earthquakes on Vancouver Island, *J. Geophys. Res.*, *114*, B00A01, 2009.

25 Locating Nonvolcanic Tremors Beneath the San Andreas Fault Using a Station-pair Double-Difference Location Method

Robert M. Nadeau, Haijiang Zhang (Massachusetts Institute of Technology), and Nafi Toksoz (Massachusetts Institute of Technology)

25.1 Introduction

It has been a challenging task to locate nonvolcanic tremors because of their lack of impulsive wave arrivals. To help overcome these difficulties, we have developed a station-pair double-difference (DD) location method to determine absolute tremor locations by directly using the station-pair travel time differences measured from cross-correlating tremor waveform envelopes. To account for velocity model inaccuracy, multiple tremors are located together to invert for station corrections. The new method is applied to tremors in the Parkfield region of central California occurring between 27 July 2001 and 21 February 2009, and the resulting locations are compared to the catalog locations of *Nadeau and Guilhem* (2009). The comparison shows that the new tremor locations more clearly delineate the spatial and temporal distribution of tremor activity in the area and improve our understanding of tremor origin and process.

25.2 Station-pair double-difference location method

The DD location method, developed by *Waldhauser and Ellsworth* (2000), has been widely used to locate earthquakes using differential arrival times at common stations from pairs of ‘events’. We use the same concept applied to the case where differential times on pairs of ‘stations’ from common events are accurately calculated (using the station-pair differential travel times directly to locate the tremor events). In addition, because station corrections are included in our inversion, our approach is a ‘multiple-event’ location method. Our method uses station-pair cross-correlation delay times measured from tremor waveform envelopes between different stations. It should also be applicable for locating low frequency earthquakes (LFEs) when similar travel time difference information is available. We applied our location method to station-pair delay time measurements from nonvolcanic tremors occurring beneath the San Andreas Fault around the Parkfield and Cholame area (originally detected and located by *Nadeau and Guilhem* (2009)). More detail on the station-pair DD method can be found in *Zhang et al.* (2010).

25.3 Results and Discussion

Figure 2.48 compares station-pair DD locations with original catalog locations (*Nadeau and Guilhem*, 2010). The DD located tremors are shifted northeast and deeper (Figure 2.48C and D), relative to the original catalog.

The average shift is 3.4 km in X and 3.7 km in depth. The northeast shift may be due to bias introduced by our use of a 1-D velocity model in this region of strong lateral velocity contrast. The shift in depth is likely due to the station-pair DD location method’s more accurate determination of tremor depths, which avoids the coupling effect between depth and origin time. The DD locations are also more clustered, and more substructure can be seen than with the catalog locations (Figure 2.48G and H). Overall, the location uncertainties of the station-pair DD tremor locations are about half those of the catalog tremors (Figure 2.48G and H; also see Auxiliary Material in (*Zhang et al.*, 2010)).

Figure 2.48E and F show histograms of tremor depths from the catalog and station-pair DD locations. In this area, earthquakes locate in the upper ~ 15 km of the Earth’s crust, and the Moho depth is ~ 25 km. Hence, our results suggest that tremors predominate below the seismogenic zone, in the ductile lower crust, and that a distinct gap in depth between the seismogenic and tremor zones exists.

Nadeau and Guilhem (2009) also observed periodic episodes of tremors at Cholame after the 2004 Parkfield M6 earthquake that were concentrated and more periodic in the southwestern portion of the tremor zone. Our results confirm these observations (see Figures 2c and d of *Zhang et al.*, 2010), and they indicate that the process generating tremors in this area may be structurally controlled and vary across the SAF.

25.4 Acknowledgements

Supported through USGS grants 06HQGR0167, 07HQAG0014, 08HQGR0100, and 08HQGR0101; DOE contract DE-FC52-06NA27325; NSF grants EAR-0537641 and EAR-0544730; and Chinese government executive program SinoProbe-02.

25.5 References

- Nadeau, R.M. and A. Guilhem, Nonvolcanic Tremor Evolution and the San Simeon and Parkfield, California, Earthquakes, *Science*, 325, 191-193, 2009.
- Waldhauser, F. and W.L. Ellsworth, A double-difference earthquake location algorithm: method and application to the Northern Hayward Fault, California, *Bull. Seism. Soc. Am.* 90, 1353-1368, 2000.
- Zhang, H., R.M. Nadeau and N. Toksoz, Locating nonvolcanic tremors beneath the San Andreas Fault using a station-pair double-difference location method, *Geophys. Res. Lett.*, 37, L13304, doi:10.1029/2010GL043577, 2010.

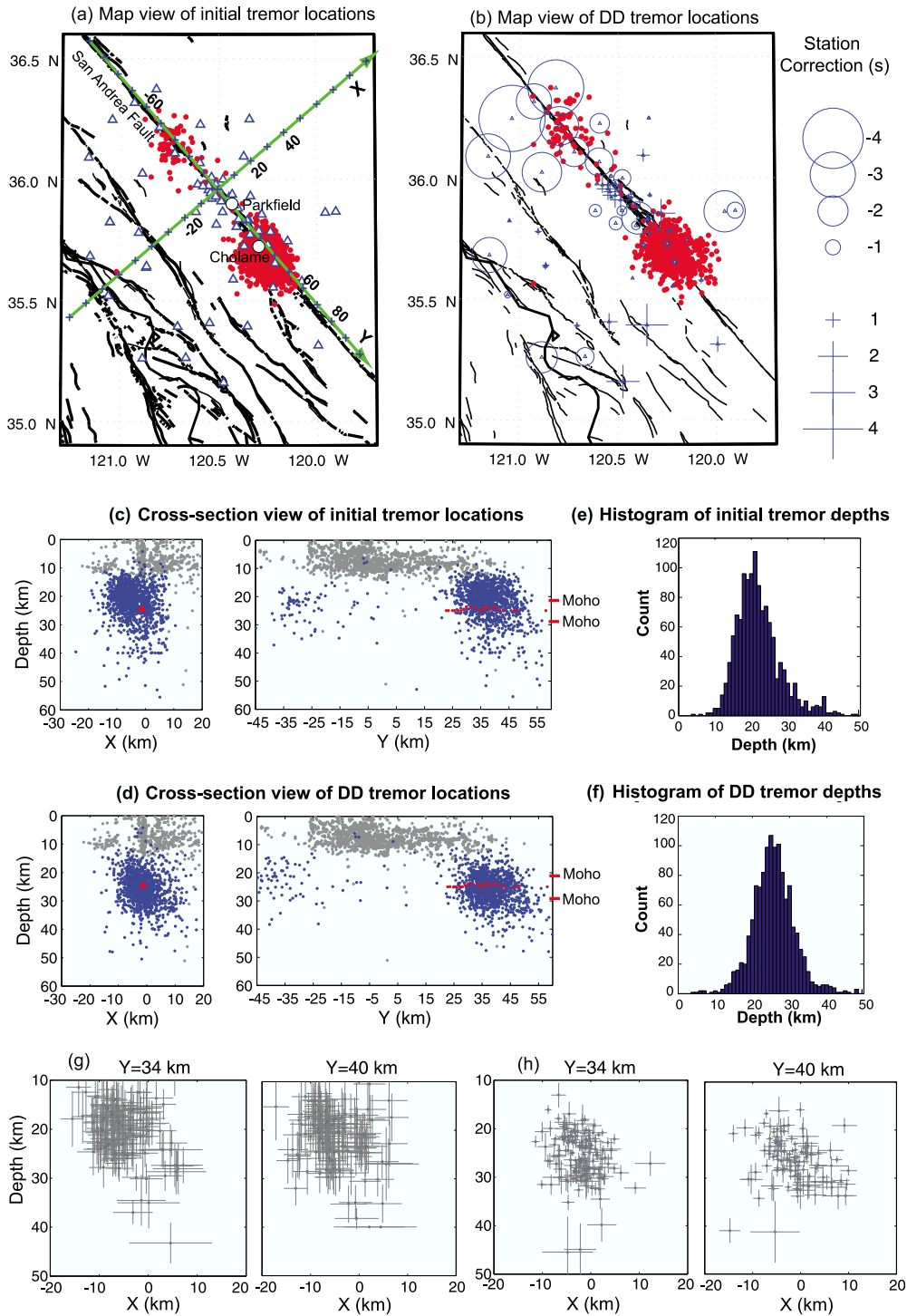


Figure 2.48: Comparison of catalog and station-pair DD tremor locations. (A) Map view of 1246 tremors (red/gray dots) and 64 stations (triangles) used in this study. Tremor catalog locations are from *Nadeau and Guilhem* (2009). The Cartesian coordinate system used in location is shown with a tick (marked as ‘+’) interval of 10 km on X and Y axes. Faults are shown as black lines. Parkfield and Cholame are marked as white dots. (B) Map view of new tremor locations determined by station-pair DD location method. Station corrections in seconds are also shown. (C) Catalog tremor locations (blue/dark-gray) are shown in X-depth and Y-depth sections. (D) DD tremor locations are shown in X-depth and Y-depth sections. (E) Depth distribution of catalog tremor locations. (F) Depth distribution of DD tremor locations. (G) Across-fault cross sections of catalog tremor locations and the associated 95% uncertainty bounds at Y=34 and 40 km (within 1 km of both sides of the section). (H) The same as G but for DD tremor locations. In both panels (C) and (D), background seismicity from *Thurber et al.* (2006) is shown as light gray dots and the inferred LFE locations of *Shelly* (2009) are shown as the near horizontal red/light-gray dots at ~25 km depth.

